



Faculty of Engineering and Technology

Department of Chemical, Material and Metallurgical Engineering

**UV Photodegradation of Textile dyes using $\text{TiO}_2\text{-ZnO}$
supported on Banana Peel Activated Carbon**

by

Name: **Bonface Ochieng' Orero**

Student ID number: **18100051**

The thesis presented in fulfilment for the degree of Master of Engineering in Chemical Engineering in the Faculty of Engineering and Technology at the Botswana International University of Science and Technology.

Supervisor(s):

Prof. Freeman Ntuli

Department of Chemical, Material
and Metallurgical Engineering
Faculty of Engineering and
Technology, BIUST
E-mail Address: ntulif@biust.ac.bw

Prof. Ochieng' Aoyi

Department of Chemical, Material
and Metallurgical Engineering
Faculty of Engineering and
Technology, BIUST
E-mail Address: aoyio@biust.ac.bw

March/2022

DECLARATION REGARDING THE WORK AND COPYRIGHT

Candidate (please write in caps or type): BONFACE ORERO

Student ID number: 18100051

Thesis Titled: UV PHOTODEGRADATION OF TEXTILE DYES USING TIO₂-
ZNO SUPPORTED ON BANANA PEEL ACTIVATED CARBON

I, the **Candidate**, certify that the Thesis is all my own original work and that I have not obtained a degree in this University or elsewhere on the basis of any of this work.
(If the thesis is based on a group project, then the student must indicate the extent of her / his contribution, with reference to any other theses submitted or published by each collaborator in the project, and a declaration to this effect must be included in the thesis)

This dissertation/thesis is copyright material protected under the Berne Convention, the Copyright and Neighbouring Rights Act, Act. No. 8 of 2000 and other international and national enactments, in that behalf, on intellectual property. It must not be reproduced by any means, in full or in part, except for short extracts in fair dealing; for researcher private study, critical scholarly review or discourse with an acknowledgement, without the written permission of the office of the Postgraduate School, on behalf of both the author and the BIUST.

Signed: 

Date: 09/03/2022

Primary Supervisor (please write in caps or type)

I, the Candidate's **Primary Supervisor**, hereby confirm that I have inspected the above titled thesis and, to the best of my knowledge, it is based on the original work of the candidate.

Signed: 

Date: 10/03/2022

CERTIFICATION

This dissertation titled “**UV Photodegradation of Textile dyes using TiO₂-ZnO supported on Banana Peel Activated Carbon**” was prepared by **Bonface Ochieng’ Orero** and submitted as a fulfilment of the requirement for a degree of Master of Engineering in Chemical Engineering at Botswana International University of Science and Technology.

Approved by:

Primary Supervisor:

Co-Supervisor:

Prof. Freeman Ntuli

Prof. Ochieng’ Aoyi

Signed: *Dr Ntuli* Date: 10/03/2022

Signed: *[Signature]* Date: 09/03/2022



ACKNOWLEDGEMENTS

Foremost, I would like to express my sincere gratitude to my renowned supervisors, Prof. Freeman Ntuli and Prof. Ochieng' Aoyi, for their guidance, continuous support, enthusiasm, and encouragement throughout my study. Their immense knowledge, dynamism and constructive criticism have steered me in all the time of research to the conclusion of this thesis. A debt of gratitude is owed to Botswana International University of Science and Technology and the Department of Chemical, Material and Metallurgical Engineering for acceptance, funding, and noble chance to pursue my study. I am extremely grateful for what BIUST offered me.

My sincere gratitude also goes to the members of the Department of Chemical, Material and Metallurgical Engineering particularly Prof. Edison Muzenda, Prof. Paul Agachi, Prof. Danha Gwiranai, Mr Nhlanhla Othusitse Mr Gaogane Tshepho, Mr Tumeletso Lekgoba, and BIUST covid-19 response team. Also, I thank the Department of Chemistry and Forensic Sciences for allowing me to use their labs and equipment. I thank my fellow postgraduate colleagues, especially Gobusaone Mokokwe, Maipelo Gaopatwe, Mavis Gabookolwe, Plaxcedes Sigauke, Robert Gembo, Saubi Onalethata, Tendai Nyangadzayi, Tlotlo Gabasiane, Tshepo Rapelang, Webla Kouadio, and entire research group members whom we shared the same supervisor. I deeply thank Dr Benton Otieno from the Vaal University of Technology and Dr Joyce Elisadiki from the University of Dodoma for their profound contributions to my research project. I also thank Prof. Cecil King' ondu, Mr Chadwick Alego, Mr Colman Nyambu, Mr Daniel Goroba, Mrs Jemima Kalama, and Mr Joseph Mwilu for the academic advice and moral support.

Last but not least, I thank my wonderful parents Mr Samuel and Mrs Rose Orero for supporting me financially, emotionally, and spiritually throughout my life. Also, express my thanks to my siblings for their support and valuable prayers. My special gratitude goes to my aunt Anne Achieng' and the entire family for their acceptance and great support. I am extending my heartfelt thanks to my family members and friends especially Amos Kitheka, Anthony Omondi, Beryl Boinett, Charles Owino, David Cary, Edwin Alianda, Femi Sewe, Janet Adongo, Job Cedric, Juliana Apiyo, Nguzo Nondo, Omondi Aoyi, Phoebe Awuor, Robert Wanjira, Timothy Kimani, and Tom Otieno for the great support and encouragement. Thank you all for believing in me and for your unwavering support; without you, none of this would be possible.

DEDICATION

I dedicate this research work to my wonderful parents, siblings and Forever loved cousin Oduor Abang’.



TABLE OF CONTENT

Topic	Page Number
DECLARATION REGARDING THE WORK AND COPYRIGHT	i
CERTIFICATION	ii
ACKNOWLEDGEMENTS	iii
DEDICATION	iv
TABLE OF CONTENT	v
LIST OF TABLES	viii
LIST OF FIGURES	ix
NOMENCLATURE	xi
ABSTRACT	xiv
1 INTRODUCTION	1
1.1 Background	1
1.1.1 <i>Dye water pollution</i>	2
1.1.2 <i>Photodegradation</i>	3
1.1.3 <i>Semiconductor as photocatalyst</i>	4
1.1.4 <i>Activated carbon as support material</i>	5
1.2 Motivation/Purpose	5
1.3 Problem statement	6
1.4 Aim and specific objectives	8
1.5 Research questions	9
1.6 Thesis overview	9
2 LITERATURE REVIEW	12
2.1 Emerging contaminants pollution	12
2.1.1 <i>Agricultural pollution</i>	12
2.1.2 <i>Personal care products pollution</i>	13
2.1.3 <i>Endocrine-disrupting hormones pollution</i>	14
2.1.4 <i>Pharmaceutical pollution</i>	14
2.1.5 <i>Textile dyes pollution</i>	15
2.2 Waste treatment methods	16
2.2.1 <i>Conventional treatment method</i>	16
2.2.2 <i>Advanced Oxidation Processes</i>	20
2.3 Heterogeneous photocatalysis	22
2.3.1 <i>Semiconductors as photocatalysts and their bandgap</i>	24
2.3.2 <i>Fundamental of TiO₂ photocatalysis</i>	25
2.3.2.1 <i>TiO₂ stability and recombination approach</i>	26
2.3.2.2 <i>TiO₂ adsorption and recovery approach</i>	26
2.3.3 <i>Photocatalysis operation parameters</i>	28
2.4 Photocatalytic reactors and their configuration	30
2.4.1 <i>Fixed bed reactor</i>	32
2.4.2 <i>Fluidized bed reactor</i>	32

2.4.2.1	Hydrodynamic parameters	33
2.5	Knowledge gaps	35
3	MATERIALS AND METHODS	37
3.1	Materials.....	38
3.2	Analytical equipment	38
3.3	Experimental reactors.....	39
3.3.1	<i>Lab-scale stirred tank reactor</i>	39
3.3.2	<i>Fabricated Fluidized bed reactor</i>	40
3.4	Experimental Design	40
3.5	Experimental setup.....	42
3.6	Experimental procedure	43
3.6.1	<i>Catalyst and support material preparation.....</i>	43
3.6.1.1	Preparation of TiO ₂ through reflux method.....	44
3.6.1.2	ZnO synthesis via precipitation method.....	44
3.6.1.3	Preparation of activated carbon from banana peels.....	44
3.6.1.4	Preparation TiO ₂ -ZnO hybrid	45
3.6.1.5	Immobilization of superior TiO ₂ -ZnO onto activated carbon	45
3.6.2	<i>Preparation and characterization of simulated wastewater</i>	46
3.6.3	<i>Catalyst and support material characterization</i>	47
3.6.4	<i>Photodegradation in lab-scale stirred tank reactor.....</i>	48
3.6.4.1	Effect of KOH activation ratio on the AC adsorption activity	48
3.6.4.2	Photocatalytic efficiency of TiO ₂ -ZnO with different mass ratios.....	49
3.6.4.3	Effect of optimized BAC1 composition superior TiO ₂ -ZnO hybrid activity	49
3.6.4.4	Photodegradation activity of pure, hybrid and composite catalyst.....	50
3.6.4.5	Main active species responsible for R6G photodegradation	50
3.6.4.6	Photodegradation of the dyes using 85%TiO ₂ -ZnO/BAC1.....	51
3.6.4.7	TiO ₂ -ZnO/BAC1 stability and reusability study	51
3.6.4.8	Photodegradation operation parameters	51
3.6.5	<i>Hydrodynamics and photodegradation in fluidized bed reactor.....</i>	52
3.6.5.1	Hydrodynamic studies	52
3.6.5.2	Photodegradation in fluidized bed reactor	54
3.7	Data and error analyses	54
4	RESULTS AND DISCUSSION.....	55
4.1	Catalyst and support material characterization.....	55
4.1.1	<i>X-ray Diffraction analysis.....</i>	55
4.1.2	<i>Fourier Transform Infrared Spectroscopy Analysis</i>	56
4.1.3	<i>Scanning Electron Microscope</i>	58
4.1.4	<i>Brunauer-Emmett-Teller</i>	60
4.1.5	<i>Optical properties</i>	62
4.1.6	<i>Thermal decomposition behaviour.....</i>	64
4.1.7	<i>Particle size distribution of 85%TiO₂-ZnO/BAC1</i>	66
4.2	Photodegradation in lab-scale stirred tank reactor experiments.....	67
4.2.1	<i>Effect of the KOH activation ratio on the AC adsorption activity</i>	67
4.2.2	<i>TiO₂-ZnO photocatalytic activity based on their mass ratio.....</i>	68
4.2.3	<i>Photocatalytic efficiency of TiO₂- ZnO based on BAC1 composition.....</i>	69
4.2.4	<i>Effect of BAC1 composition on photocatalytic reaction kinetics</i>	71
4.2.5	<i>Comparison of photodegradation activity of catalysts.....</i>	73
4.2.6	<i>Main active species on photodegradation and its reaction mechanism.....</i>	74

4.2.7	<i>Photodegradation of the different dyes</i>	76
4.2.8	<i>Estimated COD removal of the dyes</i>	77
4.2.9	<i>Photodegradation operational parameters and kinetics</i>	79
4.2.9.1	Effect of initial solution pH	79
4.2.9.2	Catalyst loading	81
4.2.9.3	Initial concentration	82
4.2.9.4	Temperature	83
4.2.9.5	Stability and reusability	85
4.2.9.6	Energy requirement for decolourization and COD reduction.	86
4.3	Comparison of various dyes degradation studies	87
4.4	Fluidized bed reactor experiments	88
4.4.1	<i>Hydrodynamics study</i>	88
4.4.1.1	Gas holdup	89
4.4.1.2	Estimation of solid concentration axial distribution.....	92
4.4.1.3	Optimum hydrodynamic conditions.....	96
4.4.2	<i>Effect of hydrodynamic parameters on photodegradation</i>	97
4.4.2.1	Reactor inclination angle	97
4.4.2.2	Superficial gas velocity	99
5	CONCLUSION AND RECOMMENDATIONS	101
5.1	Conclusion	101
5.2	Recommendation	104
5.2.1	<i>Engineering significance and recommendation</i>	104
5.2.2	<i>Recommendation for future work</i>	105
	REFERENCE	106

LIST OF TABLES

Table 2-1. Advantages and disadvantages of conventional methods for the treatment of dye wastewater (Foo and Hameed, 2010).	18
Table 2-2. Photocatalyst with their respective bandgap.	24
Table 3-1. OFAT design of experiment of varied parameters.	40
Table 3-2. OFAT design of experiment on hydrodynamic parameters.	41
Table 3-3. Hybrid percentage composition of TiO ₂ and ZnO.	45
Table 3-4. BAC percentage composition on 85% TiO ₂ -ZnO superior hybrid.	46
Table 3-5. Estimated water quality characteristics of simulated wastewater.	46
Table 4-1. FTIR spectra with possible assignments (Benton et al., 2016; El Mragui et al., 2019; Mofokeng et al., 2017).	57
Table 4-2 BET surface areas and pore volumes of the samples.	62
Table 4-3. The estimated Conduction and Valence potential edge of the material.	63
Table 4-4. Shows summarized kinetic data for photodegradation by varying BAC1 loading. Experimental condition: C ₀ - 30ppm, 0.7 g/L catalyst dosage and pH 7.	72
Table 4-5. Estimated COD of the dyes before and after photodegradation.	78
Table 4-6. Comparison of 85%TiO ₂ -ZnO/BAC1 photocatalytic efficiency on the dyes with other similar work.	87
Table 4-7. Global gas hold-up and mass transfer correlations.	90
Table 4-8. Comparison of gas holdup correlation with other studies.	91

LIST OF FIGURES

Figure 1-1. Work outline subjected to this study.	10
Figure 2-1. Schematic diagram of photodegradation mechanism.....	23
Figure 3-1. (a) and (b) Schematic diagram of a lab-scale stirred tank experimental setup.....	42
Figure 3-2. Schematic diagram of fluidized bed reactor.....	43
Figure 4-1. (a) XRD pattern of pure TiO ₂ , ZnO, and their hybrids based on percentage composition, and (b) XRD profile of pure TiO ₂ , ZnO, and prepared activated carbon, superior hybrid, and the composite.	56
Figure 4-2. FTIR spectra of (a) BAC1, (b) TiO ₂ , (c) ZnO, (d) TiO ₂ -ZnO hybrid, (e) TiO ₂ -ZnO/BAC1 composite.....	57
Figure 4-3. SEM images (magnification: 50 μ m) (a) carbonized peel (char) activated carbon at char: KOH ratio 1:1 (b), 1:2 (c), and 1:3 (d).	59
Figure 4-4. SEM images for TiO ₂ (a), ZnO (b), 85% TiO ₂ -ZnO hybrid (c), and 85% TiO ₂ -ZnO/BAC1(d).	59
Figure 4-5 (a) and (c) N ₂ sorption isotherms. (b) and (d) Pore size distribution curves	61
Figure 4-6. UV-vis spectrum in water (a) and PL (b) spectra of the materials.....	63
Figure 4-7. TGA analysis of the synthesized materials.....	65
Figure 4-8. Particle size volume distribution (a), number distribution (b), and cumulative undersize for both number and volume fraction (c)-(d).	66
Figure 4-9. Effect of KOH: char ratio on adsorption performance.	67
Figure 4-10. (a) Effect of hybridization by the different mass ratios of TiO ₂ -ZnO on adsorption and photodegradation rate. (b). Synergistic effect of the hybrids based on the varied mass fraction.	68
Figure 4-11. Effect of BAC1 support composition on TiO ₂ -ZnO hybrid activity. Experimental condition: 30 ppm, 0.7 g/L catalyst dosage, and pH 7.....	70
Figure 4-12. Compares adsorption and photodegradation performance of R6G dye over pure, superior hybrid and composite. Experiment conditions: 1.3 g/L catalyst dosage, 50 ppm, and pH 7.....	73
Figure 4-13. Percentage colour removal of R6G dye over 85% TiO ₂ -ZnO/BAC1 composite in the presence of various radical scavengers.	74
Figure 4-14. Proposed schematic diagram of the 85% TiO ₂ -ZnO/BAC1 photocatalyst.....	75
Figure 4-15. The possible mechanisms of self-sensitized 85% TiO ₂ -ZnO/BAC1 active species on degrading R6G dye.	76
Figure 4-16. Degradation of different dyes using 85% TiO ₂ -ZnO/BAC1.....	77

Figure 4-17. (a) Effect of pH on adsorption and photodegradation of R6G dye colour. (b) Degradation kinetics at different initial pH.	80
Figure 4-18. (a) Effect of 85%TiO ₂ -ZnO/BAC1 loading on R6G photodegradation. (b) Degradation kinetics at different photocatalyst loading.	81
Figure 4-19. (a) Effect of initial concentration on photocatalytic efficiency of 85%TiO ₂ -ZnO/BAC1. (b) Degradation kinetics at different initial concentrations.	82
Figure 4-20. (a) Effect of temperature on photocatalytic efficiency of 85%TiO ₂ -ZnO/BAC1. (b) Degradation kinetics at different temperatures.	83
Figure 4-21. A plot of ln K _L against 1/T for 70 ppm R6G dye adsorption by 85%TiO ₂ -ZnO/BAC1.	84
Figure 4-22. (a) Recycling runs in photocatalytic degradation of R6G over 85%TiO ₂ -ZnO/BAC1 composite. (b) XRD pattern of the composite before and after photocatalytic degradation of R6G dye.	85
Figure 4-23. Energy requirement for colour removal and COD reduction of the dyes using 85%TiO ₂ -ZnO/BAC1 at 1.3 g/L catalyst loading, pH 7 and 3.4 h reaction time.	86
Figure 4-24. The relation between the experimental and predicted global gas holdup at different superficial velocities and aspect ratio (AR).	90
Figure 4-25. Effect of reactor angle inclination on gas holdup (a) and mass transfer (KLa) (b) characteristic.	91
Figure 4-26. Particle distribution profile on solid loading at different gas superficial velocities.	93
Figure 4-27. Effect of inclination angle on particle distribution at different superficial gas velocities.	94
Figure 4-28. Model of flow scheme in an inclined column.	96
Figure 4-29. Effect of reactor inclination angle on photocatalytic efficiency.	98
Figure 4-30. Effect of lamp position on photocatalytic efficiency.	99
Figure 4-31. Effect of superficial gas velocity on photocatalytic efficiency.	100

NOMENCLATURE

Abbreviation

AC	Activated carbon
ARV	Anti-retroviral drugs
AOP	Advanced oxidation processes
AR	Aspect ratio
BAC	Activated carbon from banana peel.
BET	Brunauer-Emmett-Teller (m^2g^{-1})
BOD	Biochemical oxygen demand (mgL^{-1})
CB	Conduction band
COD	Chemical oxygen demand (mgL^{-1})
EC	Emerging contaminants
EU	European Union
FBR	Fluidized bed reactor
FTIR	Fourier transform infrared.
HOMO	Highest occupied molecular orbital
IA	Inclination angle ($^\circ$)
MB	Methylene blue
MG	Malachite green
NSAIDs	Non-steroidal anti-inflammatory drugs, and analgesics
LUMO	Lowest unoccupied molecular orbital
OFAT	One-factor-at-a-time

OTC	Over the counter medication
PCP	Personal care products
PL	Photoluminescence
PZC	Point of zero charge
R6G	Rhodamine 6G
SC	Semiconductor
SD	Standard deviation
SEM	Scanning electron microscopy
STR	Stirred tank reactor.
TGA	Thermal gravimetric analysis
TP	Transformation product
USFDA	United State Food and Drugs Administration
UV	Ultraviolet
V	Volume
VB	Valence band
WWTP	Wastewater treatment plant
XRD	X-ray diffractometer

Notation

A	cross-sectional area of the column (m ²)
A, B, n	Empirical constants
C _t	Concentration at time, t
C ₀	Initial concentration
C _f	Final concentration

E	Potential edge
E_0	Electrical energy per order (kWhm^{-3})
E^e	Free electron energy on the hydrogen scale
E_g	Energy band gap (eV)
H	Bed height (m)
H_{eb}	Expanded bed height
k	Apparent reaction rate constant
K_{La}	Gas-liquid mass transfer coefficient
M_s	Mass of the solid particle in the bed (kg)
P	Power (kW)
Q	Gas flow rate (m^3/h)
q_e	Adsorbed substrate at equilibrium
rpm	Revolution per minute
t	Time (min or hour)
$\Delta P/\Delta H$	Pressure gradient in the bed (Pa/m)
U_g	Gas velocity (ms^{-1})
U_{mf}	Minimum fluidization velocity (ms^{-1})
U_t	Terminal velocity (kg/m^3)
χ	Milliken electronegativity (eV)

Greek symbols

$\varepsilon_g, \varepsilon_L, \varepsilon_s$	Phase holdup
ρ	Density (kgm^{-3})
λ	Wavelength (nm)

ABSTRACT

Dyes are the main textile pollutant present in natural water bodies that pose a severe threat to human beings and other living organisms. To overcome dye wastewater pollution, Advanced Oxidation Process (AOP) especially UV photodegradation has been explored as a better alternative method over conventional treatment methods. However, UV photodegradation poses some shortcomings which impede its practical application. Among the photocatalysts, TiO₂ is widely used due to its better photocatalytic properties. However, TiO₂ requires some surface modifications and developments to improve its photocatalytic activity. To deal with it, the effectiveness of 85%TiO₂-ZnO/BAC1 (51:9:40) composite was investigated and evaluated as a novel photocatalyst for colour removal and Chemical Oxygen Demand (COD) reduction from aqueous solution under UV irradiation. The dyes used as a model pollutant in this study are methylene blue (MB), malachite green (MG), and rhodamine (R6G).

To enhance the photocatalytic activity, the TiO₂ surface was modified with ZnO and subsequently supported on banana peel activated carbon (BAC1), forming a composite referred to as 85%TiO₂-ZnO/BAC1. TiO₂ physicochemical properties before and after surface modification were characterized by X-ray diffractometer (XRD), Fourier transform infrared (FTIR), Scanning electron microscopy (SEM), Photoluminescence (PL), Thermal gravimetric analysis (TGA), Brunauer-Emmett-Teller (BET) and Laser diffraction technique. The catalysts performance and optimization of the operation conditions on colour removal and COD reduction of the dyes were determined in Lab-scale stirred tank reactor (STR) system under UV irradiation. From the study, 85%TiO₂-ZnO/BAC1 has demonstrated its potential as a promising photocatalyst for dye removal. It showed a higher colour removal of 95.7% compared to TiO₂, ZnO and 85%TiO₂-ZnO having 46.3%, 30.9%, and 55.5%, respectively under 50 mg/L initial dye concentration, 1.3 g/L photocatalyst loading, and 160 min UV irradiation conditions. The study revealed that UV photodegradation is more effective for colour removal of the dyes (MB, MG, and R6G) as compared to COD reduction, with about 95% and 70% reductions, respectively. The colour removal of R6G was still as high as 90% after four recycling runs, confirming the good stability and reusability of 85%TiO₂-ZnO/BAC1 composite. The photocatalytic mechanism of 85%TiO₂-ZnO/BAC1 has been proposed, as a hole (h⁺) and superoxide (O₂^{•-}) radicals as

primarily the main active species responsible for the degradation of R6G UV irradiation. Therefore, oxygen in the air used as a fluidizing medium is essential since it can trap electrons and consequently enhance $O_2^{\bullet-}$ formation and generation of h^+ .

The goal of this work was also to examine the applicability of 85%TiO₂-ZnO/BAC1 composite on the degradation of R6G dye in a fluidized bed reactor (FBR) system under UV irradiation. A preliminary hydrodynamic experiment was first conducted before the photodegradation experiment in the FBR system. From hydrodynamic experiments, the 90° inclination angle (reactor vertical position) resulted in a good gas holdup (ϵ_g), but poor particle distribution compared to 80°, 70°, 60°, and 50° inclination angles. Although the 70° inclination angle at superficial gas velocity (U_g) of 0.02405 ms⁻¹ showed a lower ϵ_g of 0.1597 compared to 90° and 80° with 0.2132 and 0.1791 respectively, it had good particle distribution and average ϵ_g . At 70° inclination angle and U_g of 0.02405 ms⁻¹ were found to be the optimum hydrodynamic conditions. However, photodegradation experiments, revealed that the optimum hydrodynamic conditions are at 0.01923 ms⁻¹ superficial gas velocity and 70° inclination angle of the reactor. From the study, it can be concluded that 85%TiO₂-ZnO/BAC1 composite shows great potential as a solution to textile dye wastewater treatment and environmental remediation. Moreover, this work may provide a reference for hydrodynamic conditions governing the photodegradation process for environmental mediation and economic concern.

CHAPTER 1

1 INTRODUCTION

1.1 Background

Water is life, and clean water means healthy living. Unfortunately, the current world still struggles with access to clean water due to water pollution. The rapid industrialisation and extensive consumption of non-biodegradable products perpetuated by an ever-increasing population have led to the widespread discharge of contaminants into the water bodies. The contaminants discharged include regulated and unregulated pollutants referred to as emerging contaminants (EC). Hence, this has posed an alarming threat to the natural environment. One of the many ECs are dyes, produced from sources such as textiles, paints, plastics industries etc. Despite the textile industry's huge economic impact, this industrial sector has been devastatingly polluting the environment and consumes large amounts of water, fuels and chemicals (Foo and Hameed, 2010). A huge volume of water, dyes and other chemicals are used during textile dyeing and finishing operations hence a large volume of wastewater containing dyes and other residuals are generated. Textile wastewater is usually a composite of chemicals, auxiliaries, surfactants, heavy metals, and organic dyes which contributes to high pH (8.2-9.6), Chemical Oxygen Demand (COD), Biochemical Oxygen Demand (BOD) and intense colour in water bodies (Santhana *et al.*, 2021). In the textile industry, the inefficiency of the dyeing processes and techniques release about 10 - 40% of the utilized dyes and about 75% of the salts resulting in highly coloured effluent and COD levels (Carr, 1995; Foo and Hameed, 2010).

Once in wastewater, dyeing chemicals are difficult to remove using conventional methods and instead these chemicals remain in the environment. The impact of dye wastewater ranges from decreasing sunlight penetration and impeding photosynthesis causing dissolved oxygen deficiency consequently, adverse effects on the entire aquatic biota (Hussain *et al.*, 2017). It is also noteworthy that the presence of dye in natural water bodies has led to the limitation on water beneficial use such as recreation, irrigation and even drinking water. The common widely used dyes such as malachite green, methylene blue and rhodamine are known to be carcinogenic and mutagenic, affecting the human immune and reproductive system (Hassanpour *et al.*, 2017;

Hussain *et al.*, 2017). In addition, dye wastewater contains heavy metals which are also known to be carcinogenic and mutagenic. Most of the dyes used have complex molecular structures and exhibit high solubility in water making them recalcitrant to conventional methods and environmental conditions (Lellis *et al.*, 2019). Therefore, it is particularly important to develop an effective and low-cost method to degrade dyes and other EC in wastewater to ensure environmental sustainability.

Various wastewater treatment methods have been widely employed to solve the water pollution problem caused by dyes. However, many dyes and other EC such as methylene blue, rhodamine 6G dye, and antibiotic oxytetracycline are resistant to conventional methods due to their non-biodegradability and recalcitrant nature (Singh *et al.*, 2020). Thus, new, and advanced treatment technologies especially Advanced Oxidation Processes (AOPs), are widely employed to minimize or completely degrade a wide range of recalcitrant pollutants over conventional methods. Considering green chemistry principles, it is key to utilize treatment processes that efficiently use minimum energy, low-cost and easily recyclable raw materials, and less generation of sludge or toxic by-products. Heterogeneous photodegradation is a preferred choice in the treatment of dye wastewater based on it meeting the fundamental principles of green chemistry (Singh *et al.*, 2020).

1.1.1 Dye water pollution

Over the years dyes are widely used in various industries including paints, textiles, printing, and paper. Dyes are primarily used to impart colour to a material. It is well known that natural dyes were replaced by synthetic dyes that bond with a material, giving a strong bright hue and colour-fast throughout washing and exposure to sunlight. Globally, it is estimated over 7×10^5 tons of synthetic dyes are produced annually and approximately 10% are lost to the environment during manufacturing and processing operations (Drumond *et al.*, 2013). Synthetic dyes are composed of different chemical compounds depending on the material being dyed. Among the widely used dyes in various industries are Malachite green, methylene blue dye and rhodamine 6 G dyes which are known to be detrimental to the environment. The industrial applications and toxicity of the dyes are summarized in Appendix A (Lellis *et al.*, 2019).

There are thousands of different dyes used in textile industries alone. Textile dyes are manufactured with several different chemicals to improve their bond and fixative

properties on the fabric, examples are chromium, nickel, and other metallic elements (Hussain *et al.*, 2017). Additives, auxiliaries, solvents, and chemical compounds are also used during textile treatment, dyeing, and finishing operations. Most notably the textile industry consumes a large volume of water and about 10 to 50% of dyes used are lost in the effluent during the dyeing and finishing stages due to the inefficiency of the operation. As a result, textile dye and chemical residuals eventually find their way into the environment without any prior effective treatment due to their resistant nature to conventional wastewater treatment methods and environmental conditions (Carmen and Daniel, 2012). Textile effluent composes of toxicants, salts, heavy metals, recalcitrant organics, and mainly coloured mass depending on chemicals and dyes used in the textile operations. The textile industry massive usage of water and chemicals coupled with extensive dye discharge is a key component of water pollution.

The detrimental impact of textile dyes on the environment includes aesthetic damage to water bodies, dissolved oxygen displacement and impaired photosynthesis and inhibition of plant growth. Most synthetic dyes are known to promote toxicity, mutagenicity and carcinogenicity through food chain and bioaccumulation (Lellis *et al.*, 2019). Moreover, many dyes and their transformation products upon degradation by an ineffective method are toxic to human health and aquatic life (Brigden *et al.*, 2013). Thus, the application of advanced, effective technologies for removing recalcitrant compounds such as textile dyes is therefore necessary.

For the treatment of textile dyes, various conventional treatments including physical, biological, and chemical methods have been used so far. However, these methods have limitations such as high cost of operation, ineffectiveness and being prone to secondary pollution (Foo and Hameed, 2010). An effective and efficient treatment method for dyes remediation is therefore required to enhance environmental sustainability.

1.1.2 Photodegradation

Among textile wastewater methods, AOP has a particular advantage over conventional treatments due to its ability to eliminate a wide range of recalcitrant organic pollutants and less generation of sludge. Briefly, AOP is based on the *in-situ* generation of free radicals linked to the chemical, catalyst, source of light, or their combination. The free radical with non-selective nature makes AOPs potent to mineralize any complex organic pollutant to simpler compounds. Despite AOP effectiveness, they are

considered costly based on energy input and chemical usage. In that context, photodegradation is regarded as a better alternative compared to other AOPs. Compared to homogenous, heterogenous photodegradation (photo-catalysis) offers additional advantages such as easy separation of the chemical material (e.g., catalyst) used from the aqueous solution since the process exists in different phases (Jean, 1999).

Presently, heterogeneous photocatalysis has aroused extensive interest in environmental remediation by providing a profound solution to overcome the problems related to separation, chemical and energy usage. This technique utilizes radiant energy, visible or ultraviolet (UV) light from artificial or natural sunlight sources to activate a catalyst (semiconductor). The absorbed photon by the catalyst induces charge separation, leading to the formation of reactive oxygen species responsible for oxidation and mineralization of the organic pollutants. Along with other advantages, heterogeneous photodegradation is relatively independent of pH adjustment and is operated under ambient temperature and pressure (Gaya and Abdullah, 2008).

1.1.3 Semiconductor as photocatalyst

Among semiconductors used as photocatalysts, TiO₂ has been extensively studied due to its high efficiency, low cost, physical and chemical stability, non-corrosiveness, and widespread availability (Chong *et al.*, 2010). TiO₂ has proven to degrade a wide variety of organic and inorganic water pollutants. Due to TiO₂ wide-bandgap crystalline structure (3.0-3.2 eV), it is efficiently photoactivated under the UV spectrum range compared visible light region. However, TiO₂ photocatalytic activity is restricted due to the low quantum yield of excitons and screening of incidence light from the active centres caused by the rapid recombination and aggregation of nano-sized particles, respectively. To overcome this, one of the approaches used has been coupling TiO₂ to another semiconductor like ZnO. Enhanced photocatalytic performance under UV has been observed for p-n heterojunctions formed in TiO₂ coupled with ZnO (Benton *et al.*, 2016). The improved photocatalytic activity due to the synergistic effect is mainly attributed to the prolonged electron-hole pairs recombination and reduced aggregation.

Besides, one main practical drawback to overcome is to recover TiO₂ from treated water which is an environmental and economic concern. To solve the separation problem, two potential strategies including immobilization on the support material and the use

of an external magnetic field have been widely studied (Li *et al.*, 2016; Wang *et al.*, 2016). Compared to the magnetic field approach, immobilization on support material has received huge attention for overcoming multiple fundamental shortcomings including adsorption capacity, aggregation tendency and recovery of TiO₂.

1.1.4 Activated carbon as support material.

Taking advantage of immobilization onto a support technique, promising efforts have been made on supporting catalyst on an adsorbent i.e. silica aerogel (Li *et al.*, 2016; Wang *et al.*, 2016), zeolite (Castañeda-Juárez *et al.*, 2019), clay (Tobajas *et al.*, 2017; Zyoud *et al.*, 2020) and activated carbon (Benton *et al.*, 2016). Immobilizing a catalyst onto an adsorbent concentrate the target pollutant around the surface of the active sites, consequently improving the photocatalytic activity. Among the supports used, activated carbon (AC) is very promising for synergistic reasons mainly reducing aggregation, increasing the adsorption of O₂ and subsequently accepting the electrons (Benton *et al.*, 2017). Most importantly supporting a catalyst on activated carbon reduces the cost associated with post-treatment catalyst separation.

Beyond the adsorption capacity, cost is one of the factors used to compare different adsorbents. The factors affecting the cost of adsorbent varies from the availability of the raw material and the preparation process. Considering the above factors, attention has been focused on the development of adsorbent support from agricultural and industrial by-products. Between the two, agricultural waste has been proven to be renewable, readily available, eco-friendly and low cost compared to other materials used as a source of an adsorbent (Yousuf *et al.*, 2019). Banana is a widely consumed fruit in the world and a huge amount of peels are dumped in landfills causing environmental problems through the emission of foul odour when left to decompose. Banana peels converted to AC, used as catalyst support helps to reduce both the economic and environmental problems. The use of an adsorbent from agricultural banana waste has multiple benefits including wastewater treatment and agricultural waste management.

1.2 Motivation/Purpose

Dyes are extensively used in different industries, especially textiles. Apart from the huge economic contribution, textile industries are also considered one of the major

causes of environmental deterioration due to their continuous discharge of undesirable textile chemicals, especially dyes that are difficult to degrade. The textile industry is known to utilize a large amount of water but generates a wide range of chemicals originating from its processing stages, mainly washing, bleaching, and finishing. In particular, the dyeing stage is vital in the textile process. However, about 10-50% of the total dye used remains unreacted and eventually become part of the effluents since they are also recalcitrant to conventional wastewater treatment methods. The textile effluents are generally characterised by high pH (8.2-9.6), strong odour, colour, and high chemical complexity, thus are difficult to be degraded by conventional wastewater treatment methods. Even in small concentrations (1 ppm), dye hinders light penetration in water, inhibiting photosynthesis and causing oxygen reduction in the aquatic environment, leading to death.

Moreover, some textile dyes and their metabolites upon degradation are known to be toxic to public life. Due to the recalcitrant nature and continuous widespread organic pollutants generated from dyes and textile auxiliaries, this has become a major global environmental pollution challenge. Therefore, the application of advanced treatment methods such as heterogeneous photodegradation, on textile dye wastewater abatement, is crucial to protect the environment. Moreover, effective treatment of textile wastewater allows the reuse of water in some textile industry processes, construction, or irrigation purpose.

1.3 Problem statement

The high demand for products perpetuated by the ever-increasing population has led to the large production of dyes used in many industries. Industries including paints, paper, textile, and others use different synthetic dyes to colour their products while using large volumes of water. Wastewater discharged to the water stream from textile industries carries a host of different chemicals mainly dyes. Dye discharged into different water streams has led to major problems such as increased toxicity, dissolved oxygen displacement and subsequently reduced photosynthesis rate resulting in a negative impact on the aquatic biota. The colourization is undesirable, limiting downstream beneficial use such as recreation, drinking water etc. A small concentration of dyes (1 ppm) is highly visible hence, regarded as a firsthand challenge.

With a view to suppress the increasing dye water pollution, conventional methods such as physical, chemical, and biological have been widely used. However, these methods suffer from various drawbacks thus AOP is regarded as a better alternative particularly for the treatment of recalcitrant contaminants. Based on the fundamental principles of green chemistry, UV heterogeneous photodegradation presents an opportunity to improve the environmental sustainability of water treatment. In this technique, TiO₂ has been widely used based on both cost and photocatalytic properties. Due to the wide structural bandgap (3.0-3.2), TiO₂ is efficiently activated upon UV irradiation which accounts for less than 5% of solar energy, thus an external source of UV energy is required. Upon UV irradiation, TiO₂ may experience rapid electron-hole recombination effect and aggregation due to structural bandgap and instability of nanosized particle and consequently reduce its photocatalytic activity. In principle, coupling TiO₂ to another semiconductor like ZnO is vital to reduce recombination, constrain aggregation, and consequently achieve a higher photocatalytic activity.

Besides, TiO₂ catalysts also suffer some technical barriers mainly separation and reusability which are regarded as an economic and environmental concern. To further extend the application and reusability of TiO₂ catalysts, supporting it on the material is therefore necessary. Using activated carbon as TiO₂ support seems useful due to multiple synergistic reasons including reduced aggregation effect, increased absorption of O₂ and increased adsorption of the target pollutants (Benton *et al.*, 2017). Most importantly, using activated carbon support from banana peels reduces the cost of chemical usage since it is readily available and requires a simple preparation method. Using agricultural waste as a source of support offers economic and agricultural waste management advantages. AC increases the overall photocatalytic activity of TiO₂, but the composite may experience a reduction in the subsequent activity cycle due to the detachment of the support from the catalyst. The use of colloidal silica as a binder enhance cohesion between the support and catalyst, hence promoting recoverability and activity of the subsequent cycles.

Although the introduction of a support approach provides a facile way to solve adsorption and separation problems, the photocatalytic activity of TiO₂ is normally impeded. This could result in reduced surface area to volume ratio, decreased substrate mass transfer and the light-shielding effect caused by inactive supports. The optimum

mass of the support on the catalyst ensures most of the substrates are photodegraded but not just adsorbed on the surface of the catalyst. Moreover, the design of a photo-reactor that can guarantee catalyst surface availability and superior mass transfer is therefore important.

Designing an efficient and feasible photoreactor is the most challenging task in achieving an effective photocatalytic process. A photocatalytic reactor is classified into two main configurations based on the location of the photocatalyst. That is a slurry-type reactor with suspended photocatalysts and a reactor with the photocatalyst immobilized onto a support carrier. The slurry reactor configuration usually offers significant advantages over immobilized catalyst-type reactor due to its high total surface area of photocatalyst per unit volume and superior mass-transfer properties. However, the main limitation of slurry-type photo-reactor applications is that it requires additional post-treatment separation processes thus increasing the operational costs. To overcome this limitation, operating in a fluidized bed reactor (FBR) is the preferred choice upon using a supported photocatalyst. FBR provides a possibility of ensuring catalyst availability towards the source of light and maximum substrate mass transfer. In a three-phase fluidized bed reactor, more efficient charge separation is achieved by oxygen in the air (as a fluidizing medium) prolonging recombination, favouring the photocatalytic activity. A photo-reactor was designed, and its hydrodynamics were evaluated to ensure an effective photocatalytic activity.

1.4 Aim and specific objectives.

The main aim was to prepare a low-cost photocatalyst ($\text{TiO}_2\text{-ZnO/BAC}$) with multi-potent characteristics to degrade various textile dyes under UV irradiation. The characteristics include adequate adsorption capacity, improved photocatalytic activity, physicochemical stability, and reusability. The specific objectives of this study were:

- i. To prepare and characterize pure, hybrid, activated carbon as support from the banana peel (BAC) and composite photocatalysts of TiO_2 , ZnO and BAC.
- ii. To examine the degradation performance of the dye(s) using synthesized photocatalyst material.
- iii. To analyse kinetics based on hybridization and support composition onto the catalyst.

- iv. To determine operational parameters and kinetics, namely pH, catalyst loading, initial concentration, temperature, catalyst reusability, and energy requirement.
- v. To fabricate a UV photoreactor for the photodegradation process.
- vi. To evaluate hydrodynamics parameters affecting adsorption and photocatalytic performance of the photocatalyst composite.

1.5 Research questions

- i. What are the physicochemical properties of TiO₂, ZnO, BAC, TiO₂-ZnO hybrid and TiO₂-ZnO/BAC materials?
- ii. How is the performance of TiO₂ on the degradation of dyes affected by ZnO hybridization and the introduction of banana peel activated carbon (BAC)?
- iii. What is the effect of operation parameters on the activity and degradation kinetics of TiO₂-ZnO/BAC?
- iv. What is the effect of hydrodynamic parameters based on gas hold up and solid distribution on the activity of TiO₂-ZnO/BAC composite?

1.6 Thesis overview

This Masters dissertation aim is to fill out the major knowledge gap that needs to be addressed to ensure the successful application of AOP heterogeneous photodegradation for wastewater treatment based on economic and safety concerns. The study aimed to conduct a series of experimental studies and address the challenges posed by TiO₂ photocatalytic activity. It further considered the mitigation of the drawbacks in order to solve the environmental problem considering safety and economic concerns. The general experimental work covered in this dissertation is depicted in Figure 1-1.

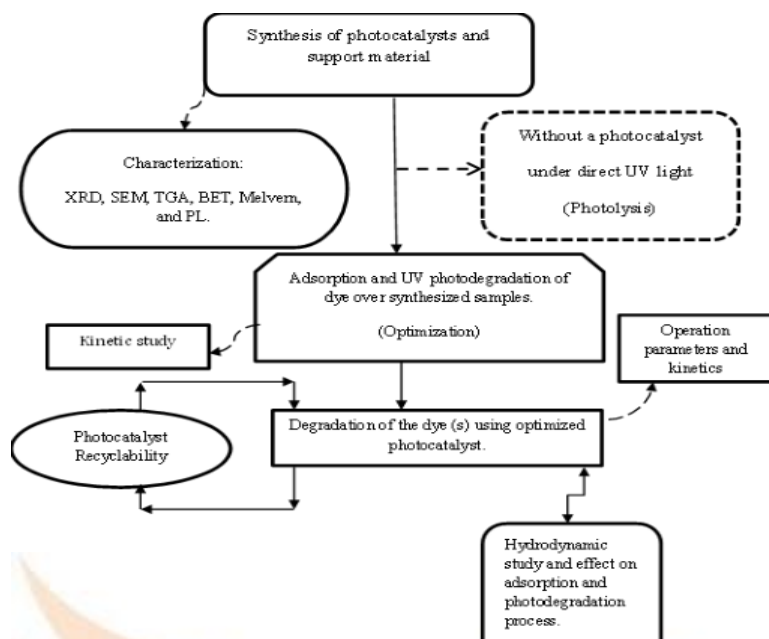


Figure 1-1. Work outline subjected to this study.

The overall thesis framework is divided into five main chapters, summarized as follow: **Chapter 1** outlines the introductory section, especially the background of water pollution and the photodegradation process over other wastewater treatment technologies, motivation/purpose, problem statement, aim, specific objectives, and general work overview of the study. This chapter is further explained in detail in the literature review chapter. **Chapter 2** presents a review of literature on water pollution, which is rapidly changing. New and advanced wastewater techniques especially Advanced Oxidation Processes (AOPs) are employed to remove recalcitrant contaminants such as dyes and pharmaceuticals as potential emerging contaminants. Heterogeneous photocatalysis (UV/ TiO₂) is reviewed as a better alternative than conventional methods and other AOPs based on environmental concerns. Moreover, the limitations and countermeasures of TiO₂-based photocatalysis are also discussed. Furthermore, the efficient photoreactor and hydrodynamic conditions are discussed. **Chapter 3** is composed of the methodology and materials used to achieve the objectives subjected to this work. In this chapter, material preparation, material characterization, experimental design, and experimental setup are explained in detail based on the literature review. **Chapter 4** entails results and a discussion of the work conducted in this study. The results obtained including characterizations, photocatalytic

performance, operation parameters, and hydrodynamics study are discussed based on scientific and engineering perspectives. **Chapter 5** summarizes the key conclusions, describes the engineering significance of the study and suggests critical recommendations for future work.



CHARTER 2

2 LITERATURE REVIEW

With rapid industrialization and extensive consumption of non-biodegradable compounds, emerging contaminants and other pollutants are presently a serious concern in pollution control. The potential emerging contaminants (EC), such as residuals of textile dyes, pharmaceuticals, personal care products, etc., are being discharged into surface waters due to their recalcitrant nature towards conventional physical, chemical, and biological methods and generation of secondary pollution (Foo and Hameed, 2010). Therefore, this has created the need to develop new techniques to remove the EC and other recalcitrant pollutants. Advanced oxidation processes (AOPs) as effective alternative water treatment technologies are therefore required to remove recalcitrant compounds (Miklos *et al.*, 2018). However, AOPs tend to be more costly than conventional methods due to the high input of chemicals and energy required. Thus, AOPs, mainly heterogeneous photodegradation, is considered a better alternative than conventional methods and other AOPs based on economic and environmental concerns.

2.1 Emerging contaminants pollution

Emerging contaminants (ECs) are unregulated compounds with limited information on their ecotoxicology but has the potential adverse effect on ecological or human health (Farré *et al.*, 2008; Luo *et al.*, 2014). The continuous widespread and improper daily use of so-called ECs has become a common trend that needs to be avoided or controlled. ECs found in water bodies comprise agricultural products, personal care products, endocrine-disrupting hormones, textile dyes etc. Based on water quality regulation standards, textile industries have been currently identified as high priority industries creating a considerable impact on water pollution due to the large volume discharge of toxic chemicals, above all dyes.

2.1.1 Agricultural pollution

Recently, many agricultural chemical inputs are also considered potential sources of EC. Ever-increasing food demand has led to unsustainable agricultural practices thus, posing a severe risk to the biota. Agricultural activities greatly contribute to the non-point source of water pollution. Many agrochemicals such as fertilizers, pesticides,

insecticides, and other agricultural chemical inputs end up in water bodies through runoff or leaching (Zhang *et al.*, 2019). Moreover, the major concern of unsustainable agricultural practices to the general ecosystem is excretory livestock waste containing veterinary medicine (hormones and antibiotics), commonly used as manure or fertilizers (Paíga *et al.*, 2016). Minimizing or controlling agricultural pollution poses some serious challenges since they originate from different sources such as farmyards, livestock herds, poultry farms, and lawn gardens.

To deal with agricultural pollution, Chen *et al.* (2017) proposed that the imposition of pollution taxes and employing agricultural subsidies, mainly innovation subsidies can reduce agricultural pollution and lead to sustainable production. Therefore, such an economic approach can significantly result in sustainable agricultural practices and prevent agricultural pollution.

2.1.2 Personal care products pollution

Personal care products (PCP) are household products used in modern daily life for hygiene and beautification purposes, e.g., soap, detergents, and cosmetics. The residual PCPs usually enter the water supply as a result of brushing, bathing, or washing. Some of these PCPs contains harmful ingredient compounds, for instance; phthalates (as a plasticizer, solvent, and fragrance ingredient in soaps, hair sprays, and perfumes), triclosan (as preservatives in toothpaste, shaving, and colour cosmetics), siloxane (as a softener and moisturizer in hair products and deodorants), formaldehyde (as a preservative in eyelash glue, baby shampoo, body soap, hair gel, and nail polish), organic UV filters (blocking or absorbing UV in lipsticks, body cream, and lotions) and parabens (as a preservative in shampoos, conditioners, facial and shaving products). Various research has demonstrated the presence of regularly used PCPs in the environment; triclosan (Bedoux *et al.*, 2012), phthalates (Gao *et al.*, 2016), siloxane (Tran *et al.*, 2019), organic UV filters (Balmer *et al.*, 2005) and parabens (Renz *et al.*, 2013). The reported concentration of such PCPs usually ranges from $(10^{-9}) \text{ gL}^{-1}$ to as low as $(10^{-6}) \text{ gL}^{-1}$ however, ecotoxicology effects at low concentration of some of these PCPs referred as EC is still undetermined. Moreover, widely used ingredients in PCPs including bis(2-ethylhexyl) phthalate, Triclocarban {3,4,4'-trichlorocarbanilide} (TCC) and triclosan {5-chloro-2-(2,4-dichlorophenoxy)} phenol (TCS) are already blacklisted as priority water pollutants by the U.S. Environmental Protection Agency (Planelló *et al.*, 2011).

Various studies have shown the ecotoxicology effect of several PCP ingredients on biota. For instance, endocrine-disrupting contaminants are phthalates; (Horn *et al.*, 2004), paraben (Nowak *et al.*, 2018), siloxanes (Helm *et al.*, 2019), and mutagenic and carcinogenic are phthalates (Caldwell, 2012), and formaldehyde (Reingruber and Pontel, 2018) etc. To date, the extensive demonstration of PCP ecotoxicological effects has led to increasing concerns about their fate and as well as effective removal methods.

2.1.3 Endocrine-disrupting hormones pollution

Endocrine-disrupting hormones are any natural or synthetic substances that can potentially affect the endocrine systems (normal hormonal functions) and physiology of an organism when exposed to its ecosystem. The disruptions may lead to severe adverse conditions like cancer, DNA alteration, reproduction defects, and developmental disorders. Several research studies have demonstrated many EC and their transformation products (TPs) frequently detected in water can cause endocrine disruptions to different organisms. The primary examples are textile dye (Brigden *et al.*, 2013), pesticides and their TPs (Huang *et al.*, 2020; Segura *et al.*, 2015) and chloramines used as swimming disinfectants (Richardson *et al.*, 2007) etc. Therefore, it is a growing concern that the biosphere is being exposed to endocrine-disrupting hormones which require an urgent and sustainable response.

2.1.4 Pharmaceutical pollution

Pharmaceuticals are specially designed synthetic or natural chemical compounds used to prevent, control, treat and improve health (Jelic *et al.*, 2011). Since most of the drugs exist as pro-drugs, they tend to undergo incomplete biotransformation, or some might persist in the process. Therefore, they end up being excreted either as in their slightly transformed form or parent form by the human body. To date, almost all groups of pharmaceuticals widely used have been detected in the aqueous environment. The main examples are non-steroidal anti-inflammatory drugs (NSAID), anti-retroviral drugs (ARV), antibiotics, antiepileptic drugs (K'oreje *et al.*, 2012), and steroid hormone (Manickum and John, 2014). ARVs and NSAIDs are mostly reported in the Sub Sahara Africa aquatic environment (K'oreje *et al.*, 2016; Madikizela *et al.*, Chimuka, 2017).

The slightly changed or parent form of excreted drugs end up in wastewater treatment plants (WWTPs) via sewage pipes or sewer vacuum trucks. Since WWTPs are incapable of completely degrading the pharmaceutical drugs via conventional sewage

treatment processes, the drug residuals are eventually discharged, thus polluting water resources (Nieto-Sandoval, 2018). Besides pollution from WWTP discharge, other routes of pharmaceutical contamination include the direct release of human waste due to poor or no sanitation process, leakages and overflow of sewage pipes and septic tanks, animal excretory waste, and veterinary drugs and usage of animal waste or WWTPs as fertilizer (Paíga *et al.*, 2016; Segura *et al.*, 2015).

Some studies have even confirmed the detrimental effect on vultures feeding on the animal carcass with DCF residue (Taggart *et al.*, 2007). The combination of any drugs or other chemicals can be potentially lethal to living organisms. For instance, the combined occurrence of DCF, ibuprofen, naproxen, and acetylsalicylic acid in water has been confirmed to exhibit a more toxic impact due to a synergistic effect (Cleuvers, 2004). Bottoni *et al.* (2015) also demonstrated that the zidovudine ARV drug could be potentially carcinogenic. At present, several studies have shown the presence of various types of ARVs in water systems (K'oreje *et al.*, 2016; Madikizela *et al.*, 2017). Amino *et al.* (2018) reported that some ARVs transform into a resistant strain during wastewater treatment. Others such as nevirapine and zidovudine tend to be very stable even under WWTP processes. Besides, the current WWTPs inefficiency, improper or no sanitation, and unlawful disposal of drugs (unused or expired), can also be the source or route to pharmaceutical contamination of water systems (Segura *et al.*, 2015). Especially in Africa, due to improper or no sanitation, has led to a wide variety of pharmaceutical contamination, mainly ARVs and NSAIDs in water bodies (K'oreje *et al.*, 2012; Madikizela *et al.*, 2017). Therefore, the application of a robust treatment method in WWTP is important. Moreover, the disposal of unused or expired drugs needs to be controlled.

2.1.5 Textile dyes pollution

Despite the undisputed global economic impact, the textile industry discharges a huge amount of chemicals into the environment. An urgent concern is placed on the enormous use of drinking water in textiles operations such as washing, bleaching and above all dyeing, instead of discharging a host of toxic chemicals. The liquid and solids effluents from the textile industry are responsible for creating an extensive catastrophic impact on the environment (Lellis *et al.*, 2019). The main environmental impact caused by the textile industry is its untreated effluent discharged into the water bodies. Textile wastewaters compose of many different chemicals including dyes, surfactants, heavy

metals, and auxiliaries. Most of the textile effluents are characterized by relatively high levels of BOD, COD, pH, and intense colour depending on the chemicals used. In the textile industry, about 40% of the dyes used are lost to effluents during the dyeing and finishing operation, due to the inefficiency of the processes (Carr, 1995). In addition to that, most dyes escape conventional treatment processes and eventually to the environment due to their high stability in various environmental conditions.

Currently, the textile industry has replaced natural dyes with synthetic dyes not only due to the increasing demand for the dye material but also to their strong hues and colour-fast on materials. The use of synthetic dyes has prompted a serious environmental impact. The colour-fast as a result of the fixative property of a dye is attributed due to the presence of auxotrophic groups in its molecular structure (Lellis *et al.*, 2019). This property makes it stable through washing and sunlight. Due to the combined high solubility and fixative properties, dyes are difficult to be degraded using conventional methods. The government and some agencies try hard to put countermeasures and standards based on industrial production and discharge. However, some industrial pollutants can be difficult to regulate through legislation or conventional methods. Therefore, this problem can further be resolved by applying an appropriate and effective wastewater treatment process.

2.2 Waste treatment methods

Common wastewater treatment typically involves conventional physical, chemical, biological processes, or combinations of these processes. Such conventional treatment methods have been used over several decades for removing pollutants based on environmental and public health concerns (Lellis *et al.*, 2019). Due to their ineffectiveness and inefficiency, new and advanced treatment methods have emerged with improved performance to remove pollutants showing persistence to conventional treatment methods. More recent, AOPs such as ozonolysis, photo-Fenton, photocatalysis, etc., are considered more effective than conventional methods. Nevertheless, all AOPs have individual shortcomings (Miklos *et al.*, 2018).

2.2.1 Conventional treatment method

Conventional wastewater treatment consists of physical, chemical, and biological operations to transform raw wastewater into a product safe to discharge. Typically, it involves four sequential stages, which are as follows: a) Preliminary treatment/Prior

treatment stage, b) Primary treatment, c) Secondary treatment, and d) Tertiary and advanced wastewater treatment (Appendix B). Tables 2-1, show summarized advantages and disadvantages of different conventional treatment methods for dye removal under the main classification including physical, chemical, and biological (Foo and Hameed, 2010).

In preliminary treatment, coarse solids and any other large raw wastewater materials are removed to ease operation and enhance maintenance of the subsequent treatment stages. Preliminary treatment operations include coarse screening using bar screens (rags and large debris removal) and subsequently, grit removal (sand, silt and, grit) via sedimentation. Moreover, the comminution of large materials is done mostly to improve coarse screening capabilities. The second stage, primary treatment, involves removing organic and inorganic sediments and suspended materials (scum) through sedimentation and skimming, respectively. Like preliminary treatment, primary treatment is vital since it also prevents damage and clogging of downstream subsequent treatment units. The third stage, secondary treatment, is designed with physical phase separation to remove sediment materials and a biological process to degrade the sewage organic content. In this stage, indigenous and aquatic microorganisms under aerobic or anaerobic ecosystems usually perform the biological degradation function. However, due to some compound recalcitrant nature, especially textile dyes and pharmaceutical compounds, secondary treatment is incapable of degrading them. Thus, robust, and more advanced treatment is often preferred (Foo and Hameed, 2010; Miklos *et al.*, 2018).

Tertiary (or referred to as advanced wastewater treatment) is a final treatment stage usually applied to remove persistent contaminants during the secondary treatment stage. This final stage is usually done to improve the effluent quality before being reused or discharged into natural surface water bodies. More than one tertiary treatment plant at any treatment plant, such as a combination of biological and physiochemical processes, can be applied to improve treatment efficiency. Most of the existing wastewater treatment plants (WWTP) are usually equipped with conventional treatment processes. Therefore, they are incapable of dealing with highly polar micro-pollutants and non-biodegradable compounds like dyes and pharmaceutical residues. As a result, such pollutants in WWTP received from textile, pharmaceutical industries, pharmacies, veterinaries, and households eventually end up in the environment (Tong *et al.*, 2011).

The conventional methods are known to be ineffective and inefficient to degrade recalcitrant organics completely and toxic pollutants. Therefore, more robust treatment processes with improved performance, especially AOPs, have greatly received enormous attention.

Table 2-1. Advantages and disadvantages of conventional methods for the treatment of dye wastewater (Foo and Hameed, 2010).

Classification	Methods	Advantages	Disadvantages
Physical and physiochemical	Adsorption	Removes a wide range of dyes. Easy handling process.	Transfer of pollutants from one phase to another leads to secondary pollution. Nonselective to dye pollutants.
	Electro-kinetic coagulation	Economical feasible	High sludge production
	Coagulation-flocculation	Effective for insoluble dyes.	Secondary pollution Increased sludge generation Requires adjunction of non-reusable chemicals (coagulants and flocculants)
	Irradiation	Effective for dye removal at low volumes.	Requires a lot of dissolved oxygen. Ineffective for light stable dyes.
	Membrane filtration	Remove all types of dyes. Optimal reduction of COD and salinity.	High setup cost and periodic replacement of membrane. Concentrated sludge production Insufficient quality for reuse of treated permeate. Requires pre-treatment of feed water, optimization of chemical, operation conditions (pH and recovery ratio) and modification of the membrane surface to avoid fouling. Fouling of the membrane affects its efficiency.
	Nanofiltration	Remove mineral salts and hydrolyse reactive dyes and auxiliaries residuals. Relative low pressure required 5-40 bars	Unable to separate soluble elements from water. Membrane fouling
	Ultrafiltration or microfiltration	Low-pressure process (3.5-16 bar)	
	Reverse osmosis	Ability to separate mineral salts and	A large amount of water, high pressure

		hydrolyse reactive dyes and auxiliaries.	(7-100 bars) is required. Prone to fouling with a high concentration
Biological	Anaerobic	Effective on decolourization by breaking down cleavage linkages of azo dye.	Production of methane and hydrogen sulphide gas. Slow process. Low biodegradability due to electrophilic propriety of -N=N- bond especially in azo dye.
	Aerobic	Effective on the degradation of the aromatic amines in the dyes.	High energy consumption for aeration. Not suitable for low BOD: COD (0.3:0.4) effluent.
	Fungal, bacterial, or algal process	Effective for low volumes and concentration of dyes. Colourant substrate selectivity.	Not applicable for large volume waste. High cost on culture maintenance.
	Activated sludge.	Produce energy from biogas. High effluent quality	High cost of maintenance. High CAPEX and OPEX. Production of flammable biogas requires proper handling.
Chemical	Chemical oxidation	Simple process	Activation of the oxidizing agent H ₂ O ₂ is needed.
	Chemical precipitation	Efficient for metals removal in dye like chromium. Effective for COD reduction.	High sludge production. High chemical consumption.
	Electrochemical	No use of chemicals and no sludge generation.	High cost of energy. Relative high flow rate affects its dye removal efficiency.
	Ion exchange	High sorption capacity for different dyes. Allow regeneration with no adsorbent loss. Not affected by water turbidity.	Specific exchange resins are required depending on the type of dye.
	Photochemical (H ₂ O ₂ /UV)	No sludge generation. Suitable for both decolourization and reduction of foul odours.	Formation of toxic intermediates. Require an external source of light to activate the oxidizing agent.
	Sodium hypochlorite destruction	Initiate and accelerate azo-bond cleavage of the dye.	Generation toxic intermediate mainly aromatic amines.

2.2.2 *Advanced Oxidation Processes*

Over the years, Advanced Oxidation Processes (AOPs) have significantly been considered an alternative effective wastewater treatment method for removing recalcitrant pollutants with low biodegradability and high chemical stability contents. AOPs are known as relative eco-friendly techniques employed to remove a wide range of organic and even some inorganic compounds in the water matrix through chemical oxidation with very reactive hydroxyl radicals ($\bullet\text{OH}$) or other reactive species (Miklos *et al.*, 2018). All AOPs greatly depend on the generation of $\bullet\text{OH}$ radicals and other reactive species linked to chemical material, source of energy utilized, or both. Hence, AOPs are mainly classified based on primary oxidants (ozone or hydrogen peroxide), iron, energy source (UV or visible light), catalyst, or their combination used in chemical processes to produce $\bullet\text{OH}$ (referred to as in-situ chemical reaction). The one unpaired e^- on $\bullet\text{OH}$ generated makes it more unstable and very reactive with a rate constant of more than $10^6\text{M}^{-1}\text{s}^{-1}$ (Luo *et al.*, 2018). Therefore, $\bullet\text{OH}$ radicals are likely to degrade almost all types of toxic organic pollutants in water into intermediate and subsequently into final less toxic products. AOPs are comparatively better than conventional methods due to their high treatment efficiencies and effectiveness. Besides AOP effectiveness, almost all types of AOPs exhibit individual shortcomings. For instance, the utilization of primary oxidants like ozone and hydrogen peroxide are likely to generate highly toxic by-products such as bromates and residual hydrogen peroxide, respectively (Wang and Zhuan, 2020). Furthermore, the utilization of UV as an external source of energy can make AOPs large scale operation costs high due to the high consumption of external energy sources.

AOPs major categories, homogeneous, and heterogeneous processes widely investigated are based on the contaminant and the chemical material existence phase. The heterogeneous process uses catalysts in a solid state to degrade pollutants in an aqueous state. In homogeneous process, both the contaminant and chemical material (e.g., catalyst) exist in the same phase, mostly aqueous state (Babuponnusami and Muthukumar, 2014). The heterogeneous processes offer additional advantages compared to the homogeneous processes by allowing easy separation of the catalyst or chemicals used from the aqueous solution since they exist in a different phase.

i. Homogeneous processes

The homogeneous process involves utilizing dissolved chemicals (same phase) in wastewater in the absence or presence of energy from various sources like UV radiation, ultrasound (US), or electrical power to remove pollutants. The UV-driven processes are O₃/UV, H₂O₂/UV, O₃/H₂O₂/UV, photo-Fenton/H₂O₂/UV, ultrasound driven processes are O₃/US and H₂O₂/US (Miklos *et al.*, 2018). The electrical-driven processes are electrochemical oxidation, anodic oxidation, and electron-Fenton. While in the absence of an energy source, they include O₃, O₃/H₂O₂, and H₂O₂/catalyst. All the mentioned above processes have been extensively studied and reported to exhibit individual advantages and disadvantages (Miklos *et al.*, 2018).

The established homogeneous AOPs in large-scale wastewater treatment involve utilizing ozone (O₃), H₂O₂, Iron (Fe²⁺ or Fe³⁺), and UV or their combination. Homogeneous AOP, especially the ozonation process, has drawn more attention due to its high standard redox potential and relatively eco-friendliness. Nevertheless, its application is constrained because of selective oxidation between O₃ and pollutants and the formation of intermediates due to incomplete mineralization of some organic compounds (Nawrocki and Kasprzyk-Hordern, 2010; Orge *et al.*, 2017). Liu *et al.* (2010) reported that UV radiation might induce complete mineralization that surpasses ozone treatment due to the decomposition of ozone. Thus, the O₃/UV process is regarded as a more effective treatment method than individual O₃ and UV for the degradation of pollutants (Fu *et al.*, 2015). Although Yuan *et al.* (2015) found that the H₂O₂/UV process has higher degradation efficiencies because of the high solubility of H₂O₂, resulting in the generation of a high amount of •OH. The major disadvantage is that H₂O₂ has poor absorbance in the UV range. Thus, most of the UV light applied goes to waste. Therefore, the installation of reflectors to reflect the unabsorbed light is needed making all processes complicated and costly (Navntoft *et al.*, 2008). Since in AOPs, total mineralization greatly depends on •OH, the combination of O₃/H₂O₂/UV can enhance •OH generation. However, O₃/H₂O₂/UV is more expensive based on chemical usage and external UV energy sources. In general, the utilization of oxidizing agents such as O₃ and H₂O₂ may lead to secondary pollution due to the formation of bromates and toxic H₂O₂ residuals (Wang and Zhuan, 2020). Although Fenton/photo-Fenton is also considered a highly competitive treatment method, it is costly due to chemical usage and energy input. It may also lead to secondary pollution in terms of acidic discharge and large amounts of iron ions (Fe²⁺ or Fe³⁺). Furthermore, other AOPs

driven by ultrasound or electrical as the energy source suffer a significant limitation of high energy consumption (Mahamuni and Adewuyi, 2010). In general, all homogeneous AOPs applications can be costly since they require a post-separation process of the chemical used and treated wastewater existing in the same aqueous phase.

ii. Heterogeneous processes

The heterogeneous process uses catalysts in a solid state to degrade contaminants in an aqueous state. Examples are catalytic ozonation, photocatalytic ozonation, photocatalysis, etc. The heterogeneous process is a preferred choice compared to the homogeneous process due to the easy separation of the catalyst or chemicals used from the aqueous solution since they exist in different phases. The separation of chemicals used from treated water is vital for both economic and environmental concerns.

Heterogeneous catalytic ozonation is more effective than sole ozone due to the presence of a catalyst that facilitates ozone decomposition (Yan *et al.*, 2013). Unlike other ozone-based treatment processes, catalytic ozonation can be operated in the absence of an energy source and under a wide range of pH. Thus, it can be relatively economical based on energy input and chemical usage.

Moreover, the total mineralization of organic pollutants significantly depends on the generation of a sufficient amount of $\bullet\text{OH}$ radical (Miklos *et al.*, 2018). A profound effect has been made on integrating different treatment methods to achieve higher mineralization. Parrino *et al.* (2015) demonstrated a higher degradation of pollutants through photocatalytic ozonation. However, photocatalytic ozonation requires additional energy and ozone usage. Therefore, making the process costly based on energy input and chemical usage. Based on effectiveness, economic and environmental concern, heterogeneous photocatalysis stands a chance to be a better alternative treatment method compared to other AOPs (Miklos *et al.*, 2018).

2.3 Heterogeneous photocatalysis

Heterogeneous photocatalysis typically involves a series of reductive and oxidative reactions by a catalyst, usually a semiconductor. Typically, a photocatalyst is activated via the absorption of sufficient photon energy equal to or higher than the absorption bandgap energy of the catalyst (Carp *et al.*, 2004). The absorbed photons induce the

promotion of electron (e^-) from the valence band (VB) to the conduction band (CB), leaving an unfilled electron-hole (h^+) on the VB of the semiconductor. As a result, e^-/h^+ pair is generated, which is the key primary step in the photodegradation process. Promoting e^- in the CB becomes the strong point of reduction where it can reduce oxygen (O_2) to superoxide radical anion ($O_2^{\bullet-}$). $O_2^{\bullet-}$ may be further protonated to form the hydroperoxyl radical (HO_2^{\bullet}) having scavenging property and subsequently to hydrogen peroxide (H_2O_2). The hole formed on the VB tends to act as an oxidation site. The hole oxidizes OH^- or H_2O resulting in hydroxyl radicals. Sequentially, the active radicals formed end up in mineralizing organic pollutants to intermediate(s) or final degradation products (CO_2 , H_2O , and stable and less toxic inorganic compounds) as depicted in Equation 1 and Figure 2-1 (Dong *et al.*, 2015).

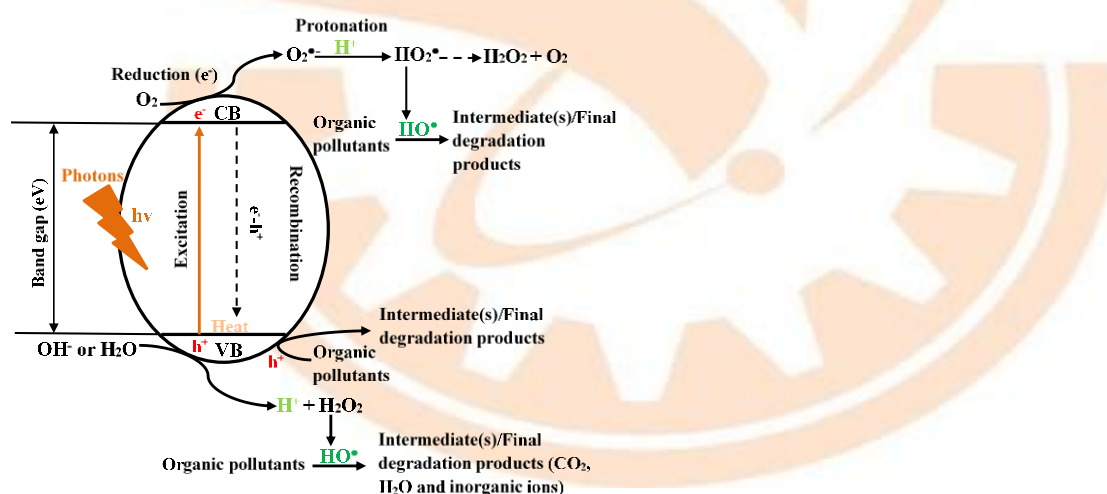
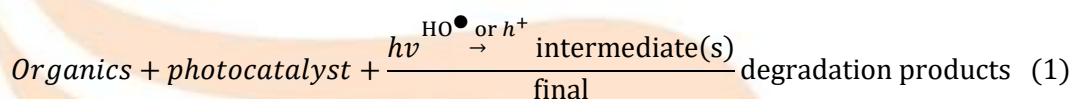


Figure 2-1. Schematic diagram of photodegradation mechanism

However, e^-/h^+ pairs formed are prone to recombine rapidly with the simultaneous dissipation of heat. Therefore, the introduction of the e^- trap (O_2) and h^+ trap onto the VB and CB respectively can minimize e^-/h^+ recombination via the formation of surface trapped e^- and h^+ , which tend to recombine much slower than they do in bulk (Furube *et al.*, 2001). Moreover, the separately formed e^- and h^+ are essential for the active radical formation, which is inherent in pollutant remediation. Hence, prolonging the e^- and h^+ pair using e^- and h^+ trap is vital to enhance the potent photocatalytic process.

2.3.1 Semiconductors as photocatalysts and their bandgap

For effective e^-/h^+ pairs formation on a semiconductor surface, enough energy equal to or greater than its bandgap energy is required. The energy threshold needed for the activation of a semiconductor depends on the energy difference between the VB and the CB (optical band gap energy). From Planck's equation, energy is inversely proportional to the light wavelength. Additionally, the desired power and bandgap energy increase with a decrease in light wavelength. For photoactivation, UV and visible light spectral range have been widely reported (Asiri *et al.*, 2011; Rasheed *et al.*, 2017; Wang *et al.*, 2018). The bandgap energy to light wavelength should be clearly understood for effective e^-/h^+ pairs formation based on a semiconductor selection as a photocatalyst. Apart from optical properties, other intrinsic properties such as physical and chemical stability are also important. Among the photocatalysts, TiO₂ has been widely used in environmental applications due to its high activity, physical-chemical stability, robustness against photo corrosion, low toxicity, and cost (Natarajan *et al.*, 2016). ZnO is also termed as a good semiconductor photocatalyst due to its wide bandgap (3.37), large excitation binding energy that allows laser emission at room temperature, and piezoelectric properties (Yar *et al.*, 2017). Despite TiO₂ and ZnO unique properties favouring photocatalytic activity, their activity is lower due to individual shortcoming recombination and photo-corrosion (Jonidi-Jafari *et al.*, 2015). Above all, TiO₂ is a preferred candidate based on cost and photocatalytic properties. Table 2-2 shows the bandgap of the commonly used semiconductors.

Table 2-2. Photocatalyst with their respective bandgap.

Photocatalyst(s)	Bandgap energy (eV)
TiO ₂ (rutile and anatase)	3.0 and 3.2, respectively (Benton <i>et al.</i> , 2016)
Bismuth oxyhalides (X-Cl, Br, and I)	3.54, 2.97, and 1.93, respectively (Natarajan <i>et al.</i> , 2016)
ZnO	3.37 (wide bandgap) (Yar <i>et al.</i> , 2017)

2.3.2 Fundamental of TiO₂ photocatalysis

Over the past decades, TiO₂-based photocatalyst has received extensive attention in degrading a wide range of organic pollutants. TiO₂ is the most widely investigated heterogeneous photocatalysis due to its high efficiency, low cost, physical and chemical stability, widespread availability, and non-corrosive nature (Herrmann *et al.*, 2007). Heterogeneous photocatalysis involves several sequential processes, namely photoexcitation, diffusion, trapping, recombination, and oxidation. When TiO₂ is irradiated with sufficient light energy that is equal to or greater than its bandgap energy (3.0-3.2eV), the electron is promoted from the valence band (VB) to the conduction band (CB), generating an unfilled valence band (Benton *et al.*, 2016). Due to photoexcitation electron-hole pair is formed. Since there is a continuous transition of electrons between the CB and VB, the recombination process might occur rapidly when the electron falls from the CB to the unfilled hole on the valence band. Thus, dissipating heat energy. The introduction of electron trap and hole trap on the VB and CB usually results in effective electron-hole charge separation, propagating subsequent charge transfer reactions at the specific reductive and oxidative sites (Kohtani *et al.*, 2017). Therefore, the presence of electron scavengers is vital for effective electron-hole charge separation, inducing potent photocatalysis. The hole generated usually reacts with the OH⁻ groups (H₂O) on the TiO₂, forming hydroxyl radicals (HO•). On the other hand, e⁻ reduces O₂ to superoxide radical anions (O₂•⁻). Followed by protonation of O₂•⁻ to hydroxyl radical (HO₂•), further to Hydrogen peroxide (H₂O₂). Therefore, the holes generated and the radicals formed can participate in the degradation of the organic pollutants (Banerjee *et al.*, 2014; Fujishima *et al.*, 2000). The HO₂• having scavenging property can doubly prolong the hole recombination during the entire photocatalytic reaction.

TiO₂ performs effectively upon irradiation with UV light spectral range (<387nm). However, TiO₂ photocatalytic activity is impaired due to some of its physicochemical features. The shortcomings include relatively low adsorption capacity, rapid electron-hole recombination and high aggregation tendency (Dong *et al.*, 2015). The main technical barrier is the recovery of nanosized TiO₂ from treated water. Despite higher photocatalytic activity showed by small compared to large particles, the separation and recoverability allowing reusability of nanosized TiO₂ is an environmental and economic concern.

2.3.2.1 *TiO₂ stability and recombination approach*

During photodegradation, the unstable nanosized TiO₂ tend to aggregate, resulting in the screening of light incidence on the active sites and consequently reducing photocatalytic activity. Moreover, upon photoexcitation, the electron and hole pairs may recombine within a short time dissipating heat energy. To solve these limitations, coupling TiO₂ with another metal has provided a profound approach to retarding electron and hole recombination and improving stability (Wang *et al.*, 2013). Enhanced photocatalytic performance under UV has been observed for p-n heterojunctions formed in TiO₂ coupled with ZnO (Benton *et al.*, 2016). Another significant approach involves doping either with a metal or a non-metal. For metal dopants like Cu, Ag, Au and Zn, they form new bandgaps below CB, whereas, for nonmetal dopants such as N and halogens, they create a new bandgap above the VB. Metal dopants like Ag and Au tend to prolong recombination by forming the Schottky barrier at the metal-TiO₂ interface (Bannet *et al.*, 2009). However, the synergism of doping is greatly affected synthesis methods and conditions. Other drawbacks include thermal instability, short-term photocatalytic efficiency, high temperature for preparation and multiple preparation steps required (Dong *et al.*, 2015). Another promising approach for improving electron-hole separation is dye sensitization however, most sensitizers are toxic and unstable in an aqueous solution. Therefore, the coupling is a better candidate for improving electron-hole separation and reducing aggregation tendency.

2.3.2.2 *TiO₂ adsorption and recovery approach*

TiO₂ low adsorption capacity and separation limitations need to be addressed to improve its photocatalytic activity and extend reusability. Two approaches have been used to address the adsorption and separation problem. The first one involves immobilization of TiO₂ onto support material (e.g., Glass fibres, activated carbon, silica). Another recovery approach consists of a combination of the photocatalyst with a magnetic particle. Among the adsorbent used as support, activated carbon is widely used due to its high adsorption capacity, surface area, very porous, mechanical resistance, eco-friendliness, abundance, low cost, and facile preparation methods (Elisadiki *et al.*, 2019). The activated carbon performance due to good physicochemical properties differs from one study to another, depending on the source of carbon, carbonization, and activation condition. The variation in the preparation condition may directly affect the photocatalytic performance of a catalyst. Recent studies revealed a

synergistic effect of adsorption by activated carbon and photodegradation by pure and hybrid TiO₂ on the degradation of several organic pollutants (Benton *et al.*, 2016; Gao *et al.*, 2011). Coating a catalyst with activated carbon also plays an important role in reducing the cost associated with post-treatment catalyst separation and, consequently, improves reusability (Benton *et al.*, 2017).

i. Source of carbon

Activated carbon is produced from environmental waste having high carbon content mainly agricultural waste (lignocellulosic biomass) and coal sources. Agriculture waste has been widely used as a source of activated carbon due to its availability, renewable, environmentally friendly and requires little preparation process. Sources of activated carbon from the agricultural waste include banana, jackfruits, orange and sapodilla peels (Elisadiki *et al.*, 2019; Yousuf *et al.*, 2019). However, the availability of the sources varies from one to another, therefore, limiting their industrial application. Banana is a widely used fruit in the world due to its nutrition benefits, but huge volumes of peels are disposed into landfills. Parfitt *et al.*, (2010) reported disposal of fruits waste requires a high cost of transportation due to their relatively low bulk density. Further combustion of the fruit waste landfills leads to the emission of methane and carbon dioxide which is unsafe to the environment. The conversion of banana peel waste into useful activated material provides control of the environmental problems especially the emission of greenhouse gases.

ii. Preparation of porous carbon

Two main methods used to prepare AC from agricultural biomass include carbonization followed by activation (physical and chemical). For activation, chemical methods involving the use of strong alkali or acid is superior over physical due to the relatively low temperature required and yielding carbon with more porous and higher specific surface area (Elisadiki *et al.*, 2019).

In addition, the adsorption performance of AC affecting the photocatalytic activity depends on the method of preparation i.e., carbonization and activation. Therefore, the preparation method for AC is a crucial factor that should be considered in its application. The reactions involved in the preparation of AC from a carbon source are well explained and summarized by Elisadiki *et al.* (2019) and Xue *et al.* (2019), using

the equations (3)-(9). In carbonization, carbon source to carbon char is carried out at high temperature 700-1100 °C in an inert atmosphere followed by chemical activation in the presence of a chemical activating agent (such as KOH) at a low temperature (400-700°C). The KOH activation process involves a series of reactions depicted in equations (3)-(9). At a temperature of around 400 °C, KOH is a dehydrated equation (3), followed by sequential water gas reactions equations (5)-(6) and carbonate formation equation (6). Conversely, K₂CO₃ decomposes at a temperature higher than 700 °C, and the K₂O is reduced to K, which therefore intercalates into the carbon lattice structure and consequently widens the pores, equations (8)-(9) (Xue *et al.*, 2019). Finally, the intercalated K onto the carbon pores and inorganic particles is removed by washing with an acid and then water leaving the pores open, which are beneficial for surface area. The general activation reaction can be summarized in equation (3).



2.3.3 Photocatalysis operation parameters

The photocatalytic process of TiO₂ on the degradation of aqueous organic and even inorganic pollutants depends on both the intrinsic and extrinsic parameters. The intrinsic factors and extrinsic parameters are related to TiO₂ operation parameters and physicochemical properties, respectively. The physicochemical properties of TiO₂, such as optical structure and surface properties are critical intrinsic factors that determine the efficacy and performance of TiO₂. The operation parameters include catalyst loading, light wavelength, pH, temperature, dissolved oxygen, etc. Such parameters often affect the overall photocatalytic performance of TiO₂ and ZnO (Gaya and Abdullah, 2008:

Gupta *et al.*, 2020; Zyoud *et al.*, 2020). Moreover, some extrinsic parameters such as oxygen, catalyst, etc. greatly depend on photo-reactor geometry.

i. Catalyst loading

TiO₂ catalyst loading generally affects the overall photocatalytic reaction rate. That is, only at optimum catalyst loading, the maximum degradation of the organic contaminant is achieved. Beyond optimum catalyst loading, this causes a light screening effect due to turbidity and agglomeration. Hence, it decreases the photocatalytic degradation rate. Therefore, determining the optimum catalyst is vital for achieving the maximum degradation rate and avoiding sedimentation and light screening (Zyoud *et al.*, 2020).

ii. pH

In photocatalytic reaction, the pH of the medium based on isoelectric point is an important parameter since it significantly affects the size of either TiO₂ or ZnO particles due to agglomeration h⁺ and •OH and ionization of their surface. Thus, it is critical to determine the isoelectric point, also known as the zero-point charge of TiO₂ and ZnO (uncharged state), to avoid agglomeration and control the formation rate h⁺ and •OH. At pH below the isoelectric point, the surface hydroxylation is favoured, leading to TiO₂ and ZnO nano-sized particles agglomeration, which may hamper the light incidence on the catalyst active sites and consequently decrease the photocatalytic activity (Mallakpour and Nikkhoo, 2014). Moreover, at a pH either lower and equal/higher than zero-point charge, TiO₂ or ZnO often results in ionization, affecting coulombic attraction between the catalyst surface and substrate molecules. Furthermore, the rate of h⁺ and •OH formation is favoured under acidic conditions. The isoelectric point charge for TiO₂, ZnO, and their hybrid is reported to be in pH of 6.4, 7.8, and 7.2, respectively (Zyoud *et al.*, 2020).

iii. Temperature

Photocatalysis involves two key steps, photoexcitation, and adsorption, which are only significantly affected by a large variation of temperature. The increase in temperature up to 80 °C leads to high adsorption of organic pollutants to the surface of TiO₂. Above 80 °C, recombination of the h⁺ and e⁻ is reported to occur, reducing the amount of h⁺ and e⁻ formation and, consequently, the rate of degradation. The optimum operating temperature is reported to range between 20 °C and 80 °C (Chiu *et al.*, 2019).

iv. *Oxygen supply*

Oxygen supply as an electron scavenging agent plays an important role in improving the overall photocatalytic degradation. Oxygen traps e^- and consequently induces the formation of co-scavenger hydroperoxyl and subsequently to hydrogen peroxide, which can be used as a precursor of hydroxyl radicals. Therefore, a sufficient amount of oxygen supply guarantees prolonged recombination and high quantum yield leading to increased photocatalytic degradation (Fujishima *et al.*, 2008).

v. *Initial concentration of the contaminant*

An increase in the contaminant initial concentration can lead to saturation on the photocatalyst's surface. Thus, hindering the photoactivation step and even may lead to the formation of intermediates. Therefore, it reduces the overall photodegradation rate (Gupta *et al.*, 2020).

2.4 Photocatalytic reactors and their configuration

Support material provides a facile way to solve TiO_2 adsorption and separation problems but reduces photocatalytic activity. This is due to the reduction of TiO_2 active surface area to volume ratio and decrease in light utilization by the inactive support material regarding the size increase. Therefore, an efficient photo-reactor design can offer significant advantages over a coupled and supported photocatalyst by providing a superior mass transfer regime, good catalyst surface availability, and good light harvesting.

The adsorption of a sufficient amount of photons to induce the generation of e^- and h^+ pairs is a key primary step in the photocatalytic process. The generation of the e^- and h^+ pair as a primary step is highly dependent on the radiation intensity of the energy source. Therefore, the most important factors in the design and fabrication of any photoreactor are i) the total irradiated surface area of photocatalyst per unit volume and ii) maximum light distribution inside the photo-reactor to minimize inactive photocatalytic site in the reactors iii) maximum mass transfer (Martín-Sómer *et al.*, 2017).

There is profound development of new and optimization of existing photocatalysts. However, the design of an efficient photo-reactor is still the most challenging task in the photocatalytic process (Ray, 1998). For large-scale industrial applications, one main

technical challenge is designing an efficient transparent photo-reactor, allowing light through (Ray, 1998). Thus, most photocatalytic processes are often carried out on a small scale. Designing an efficient photo-reactor is of great significance in photocatalytic processes. Based on an engineering approach, the important factors that should be considered in designing an efficient photo-reactor for wastewater treatment are summarized as follows:

- i. The photo-reactor must be well illuminated to avoid dark zones resulting in an inactive photocatalytic site.
- ii. The favourable photocatalyst location ensures there is the total irradiated surface area of the photocatalyst per unit volume.
- iii. It should have a good channelling flow to minimize the dead volume problem.
- iv. Ensuring there is perfect mixing to enhance catalyst surface availability and improve the pollutant to the activated catalyst surface mass transfer.
- v. To allow the continuous mode of operation to enhance recoverability and reuse of the photocatalyst.

Regarding water treatment processes, photo-reactors are usually categorized based on the location of the photocatalyst. The two main categories of photo-reactors for water treatment include slurry-type photo-reactor and photo-catalyst-immobilized photo-reactor. In a slurry-type photo-reactor, the photocatalyst is suspended, thus providing higher photocatalytic activity. Due to catalyst suspension in the system, a slurry-type reactor can provide high catalyst surface availability and good light harvesting by the catalyst, unlike the photocatalyst-immobilized reactor (Ray, 1998). Thus, the Slurry-type photoreactor is still the preferred photo-reactor configuration. However, the main limitation of slurry-type photo-reactor applications is that it requires post-treatment separation processes. For instance, settling tanks installation or an external filtration system to separate the photocatalyst used from the treated water (Chong *et al.*, 2010). Despite a considerable attempt to overcome the post-treatment separation limitations via membrane installation, the filtration rate and operating costs depend on transmembrane pressure and membrane fouling (Zheng *et al.*, 2017). To overcome this limitation, operating in a fluidized bed reactor (FBR) provides a possibility of catalyst availability towards the source of light and maximum substrate mass transfer.

2.4.1 Fixed bed reactor

A fixed bed also called a packed bed reactor, has a higher conversion per weight of catalyst and with minimal attrition than any other catalytic reactor. Mass transfer and light distribution within the reactor significantly affect the overall photocatalytic degradation in the photocatalytic process. The packed bed photo-reactor greatly suffers from poor light distribution due to light screening by the bed. [Mosleh *et al.* \(2017\)](#) tried to solve this problem by installing a rotating packed bed. Nevertheless, applying a powerful centrifuge to rotate the bed can be expensive due to energy consumption and the maintenance of the moving parts. Therefore, the fluidized bed reactor (FBR) would be the better choice over the fixed bed reactor because of the lack of moving parts. FBR has proven to be an effective reactor in the wastewater treatment processes ([Ochieng *et al.*, 2002](#)). With oxygen gas used as a mixing medium, it can also improve photocatalytic activity. The presence of oxygen prolongs recombination by scavenging e^- and subsequently form a reactive oxygen species, which can participate in the degradation of organic pollutants.

2.4.2 Fluidized bed reactor

Based on economic and environmental concerns, catalyst recoverability and reusability are vital. Some studies have tried to improve the photocatalyst's recoverability and reusability limitations either by supporting it onto porous support material and magnetic unification techniques ([Li *et al.*, 2016](#); [Wang *et al.*, 2016](#); [Wang *et al.*, 2013](#)). However, supporting, and magnetic unification techniques provide a versed solution for particle aggregation, adsorption, and separation problems. It also reduces the active surface area to volume ratios, inhibiting mass transfer and light utilization by the catalyst. Hence, applying a fluidized bed reactor (FBR) can provide a uniform mixing regime of catalyst, uniform light distribution, and contaminants and improve the mass transfer rate ([Gao *et al.*, 2011](#)). Fluidization is a technique by which the solid particles are transformed into a fluid-like state through contact with an upward stream of a fluid (gas or liquid phase). It occurs when solid particles of almost the same size are subjected to an upward flow stream of fluid depending on hydrodynamic parameters ([Brown and Fogler, 2008](#)). This operation is mainly categorized based on the number of phases involved, namely two-phase or three-phase fluidization. The three-phase fluidized system (solid, liquid and gas) can be considered vital in the photodegradation process since it can provide good solid-liquid and gas-solid mass transfer. Operating in a three-phase fluidized bed

reactor system can greatly enhance photocatalytic activity. In the FBR system, more efficient charge separation can be achieved by oxygen in the air (as a fluidizing medium) prolonging recombination favouring the photocatalytic activity. FBR system is indeed less problematic and more effective than other reactors. Moreover, it is very important to note that the fluidization process greatly depends on the reactor geometric and hydrodynamics parameters that can significantly affect the photodegradation rate.

2.4.2.1 Hydrodynamic parameters

Based on a good performance, such as excellent mass and heat transfer, FBR has been greatly used to carry out a variety of multiphase chemical reactions. FBR has displayed significant advantages compared to a packed bed, including better fluid-solid contacts and no hot spot due to the uniform temperature gradient across the bed which allows continuous operation. Good fluidization depends on the following macroscopic observable parameters that affect fluidized bed behaviour, mainly solid concentration distribution and gas holdup. Hydrodynamic parameters are summarized as follows.

i. Aspect ratio

Aspect ratio is a measure of static bed height to the column diameter. At a constant column diameter, the aspect ratio can be altered by changing the bed height. [Ochieng et al. \(2002\)](#) demonstrated that particle loading increases aspect ratio at constant column diameter. Therefore, this could increase bed pressure drop and superficial gas velocities to suspend particles.

ii. Superficial gas velocity

The effect of gas velocity plays a crucial role in the overall performance of fluidized bed systems, mainly solid concentration distribution and gas holdups. This operational parameter is directly affected by the gas velocity flow rate and the column's cross-sectional area. The fluid is supplied to the solids' bed through the distributor at different gas velocities. The bed remains at rest at lower velocities as the fluid passes through voids in the materials behaving like a fixed bed. When the fluid velocity increases, the drag forces begin to counteract the solid particles' weight, resulting in a slight bed expansion. On further increase in fluid velocity at a certain point, the upward drag force becomes equal to the weight of the solids. At this stage, the velocity is known as minimum fluidization velocity, whereby solid particles become suspended within the

fluid. Minimum fluidization (U_{mf}) velocity is a measure of the onset of fluidization. In addition, at a velocity greater than the minimum fluidization velocity, the bulk density of the bed continues to decrease as bed volume increases. As a result, the solid particles are conveyed up with the fluid. At this point, the velocity is referred to as terminal velocity or minimum elutriation velocity. At a velocity beyond terminal velocity is elutriation of the particles is prone to occur. In addition, operating at high velocity can lead to high power consumption by the compressor. Therefore, the air supply for fluidization should be maintained to achieve a proper mixing regime and minimize the power consumption as much as possible. A good fluidization regime occurs between minimum fluidization velocity and terminal velocity.

Global phase holdup is used to describe the characteristic composition of the distinct phase during fluidization. On the assumption of negligible gravitational acceleration and wall friction, pressure drop can be related directly to the phase holdups and the individual density of the phases. The correlation of the phases (solid, liquid, gas) present in the bed can be represented by a global phase holdup Equation (10) since the sum of the phase is equal to one (Haribabu and Sivasubramanian, 2014).

$$\varepsilon_S + \varepsilon_L + \varepsilon_g = 1 \quad (10)$$

Moreover, solid holdup and air holdup can be determined by the macroscopic observable bed expansion using Equation (11)-(12), respectively (Haribabu and Sivasubramanian, 2014).

$$\varepsilon_S = \frac{M_S}{\rho_S A H_{eb}} \quad (11)$$

The gas holdup can be estimated based on the known amount of liquid phase present in the system using Equation (12).

$$\varepsilon_g = \frac{H_{eb} - H}{H_{eb}} \quad (12)$$

On assumed negligible acceleration and wall friction, pressure drop can be determined using phase holdups based on the bed height change Equation (13).

$$\frac{\Delta P}{\Delta H} = (\rho_s \varepsilon_s + \rho_L \varepsilon_L + \rho_g \varepsilon_g)g \quad (13)$$

Equation (13) implies that the density of the solid is directly proportional to the pressure drop across. High and low densities consequently can increase power consumption and particle elutriation, respectively.

Oxygen plays an important role in prolonging recombination e^-/h^+ pairs by trapping e^- . Therefore, using gas as a fluidizing medium can provide a positive oxygen mass transfer effect, unlike a liquid medium (Nikolov *et al.*, 2000). The correlation between gas fluidization velocity and gas hold up is given by equation (14).

$$\varepsilon_g = AU_g^n \quad (14)$$

Mass transfer is an important chemical engineering aspect that can explain the mechanism and concentrations between different phases in a reaction. Moreover, Bouaifi *et al.* (2001) reported a simple linear correlation between gas hold up and mass transfer coefficient (K_{La}), as shown in Equation (15). Therefore, gas hold-up correlation mass transfer can be used to explain the catalyst homogeneous mixing and oxygen mass transfer, which directly affects the photodegradation reaction.

$$K_{La} = 1.53\varepsilon g \quad (15)$$

From equation (15)-(16), the correlation between gas velocity and mass transfer is given as.

$$K_{La} = BU_g^n \quad (16)$$

where $B=1.53A$.

2.5 Knowledge gaps

From the literature review, textile wastewater is characterized by a high Chemical Oxygen Demand (COD), Biochemical Oxygen Demand (BOD) and intense colour in water bodies thus causing water pollution and consequently public health concerns (Santhana *et al.*, 2021). Many techniques have been applied to remediate the textile wastewater, decolourise and degrade dyes including conventional physical, chemical and biological methods (Foo and Hameed, 2010). However, these traditional methods

are unable to completely degrade organic dyes and might cause secondary pollution. It is clear that heterogenous photocatalysis is a simple, low-cost AOP, and offers a green way to degrade a wide range of bio-recalcitrant organic pollutants (Miklos *et al.*, 2018). TiO₂ as a photocatalyst is widely used owing to its high efficiency, nontoxicity, stability, and ease of preparation (Herrmann *et al.*, 2007). Nevertheless, TiO₂ has relatively low adsorption capacity, rapid electron-hole recombination and high aggregation tendency (Dong *et al.*, 2015). Despite promising efforts to overcome these limitations, one of the main practical drawback of using TiO₂, is the difficulty of separating it from the wastewater after use, which is an economic and environmental concerns. Supporting a photocatalyst plays an important role in improving adsorption capacity, reducing the cost associated with post-treatment catalyst separation and, consequently, improving reusability (Benton *et al.*, 2017). Therefore, the major focus of this study is to prepare low-cost and efficient ternary photocatalyst made up of TiO₂-ZnO supported on activated carbon derived from banana peel waste. Although the support material offers a solution for low adsorption capacity and separation problems, instead it reduces photocatalyst surface area to volume ratio (Dong *et al.*, 2015). Thus, this study designs an efficient photoreactor and further evaluates hydrodynamic conditions to understand the homogeneity of the system and consequently overcome the mass transfer limitation posed by the supported photocatalyst.

CHAPTER 3

3 MATERIALS AND METHODS

The overall TiO₂-based photocatalysis reaction involves a series of independent key steps. The sequential steps involved include mass-transfer of the organic substrate in the liquid phase to the TiO₂ surface, simultaneous photoexcitation of TiO₂ and adsorption of the organic substrates onto photoactivated TiO₂ surface and then followed by photodegradation of the adsorbed substrate. Finally, the desorption of intermediates formed and mass-transfer of the intermediates from the interface region to the bulk aqueous solution. Based on previously discussed TiO₂ drawbacks, a series of experiments were carried out to improve its overall photocatalytic activity. In this thesis, simulated wastewater of the textile dyes was used as organic pollutants. Adsorption and photodegradation (as the main process) were conducted under dark and UV-light conditions, respectively. Various analytical measurements such as Ultraviolet-visible spectra (UV-Vis), pH, and chemical oxygen demand (COD) analysis were conducted. The materials used in the experiment were prepared, characterized before and after being tested. Numerous experiments were carried out to have the best variables control level on the physicochemical properties of the prepared materials, photocatalytic operation parameters and hydrodynamic conditions.

Based on physicochemical properties control, a mixture experimental design was used to obtain the optimum percentage composition of ZnO and support material on pure TiO₂. Before the introduction of support material, adsorption optimization experiments were done on the activated carbon from banana peels (BAC) using different potassium hydroxide (KOH) impregnation ratios. Thereafter, the resultant BAC with the highest decolourization rate on dye was then used as support material. The one-factor-at-a-time (OFAT) experimental design was used to evaluate the photocatalytic operation parameters, hydrodynamic parameters and other variables that affect the adsorption and subsequently photocatalytic process. The efficiency of the process-based energy requirement was also evaluated. The experimental setups used in this work was lab-scale stirred tank reactors (STR) and fabricated fluidized bed reactors (FBR). FBR as the main photoreactor chamber was used to study hydrodynamics to further delve into the homogeneity of the phases in the system. The hydrodynamic study involved the evaluation of gas holdup and solid concentration distribution in the system.

Furthermore, experiments were conducted to evaluate the effect of hydrodynamics on photodegradation.

3.1 Materials

Titanium (IV) isopropoxide (97%) and Zinc acetate ($\geq 97\%$) used as a precursor in the preparation of Titanium (IV) oxide (TiO_2) and Zinc Oxide (ZnO), respectively, were purchased from Sigma Aldrich Co. Ltd., South Africa (SA). Methanol (99.5%) purchased from Associated chemical enterprises (ACE) Co. Ltd., SA was used as a solvent in the preparation of TiO_2 . Potassium hydroxide (KOH) purchased from Minema chemicals Co. Ltd., SA was used as an activating agent in the preparation of activated carbon from banana peel. Ammonium oxalate (AO), 98% P-benzoquinone (BQ), Isopropanol (IPOH) purchased from Sigma Aldrich Co. Ltd., SA was used as scavengers to quench active species formed during photodegradation. Sodium hydroxide (NaOH) (98-100%) and Hydrochloric acid (32% CP HCl) purchased from Minema Chemicals Co. Ltd., SA was used in adjusting pH. Sodium Nitrate (NaNO_3) purchased from Minema Chemicals was used to prepare an aqueous solution used to determine the point of zero charges (PZC) of the material. Rhodamine 6G (R6G), methylene blue (MB) and malachite green (MG) dye were used to prepare stock solutions of synthetic dye wastewater and was purchased from Sigma Aldrich Co. Ltd., SA. The banana peel waste used to prepare activated carbon (BAC) as photocatalyst support material was collected from Extension 7 Palapye, Botswana. Low range (L: 0-150 mg/L) and medium range (M: 1500 mg/L) Chemical Oxygen demand (COD) vials purchased from Sigma Aldrich Co. Ltd., South Africa (SA) were used as dichromate reagents for COD measurements. All the reagents were analytical grade therefore, they were used as acquired. The deionized water was used for solution preparation.

3.2 Analytical equipment

X-ray diffractometer (XRD) (Bruker D8 Model) with $\text{Cu-K}\alpha$ radiation set at a wavelength of 1.54056 \AA was used to identify the composition of purity and crystallinity of the prepared material. Fourier transform infrared (FTIR) (Bruker, Germany Model) Bruker Vertex 80v vacuum was used to identify the functional groups present on the surface of the prepared material. Gemini SEM 500 Scanning electron microscopy (Carl Zeiss, Japan Model) was used to characterize the surface morphology of the prepared material. UV-vis spectroscopy was used to determine the bandgap energy of the prepared semiconductor material by the solid-state electronic absorption

spectra technique. Photoluminescence spectroscopy (PL) (Jasco spectrofluorometer FP-8600 Model) at Vaal University of Technology (VUT) was to study electron-hole pair recombination of the prepared semiconductor material. The surface area of the materials was analysed using Brunauer-Emmett-Teller (BET) method using the Micro-metrics Tristar porosity analyser at the University of Johannesburg (UJ). TGA/DSC 3⁺ Thermogravimetric analyser (Mettler Toledo Model) use used to study the thermal stability of the prepared material. Malvern (Mastersizer 3000 E) coupled to a wet dispersion unit (Malvern Hydro EV Model) was used to analyse the particle size.

The pH meter (6 PC 2700 Benchtop, Oakton Model) was used to measure the solution pH. UV-vis spectroscopy (UV-Vis Thermo Scientific 201 Model) equipped with PC having Thermo software was used to monitor dye colour removal during adsorption and photodegradation process. The centrifuged dye samples absorbance related to concentration was based on the maximum absorption wavelength at around 525 nm for R6G, 664 nm for MB, and 618 nm for MG dye (Appendix B) using water as a reference. A Lovibond COD kit (MD 200 COD VARIO model) composed of digester RD 125 and spectrophotometer was used to measure COD level. Briefly, a 2mL aliquot of the sample collected was mixed with COD low range vials (0-150 mg/L) before being digested at 148 °C for 2 h. The same procedure was done for blank (water) and the samples before being subjected to photodegradation. After cooling, the vial containing the mixture was transferred to a spectrophotometer for COD reading.

3.3 Experimental reactors

In this study, a lab-scale stirred beaker reactor (STR) and fabricated fluidized bed reactor (FBR) system were used to carry out the adsorption and photodegradation process. The STR was used to determine superior photocatalyst and photocatalytic operation parameters. The FBR as the main photocatalytic system was used in studying hydrodynamic conditions affecting the photocatalytic process.

3.3.1 Lab-scale stirred tank reactor

An experimental lab-scale stirred beaker reactor (STR) (Figure 3-1a and b) was used to test the performance of the prepared materials, and operation parameters affecting the adsorption and photocatalytic activity. The STR rig consisted of a 250 mL borosilicate glass beaker, magnetic stirrer (Bio cote Model) covered with aluminium foil, stirring rod (Size: 8×30 mm) and UV lamp as a source of ultraviolet (UV) irradiation. Aluminium foil placed between the beaker and magnetic stirrer was used to avoid the

dark zone at the bottom of the beaker. The UV lamp used was UVP UVG-54 6 Watt/254nm/0.16 Amps/230V~50-60Hz (size: 151 × 44 mm) with a typical light intensity of 254 nm energy at 0.0762 m (22 W/m²). Figure 3-1 b, consisting of a temperature controller connected to a sensor, dipped in an oil bath was used to study the effect of temperature on degradation. The oil bath was used to ensure uniform heat distribution to the beaker while the cork wood flask base was used to prevent direct heat contact between the beaker and the hotplate.

3.3.2 *Fabricated Fluidized bed reactor*

The fabricated fluidized bed reactor (FBR) rig consisted of a pyrex glass column with two inlets and two outlets, fitted with a distributor plate made of sintered glass (10-16 μm) at the bottom, which was used as the main chamber for the photocatalytic reaction. The FBR column had an inner diameter: 29.7 mm, height: 575 mm and a Total volume: 0.40 L. The belt-driven air compressor (3 HP, 360 L/min, 115 Psi) was connected at the bottom of the glass column via an air rotameter to provide air for fluidization throughout the experiment. Two UV lamps (254 nm, 14 W) mounted on semi-cylindrical support with aluminium lining placed opposite to each other, 1 cm from the surface of the column was used as a source of UV irradiation during the photodegradation process. The aluminium lining was used to maximise and concentrate UV reflection on the glass main photocatalytic chamber. FBR was used to study hydrodynamics and evaluate the effect of hydrodynamics on the adsorption and photodegradation process.

3.4 Experimental Design

In this study, the mixture design of the experiment from Minitab software was used to obtain the best proportion of each pure component in the hybrid and support loading regarding physicochemical properties control. The OFAT design of the experiment was used to evaluate the extrinsic operation parameter and other variables as displayed in Table 3-1 and 3-2.

Table 3-1. *OFAT design of experiment of varied parameters.*

Experiment	Parameter and variables	Values or reagents
Individual dye (R6G)	ZnO composition on TiO ₂	15-70%

	BAC1 loading	0-70%
	pH	2-11
	Catalyst loading	0.2-1.4 g/L
	Initial concentration	40-70 mg/L
	Temperature	30-80 °C
	Scavenger for active species	Ammonium oxalate (h ⁺) Benzoquinone (O ₂ • ⁻) Isopropanol (HO•)
Different dyes	R6G, MG, and MB	50 mg/L

Table 3-2. OFAT design of experiment on hydrodynamic parameters.

Hydrodynamic parameter (Experiments)	Parameter varied
Gas holdup (Gas-liquid mass transfer)	Superficial air velocities (0.009 - 0.033 ms ⁻¹)
	Aspect ratio (2-12)
	Reactor inclination angle (90 ° – 50 °)
Solid concentration distribution	Superficial air velocities

(Substrate-catalyst mass transfer)

Solid loading

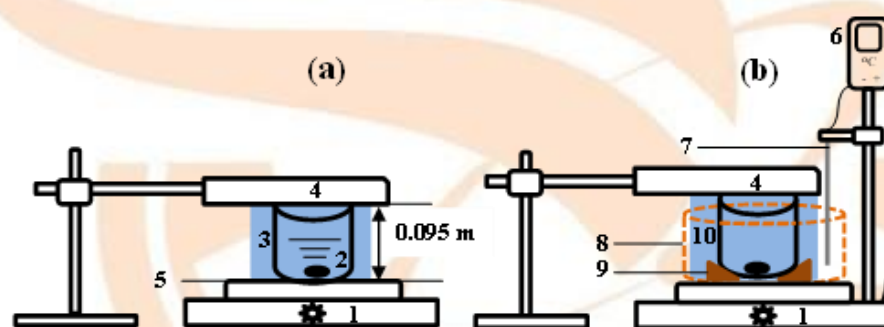
Inclination angle

(90 ° – 50 °)

90 ° as vertical position

3.5 Experimental setup

In this work, a lab-scale STR (Figure 3-1 a-b) and fabricated FBR experimental setup were used to conduct the adsorption and photodegradation experiments. In lab-scale STR, the distance from the pollutant aqueous solution to the lamp surface was 0.095 m.



1-Hotplate, 2-Magnetic stirrer, 3-Glass beaker, 4-UV lamp, 5-Aluminium foil cover, 6-Temperature controller, 7-Temperature sensor, 8-Aluminium pot, 9-Cork wood flask base, 10-Oil bath.

Figure 3-1. (a) and (b) Schematic diagram of a lab-scale stirred tank experimental setup.

The main photo reactor setup, FBR (Fig 3-2), consist of a cylindrical glass column (6) screwed onto a plastic connector (4). The plastic connector fitted to the non-return valves (2) was used to hold the sintered glass diffuser and to prevent the backward flow of water from the reactor in case of leakage at the gas diffuser. Air (constant pressure 1.5 bar and temperature 25 °C) was supplied to the reactor from the lab air compressor (1) through the air rotameter (3), where the flow rate was regulated. The gas diffuser had a fine pore size smaller than the catalyst size that only allowed gas to pass through and produce small uniform bubbles for good fluidization.

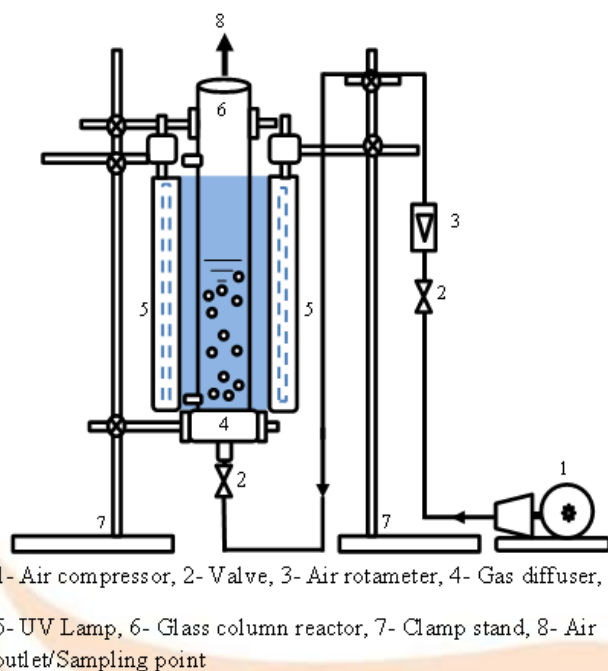


Figure 3-2. Schematic diagram of fluidized bed reactor.

The main section (6) of the reactor was made of borosilicate glass since it allows high transmittance of UV range of about 80%, thus not problematic for UV transmission applications as demonstrated by Peng *et al.* (2020). The glass column outer and inner diameters were selected to be 34.0 and 29.7 mm, respectively, which falls in the range of 25.0-50.0 mm for an ideal photoreactor as suggested by Rodríguez *et al.* (2004). For UV irradiation, the two UV lamps mounted inside the semi-cylindrical plastic support with aluminium foil lining (5) were kept vertically opposite each other, both facing the reactor. The two lamps were placed 1 cm from the surface of the glass column to ensure maximum UV irradiation and avoid or minimize heat from the lamps in case of overheating.

3.6 Experimental procedure

3.6.1 Catalyst and support material preparation

The preparation of TiO₂-ZnO/BAC supported photocatalyst first involved a separate synthesis of TiO₂, ZnO, and banana peel activated carbon (BAC) as support material. This was followed by the preparation of the TiO₂-ZnO hybrid and, finally, the introduction of support material onto the hybrid to form a composite (TiO₂-ZnO/BAC1).

3.6.1.1 Preparation of TiO₂ through reflux method

TiO₂ was successfully synthesized by the reflux method (Behnajady *et al.*, 2011). Briefly, a precursor solution containing 83.33 mL titanium (IV) isopropoxide and 11.40 mL methanol was uniformly sonicated in an ultrasonic bath at room temperature. This was followed by the gradual addition of 329.4 mL deionized water (18 mL per 10 min) to initiate hydrolysis under refluxing and magnetic stirring for 3 h at 80°C. The resultant molar ratio of titanium isopropoxide: methanol: water was 1:65:1. After 3 h of continuous refluxing and magnetic stirring, the white sol was obtained through centrifuging, re-dispersed in methanol with repeated centrifuging to decant the supernatant solvent. The resultant precipitate was later dried at 80°C for 12 h, followed by calcination at 500°C for 3 h to obtain dried TiO₂ particles. Finally, the TiO₂ particles were crushed using a mortar and a pestle then stored for further use.

3.6.1.2 ZnO synthesis via precipitation method

ZnO was prepared via the precipitation method, adopting a technique reported by Daou *et al.* (2017). A given mass of Zinc acetate was dissolved in 150 mL of distilled water under constant stirring at 50-60°C and at the same time followed by the gradual addition of 40 mL of 1M NaOH to form a white precipitate. After that, the solution was continuously stirred for 1 h at 50-60°C to obtain a uniform white precipitate. The obtained uniform precipitate was filtered, washed four times using distilled water, and dried overnight in an oven at 100°C. Finally, the white product obtained was then ground and calcined at 500°C for 3 h in a muffle furnace to obtain a dried ZnO powder.

3.6.1.3 Preparation of activated carbon from banana peels

Two main steps, carbonization, and activation were used to prepare activated carbon from banana peel waste. At first, banana peels were thoroughly washed with deionized water, sun-dried for 2 days, and dried in an oven at 100 °C for 24 h. The dried banana peels were then crushed into powder form, then sieved using mesh sieve (200 – 280 μm). The sieved banana peels were carbonized using an electric resistance tube furnace at 400 °C for 1h (heating rate: 10°C per min) under an atmosphere of nitrogen (flow rate: 20.0 std. cubic centimetres per minute). The yield char from banana peels was 39.1%. From the available literature, activated carbon derived from carbon source with high surface area is produced starting with chemical KOH activation ratio of 1 over the mass of pre-carbonized char (Elisadiki *et al.*, 2019). Therefore, in this study, the mass

ratio of Char: KOH during chemical activation was varied from the mass ratios of 1:1, 1:2, and 1:3. For activation, the black carbonized banana peel (Char) was first mechanically mixed with a required mass of KOH. The impregnation ratio (Char: KOH) of the samples were 1:1, 1:2, and 1:3 (w/w), referred to as BAC1, BAC2, and BAC3, respectively, whereas non-activated carbon was referred to as BAC0. The impregnated samples were separately activated using a tube furnace at 700°C for 1 h (heating rate: 10 °C per min) under a nitrogen atmosphere. After cooling to room temperature, the resulting activated samples were soaked in 1M HCl to remove any residual ash before being washed with deionized water several times until the washing pH of water reached almost neutral (pH 6.5-7.5). Finally, the three wet activated carbon samples (BAC1, BAC2 and BAC3) were dried in an oven at 100°C for 24 h. The dried activated carbon samples were left to cool to room temperature before being stored in a separate sealed tube for further use.

3.6.1.4 Preparation TiO_2 -ZnO hybrid

A composite of TiO_2 -ZnO was prepared using different mass ratios of TiO_2 , and ZnO. Different mass ratios of TiO_2 and ZnO summing to 100% was weighed and then mechanically mixed using pestle and mortar with a few drops of deionized water as a solvent to form a paste-like mixture. Then the products (TiO_2 -ZnO) with varying mass ratios were dried at 70°C for 1 h and then calcined at 450°C for 5 h. After that, the products were ground into powder before being used. The composition of the hybrid prepared is summarized in Table 3-3.

Table 3-3. Hybrid percentage composition of TiO_2 and ZnO.

TiO_2-ZnO hybrid composition (100%)						
TiO_2 (%)	95	85	80	75	50	25
ZnO (%)	5	15	20	25	50	75

3.6.1.5 Immobilization of superior TiO_2 -ZnO onto activated carbon.

The superior hybrid (TiO_2 -ZnO) in terms of photocatalytic efficiency on the dye was immobilized onto varied percentage compositions of support material (10-70%). The

support material used was the banana peel activated carbon (BAC), with the highest decolourization rate due to adsorption.

For BAC photocatalyst composite, TiO₂-ZnO hybrid supported onto activated carbon was prepared through a simple method reported by Benton *et al.* (2016). A varied mass ratio TiO₂-ZnO and BAC were ground together and then well mixed in a 30% colloidal silica solvent under ultrasonication at room temperature for 30 min to achieve uniform dispersion. The mass ratio of BAC loading onto the photocatalyst samples was varied from 10% to 70% shown in Table 3-4. The resultant mixture containing TiO₂-ZnO, and BAC were separately dried in an oven at 100°C for 6 h to obtain dried granules. The dried granules were crushed and sieved using 300-400 μm sieve size before being used.

Table 3-4. BAC percentage composition on 85% TiO₂-ZnO superior hybrid.

TiO₂-ZnO/BAC composite composition (100%)							
TiO₂-ZnO (%)	90	80	70	60	50	40	30
BAC (%)	10	20	30	40	50	60	70

3.6.2 Preparation and characterization of simulated wastewater

Simulated wastewater stock solution (100 ppm) for the individual dye was prepared by dissolving 0.1 g of commercial dye powder in 1 L of distilled water. The commercial dye used in this study were Rhodamine 6G (R6G), methylene blue (MB) or malachite green (MG). The required initial concentration of the dye was obtained from the corresponding stock solution based on molarity stoichiometry calculation. The 50 ppm of individual simulated wastewater R6G, MB, and MG dye from the stock solution were characterized, as displayed in Table 3-5.

Table 3-5. Estimated water quality characteristics of simulated wastewater.

Dye C₀ = 50 ppm	MB	MG	R6G
Chemical oxygen demand (COD), mg/L	131	124.7	137.4

pH	6.3	7	7
----	-----	---	---

3.6.3 Catalyst and support material characterization

X-Ray Diffractometer was used to determine the diffraction pattern of the prepared materials. The instrument was operated according to a Bragg-Brentano geometry scanning within the values of 2θ between 10° and 80° with a step size of 0.45sec/step . The XRD data were analysed using Diffraction EVA and MATCH3 software to identify the major phases present in the materials.

Fourier transform infrared with accessories was used to determine the functional groups present in the materials. The IR spectra were scanned over a wavenumber range of $500 - 4000\text{ cm}^{-1}$. The thermogravimetric analyser instrument was used to determine the thermal decomposition behaviour of the prepared materials. The thermal decomposition study at a temperature range of $30 - 900^\circ\text{C}$ was investigated at a fixed ramp rate of 10°C/min under a flow rate of 20 mL/min nitrogen.

Scanning electron microscopy (SEM) was used to study the surface morphology of the material. An automated gas sorption porosimeter instrument was used to measure the adsorption and desorption of liquid nitrogen at constant temperature (77 K). Before nitrogen adsorption measurements, the materials were degassed at 393.15 K for 3 h . The specific surface areas of materials were calculated using Brunauer-Emmett-Teller (BET) method.

The optical properties of the photocatalysts were characterized by solid-state electronic absorption spectra. The method involved 1 min ultrasonication of 0.05g from each powder system in water solvent (40 mL). The spectra were measured against the baselines of methanol and noted the maximum adsorption wavelength. The maximum adsorption wavelength for each sample was divided by 1240 to estimate the bandgap energies. The photoluminescence (PL) spectroscopy operated within the wavelength range of $300\text{-}800\text{ nm}$ emission and 450 nm excitation was used to determine electron-hole recombination of the photocatalysts.

The point of zero charges (PZC) of the optimized photocatalyst was measured using the pH drift method (Pashai *et al.*, 2016). The method involved adding 0.1 g of solid into 40 mL of 0.1 M NaNO_3 aqueous solution into various vessels that were adjusted

to initial pH₀ values (3-11) by 0.1 mol/L HCL or NaOH. Each vessel with the suspension was subjected to a shaker at 25 °C, and 150 rpm for 24 h. After agitation, the final pH₁ was recorded and a graph of pH₀ and pH₁ was plotted. The diagonal straight-line intersecting between the pH₀-pH₁ curve was used to obtain the PZC.

The particle size distribution of the photocatalyst was analysed using wet dispersion in Melvern 3000 analyser run in the Fraunhofer diffraction model. The distilled water was used as a dispersant solution with a refractive index of 1.330. Given the amount of sample (~ 0.4 g) was dispersed in 500 mL water until the laser obscuration bar indicated ~ 10% for analysis and the result was recorded within 8 min.

3.6.4 Photodegradation in lab-scale stirred tank reactor

3.6.4.1 Effect of KOH activation ratio on the AC adsorption activity

The optimization of adsorption activity of activated carbons from banana peels using different KOH impregnation ratios for activation was studied. The activated carbon prepared by char: KOH mass ratio 1:1, 1:2 and 1:3 was referred to as BAC1, BAC2 and BAC3, respectively while the non-activated carbon was referred to as BAC0. The adsorption efficiency of the prepared BAC0, BAC1, BAC2 and BAC3 materials were tested on decolourization of R6G dye. Four sets of 80 mL (30 ppm) R6G dye solution, each having 0.3 g/L adsorbent dosage of BAC0, BAC1, BAC2 and BAC3 were prepared. The initial pH of the mixtures was adjusted to approximately 7. The mixtures were subjected to a constant stirring of 250 rpm until the equilibrium was attained. During the adsorption process, samples were collected at a predetermined time interval of 10 min, centrifuged at 7000 rpm for 3 min and then analysed using a UV-Vis spectrophotometer. The samples were centrifuged to obtain the supernatant liquid for accurate analysis by avoiding catalyst light attenuation from the sample. R6G dye samples were analysed based on their maximum absorbance ($\lambda = 525$ nm), related to the concentration using the constructed calibration curve (Appendix D). The adsorption capacity (q_e) and colour removal percentage efficiency, Ad (%) were calculated using equation (17)-(18):

$$q_e = \frac{(C_0 - C_e)V}{m} \quad (17)$$

$$Ad = \frac{(C_0 - C_t)}{C_0} \times 100\% \quad (18)$$

where C_0 and C_t are the initial concentration of the dye (mg/L) at time = 0 and the dye concentration at a given time during the adsorption (time = t), respectively. C_e is the equilibrium concentration of the dye (mg/L), V is the volume of the dye aqueous solution (L) and m is the mass of the adsorbent (g).

3.6.4.2 Photocatalytic efficiency of TiO_2 -ZnO with different mass ratios.

The effect of the TiO_2 : ZnO mass ratio on the resultant hybrid (TiO_2 - ZnO) was investigated. The experiment was conducted using the resultant TiO_2 - ZnO hybrid having a different TiO_2 : ZnO mass ratio. 0.08g for each TiO_2 - ZnO hybrid was dispersed in 80 mL of 50 ppm R6G dye solutions at pH ~ 7. The mixtures were magnetically stirred (250 rpm) in the dark until there was no change in concentration (adsorption-desorption point). When adsorption-desorption equilibrium was achieved, the mixtures were subjected to UV irradiation (254 nm, 22 W/m²) under continuous constant stirring of 250 rpm. During the adsorption and photodegradation process, samples were collected at predetermined time intervals, centrifuged and the supernatants were analysed for the residual R6G dye. The superior hybrid composition was further supported on BAC1 support. The colour removal due to photodegradation (% Pd) and overall photocatalytic degradation (% Overall Pd) was calculated using equation (19)-(20):

$$Pd (\%) = \frac{(C_e - C_t)}{C_e} \times 100 \quad (19)$$

$$Overall Pd (\%) = \frac{(C_0 - C_t)}{C_0} \times 100 \quad (20)$$

where C_t is the dye concentration at a given time during the UV irradiation after adsorption-desorption equilibrium (C_e) is achieved.

3.6.4.3 Effect of optimized BAC1 composition superior TiO_2 -ZnO hybrid activity

The superior TiO_2 -ZnO hybrid loaded on optimized BAC with different percentage compositions in the range of 70%- 10% making a composite was investigated. The 80 mL sets of solution (each having 30 ppm R6G, 0.7 g/L composite loading) at pH ~ 7 were stirred (250 rpm) in the dark to achieve adsorption equilibrium. Thereafter, the solutions were subjected to UV irradiation to initiate the photodegradation process.

Sampling was carried out at predetermined time intervals. The samples collected were centrifuged before being analysed for colour removal to monitor the adsorption and photodegradation process. The superior composite, 85% TiO₂-ZnO immobilized onto 40% BAC1 was used in the subsequent experiments.

3.6.4.4 Photodegradation activity of pure, hybrid and composite catalyst

The photodegradation experiments were carried out using pure ZnO, TiO₂, superior 85%TiO₂-ZnO hybrid and optimized 85%TiO₂-ZnO/BAC1 (with 40% BAC1) composite materials. The optimized 85%TiO₂-ZnO/BAC1 was determined from results obtained by varying the percentage composition of superior TiO₂- ZnO and BAC1 support (Table 3-4). 80 mL of 50 ppm R6G dye was mixed with 0.104 g for each of the catalyst materials at pH ~ 7. Before UV irradiation, the suspensions were magnetically stirred (250 rpm) in the dark for 60 min to establish the adsorption equilibrium of the dye. At predetermined time intervals, samples were withdrawn, centrifuged, and then analysed to monitor the colour removal. The same experimental procedure was used to investigate R6G aqueous solution COD removal over-optimized 85%TiO₂-ZnO/BAC1 composite. For energy requirement studies, the efficiency based on the energy required for the colour removal and COD reduction over UV photo catalysed process using 85%TiO₂-ZnO/BAC1 composite was calculated using electrical energy per order (E₀) equation (21) (Jonidi-Jafari *et al.*, 2015):

$$E_0 = \frac{P \times t \times 1000}{V \times \log \left(\frac{C_0}{C_f} \right)} \quad (21)$$

where P is the lamp power (kW), t is the irradiation time (h). V is the volume of wastewater degraded (L). C_f represents the final concentration of the solution (at the end UV irradiation).

3.6.4.5 Main active species responsible for R6G photodegradation

A series of experiments were carried out to identify the main active species generated over-optimized 85%TiO₂-ZnO/BAC1 composite on degrading R6G dye. Four sets of suspension (80 mL, 50 ppm R6G dye) each having 0.104 g/L 85%TiO₂-ZnO/BAC1 composite loading was prepared. The initial pH of the suspension was adjusted to pH ~ 7. The suspensions were stirred for 60 min to establish adsorption-desorption

equilibrium. Before UV irradiation, 1 drop of 1.0 mmol^{-1} of ammonium oxalate (AO, quencher of h^+), benzoquinone (BQ, quencher of $\text{O}_2^{\bullet-}$), and isopropanol (IPOH, quencher of HO^{\bullet}) scavenger was added in the three separate suspensions except for one which was referred as no scavenger. The scavenger was added to trap active species responsible for photocatalytic degradation. Thereafter, the four suspensions were exposed to UV irradiation under constant stirring (250 rpm) to initiate the photodegradation process. Samples collected were analysed using a UV-Vis spectrophotometer.

3.6.4.6 Photodegradation of the dyes using 85%TiO₂-ZnO/BAC1

For the photodegradation of different dyes experiment, 80 mL of 50 ppm of different dyes (R6G, MB and MG) were mixed with 0.104 g/L 85%TiO₂-ZnO/BAC1 composite at pH ~ 7 . The mixtures were magnetically stirred in the dark to achieve adsorption-desorption equilibrium before being exposed to 160 min UV irradiation. The samples withdrawn were centrifuged before being analysed by a UV-Vis spectrophotometer. The concentration of R6G, MB and MG were measured by recording their absorbance at 525 nm, 664 nm, and 618 nm, respectively with the spectrophotometer. COD of the samples were also analysed.

3.6.4.7 TiO₂-ZnO/BAC1 stability and reusability study

The stability measurements of the TiO₂-ZnO/BAC composite was conducted for 4 consecutive days (one day per cycle). Initially, 0.104 g of TiO₂-ZnO/BAC composite and 80 mL of 50 ppm R6G dye solution at pH ~ 7 was placed in SBR. The mixture was magnetically stirred (250 rpm) for about 1 h to reach the adsorption-desorption equilibrium before being subjected to 2 h of UV irradiation. Samples were withdrawn every 30 min, centrifuged to separate the photocatalyst. The supernatant solution was analysed using a UV-Vis spectrophotometer while the obtained photocatalyst was washed 5 times with distilled water then dried overnight at 80 °C. The recycled photocatalyst was used in the second cycle maintaining the same operation condition (80 mL, 30 ppm at pH ~ 7). The third and fourth cycles were conducted using the same procedure.

3.6.4.8 Photodegradation operation parameters

The effect of pH on adsorption and photodegradation experiments was conducted using TiO₂-ZnO/BAC1 photocatalyst composite. R6G aqueous solution (80 ml, 50 ppm) was

mixed with 0.104 g of TiO₂-ZnO/BAC at different pH values (2, 4, 8, 7,10 and 11). pH adjustment was done using 0.2 M NaOH and 0.2 M HCl. The suspensions were magnetically stirred (250 rpm) in the dark while monitoring the adsorption process. When adsorption-desorption equilibrium was achieved, the suspensions were exposed to UV irradiation under continuous constant stirring to initiate the photodegradation process. The samples withdrawn were then centrifuged and the supernatants were analysed using a UV-Vis spectrophotometer.

The effect of catalyst loading on degradation was studied using the same procedure and experimental conditions but varying the solid loading (0.4-1.4 g/L) and keeping the pH 7 of the R6G solution constant. Initial concentration was also studied using similar procedure and conditions but varying the initial concentration (40-70 ppm) and catalyst loading of 1.3 g/L kept constant. The effect of temperature was done in a temperature-controlled setup (Figure 3-1 b) under set temperature (varied range 30-80°C), 70 ppm R6G, pH 7, and catalyst loading 1.3 g/L.

3.6.5 Hydrodynamics and photodegradation in fluidized bed reactor

3.6.5.1 Hydrodynamic studies

Preliminary experiments were first carried out in FBR to evaluate hydrodynamic behaviour, mainly solid concentration distribution and gas hold-ups. Therefore, parameters such as superficial velocity and aspect ratio, which affect hydrodynamic conditions, were determined. In this experiment, distilled water, optimized 85%TiO₂-ZnO/BAC1 photocatalyst composite, and purged compressed air were used as liquid, solid, and gas-phase respectively, whereby solid concentration distribution and gas hold up were determined using the methods adopted from [Matsumura *et al.* \(2007\)](#) and [Haribabu and Sivasubramanian, \(2014\)](#). The optimized 85%TiO₂-ZnO/BAC1 photocatalyst (Dx50% 320 μm depicted in Appendix D) was used. The photocatalyst density (ρ) was 3941 kgm⁻³, and it was further assumed that the photocatalyst was spherical (Figure 4-4). The system was operated in batch mode.

For the global gas hold-up experiments, the reactor column was placed in the desired inclination position (90°–50°) and then a known volume of water and determined solid loading (85%TiO₂-ZnO/BAC1 composite) were added to the required aspect ratio. The reactor vertical position was taken as a 90° inclination angle. The water level containing the catalyst was marked as H and followed by air sparging (0.009 ms⁻¹ to

0.033 ms⁻¹) at the required flow rate maintained for about 10 min for hydrodynamic behaviour in the reactor to stabilize. After the fluidized bed had stabilized, the new level of the phases was noted as H_{eb}, thus quantifying gas volume in the liquid phase. The difference in two levels before and after sparging air was used to determine gas hold up. The phase holdup was estimated from the static bed height (H) and expanded bed height (H_{eb}) using equation (22)-(23)-(24):

$$\varepsilon_g = \frac{H_{eb} - H}{H_{eb}} \quad (22)$$

$$\varepsilon_s = \frac{M_s}{\rho_s A H_{eb}} \quad (23)$$

$$\varepsilon_s + \varepsilon_l + \varepsilon_g = 1 \quad (24)$$

The superficial air velocity (U_g) was simply calculated using equation (25):

$$U_g = \frac{Q}{A} \quad (25)$$

where ε_s , ε_l , and ε_g represent solid, liquid, and gas holdup, respectively. M_s is the mass of the solid and ρ_s is the density of the solid. H and H_{eb} is the height and expanded bed height, respectively. Q is the gas flow rate (m³/h) and A is the cross-sectional area of the column. Gas hold plays an important role in liquid-gas mass transfer. It is important to note that, the gas flow rate contributes to the reactor cost of operation. Therefore, a correlation between the gas holdup and gas flow rate is given by [Ochieng *et al.* \(2003\)](#); equation (26).

$$\varepsilon_g = AU_g^n \quad (26)$$

where A and n values are the empirical constants calculated using Ms Excel solver using the experimental data. For gas holdup (ε_g) and gas-liquid mass transfer coefficient (K_{La}) correlation, a well-summarized correlation by [Ochieng *et al.* \(2003\)](#) was used equation (27), in which K_{La} was defined as:

$$KL_a = 1.53\varepsilon_g \quad (27)$$

Therefore, the correlation between U_g and K_{La} is given by:

$$KL_a = BU_g^n \quad (28)$$

where B is the empirical constant.

Solid concentration distribution was estimated using the gravimetric method. A given mass of supported photocatalysts with respect to the column aspect ratio was added to a known volume of water in the glass column reactor. Thereafter, the glass column reactor was placed at a selected inclination angle ($90^\circ - 50^\circ$) before sparging air through the gas diffuser. The air supplied was regulated using an air rotameter (0.009 to 0.033 ms^{-1}) and then maintained to a required constant flow rate for about 10 mins for stabilization. After stabilization, 10 ml samples containing water and supported catalyst were taken at 5, 15, 25, and 35 cm from the gas diffuser using a 10 mL pipette through the gas outlet (8). The samples were filtered followed by drying of filter paper containing the suspension. Thereafter, the weight difference between the dried laden filter paper and clean filter paper was used to compute the concentration of solids in the samples. The solid concentration distribution across the column was therefore estimated.

3.6.5.2 Photodegradation in fluidized bed reactor

The rate of adsorption and photodegradation greatly depends on the magnitude of solid-liquid and liquid-gas mass transfer. Solid concentration distribution and gas holdup govern the concentration of substrates to the photocatalyst surface and the dissolution of air-oxygen in the aqueous solution. In particular, the presence of oxygen as an electron scavenger is vital for prolonging the recombination of electron-hole pairs. Therefore, the solid-liquid and gas-liquid mass transfers influence the adsorption and photodegradation. The optimum hydrodynamic conditions for the adsorption and photodegradation process were selected based on the preliminary studies conducted.

3.7 Data and error analyses

Microsoft Excel was used for data and error analyses. All experiments were repeated at least two times, and averages are reported for error analyses. The results shown are obtained from the average data values of two independent repeated experiments. The standard deviation (SD) calculated values are represented as error bars in figures plotted using Origin 9 software.

CHAPTER 4

4 RESULTS AND DISCUSSION

4.1 Catalyst and support material characterization

The characterization of prepared materials was done to confirm the effect of physicochemical features on the adsorption and photodegradation process. The optical bandgap of the materials was determined using solid-state electronic adsorption spectra obtained from a UV-vis spectrophotometer. The materials were tested under different operation parameters mainly photocatalytic operation and hydrodynamic parameters, and the results were reported.

4.1.1 X-ray Diffraction analysis

The X-ray diffraction (XRD) patterns for the materials are shown in Figure 4-1 (a)-(b). The XRD results showed that both TiO₂, ZnO, and the hybrids had crystalline structure phases with a series of defined peaks. The TiO₂ XRD pattern profile observed at 2 Theta values of 25.28°, 37.8°, 48.04°, 53.89°, 55.06° and 62.68° related to (100), (004), (200), (105), (211) and (204) reflections respectively revealed the existence of anatase TiO₂ Figure 4-1 (b). Similarly, ZnO peaks were observed at 2 Theta values of 39.94°, 34.61°, 34.6°, 36.47°, 47.55°, 56.60°, 62.83°, 66.38°, 67.97° and 69.10° related to (100), (002), (101), (102), (100), (103), (200), (112) and (201) reflections respectively confirm the planes of hexagonal wurtzite ZnO (Figure 4-1 b).

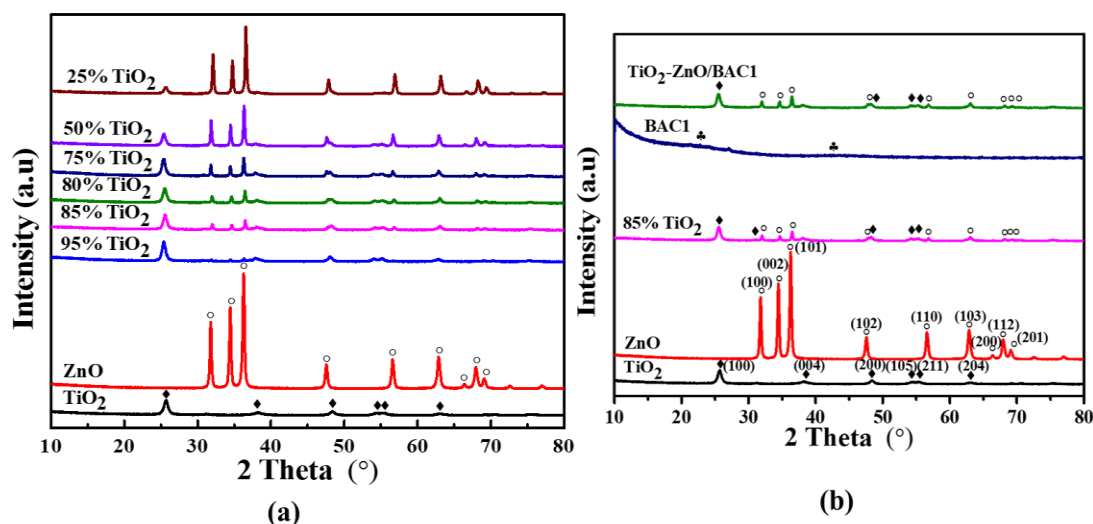


Figure 4-1. (a) XRD pattern of pure TiO₂, ZnO, and their hybrids based on percentage composition, and (b) XRD profile of pure TiO₂, ZnO, and prepared activated carbon, superior hybrid, and the composite.

The defined phases for TiO₂ and ZnO obtained are similar to other studies (Benton *et al.*, 2016; Liao *et al.*, 2008). All hybrids showed an increase in individual species constituent defined peaks with increased percentage composition and vice versa, indicating a successful hybridization. The BAC1 only had two broad diffractions at 2 thetas 23.5 ° and 43 °. The absence of a sharp peak reveals a predominantly amorphous structure, typically characteristic of activated carbon (Elisadiki *et al.*, 2019).

4.1.2 Fourier Transform Infrared Spectroscopy Analysis

The successful hybridization and incorporation of BAC1 support were inferred by FTIR analysis. Figure 4-2 presents the FTIR spectra of BAC1, TiO₂, ZnO, TiO₂-ZnO (85%TiO₂) hybrid and, TiO₂-ZnO/BAC1 (40% BAC1) composite. The characteristic absorption peak appearing at around 500 cm⁻¹ is assigned to Zn-O (El Mragui *et al.*, 2019). The band peak appearing at around 680 cm⁻¹ is attributed to Ti-O stretching and Ti-O-Ti bridging stretching mode (Mofokeng *et al.*, 2017). The samples show a low-frequency absorption band corresponding to bending vibrations of adsorbed water molecules and stretching vibration of O-H at around 1654 and 3414 cm⁻¹, respectively. The peak centred around 814 cm⁻¹ is ascribed to the stretching of Zn-O-Ti mode and was also observed by Mofokeng *et al.* (2017).

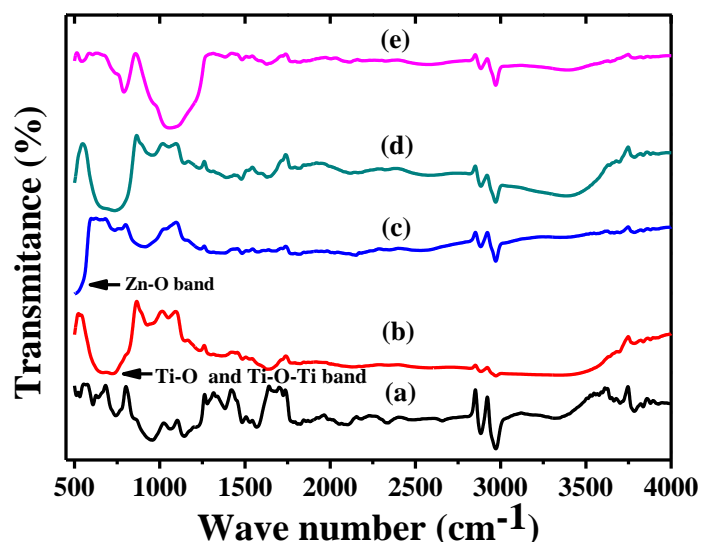


Figure 4-2. FTIR spectra of (a) BAC1, (b) TiO₂, (c) ZnO, (d) TiO₂-ZnO hybrid, (e) TiO₂-ZnO/BAC1 composite

With the introduction of BAC1 support, the peak width at around 1079 cm⁻¹ became broader for the composite which is attributed to C-N stretching vibration, corresponding to the observed peak for BAC1 (Figure 4-2). According to Benton *et al.* (2016), the broadening could occur due to exposure of C-N, which might have been limited before the incorporation of the hybrid and lengthy drying of the composite. A similar observation was made by Table 4-1 depicts a summary of the absorption spectrum with possible assignments in the material.

Table 4-1. FTIR spectra with possible assignments (Benton *et al.*, 2016; El Mragui *et al.*, 2019; Mofokeng *et al.*, 2017).

Frequency (cm ⁻¹)	Possible Assignment
510 cm ⁻¹	Zn-O stretching mode (hexagonal phase)
708 cm ⁻¹	Ti-O stretching and Ti-O-TiO bridging stretching mode
814 cm ⁻¹	Zn-O-Ti stretching mode
1079 cm ⁻¹	C-N stretch of amide-I in protein
1588 cm ⁻¹	C=C stretch in the aromatic ring and C=O stretching in polyphenols

1654 cm ⁻¹	Adsorbed water bending
2877 cm ⁻¹	O-H stretch in carboxylic group
2972 cm ⁻¹	C-H stretch mode in alkanes
3414 cm ⁻¹	OH stretch in a hydroxyl group

Overall, the IR spectra suggest that TiO₂-ZnO/BAC1 composite have functional groups that include TiO₂, ZnO, and BAC1 support. This confirms the successful hybridization with ZnO and BAC1 incorporation to TiO₂.

4.1.3 Scanning Electron Microscope

Scanning Electron Microscope (SEM) analysis was carried out to understand the surface morphology of BAC samples, TiO₂, ZnO, 85%TiO₂-ZnO hybrid, and TiO₂-ZnO/BAC1 (40% activated carbon composition) as shown in Figure 4-3 and Fig 4-4. The comparison of the morphologies was done under a similar magnification of 50 μ m. It can be seen after carbonization at 400 °C non-porous carbon with block-like structures on the surface were produced (Figure 4-3 a). With the introduction of the KOH activating agent, more pores were formed due to the intercalation of potassium onto the carbon surface (Elisadiki *et al.*, 2019). An increase in the KOH ratio subsequently led to an increase in the surface roughness and structural defect on the pores. Figure 4-3 (a)-(d) show pore cavities of the un-activated carbonized banana peel and activated carbonized banana peel at different KOH impregnation ratios. The increase in the KOH concentration induces an increased C-KOH reaction rate, causing the carbon structure to burn off. Therefore, this might result in decreased surface area and pore volume (Xue *et al.*, 2019).

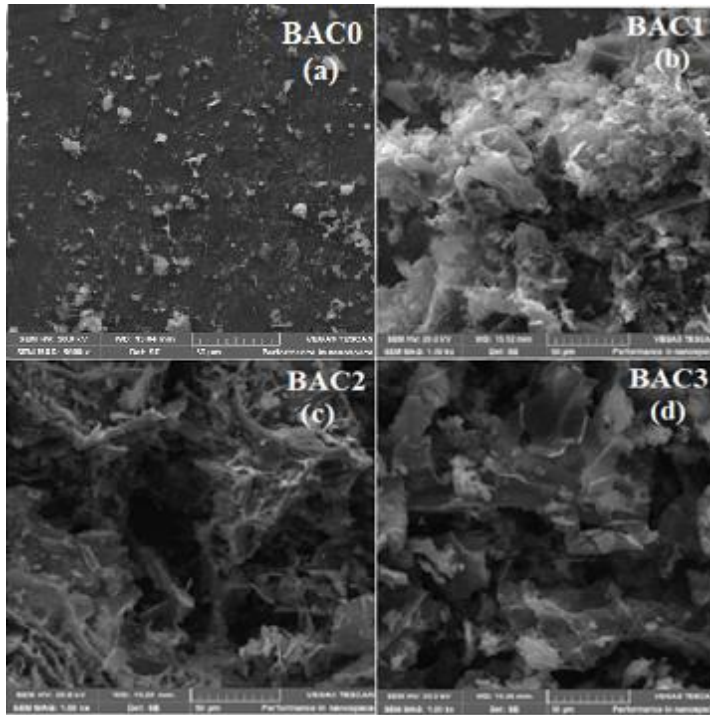


Figure 4-3. SEM images (magnification: 50 μm) (a) carbonized peel (char) activated carbon at char: KOH ratio 1:1 (b), 1:2 (c), and 1:3 (d).

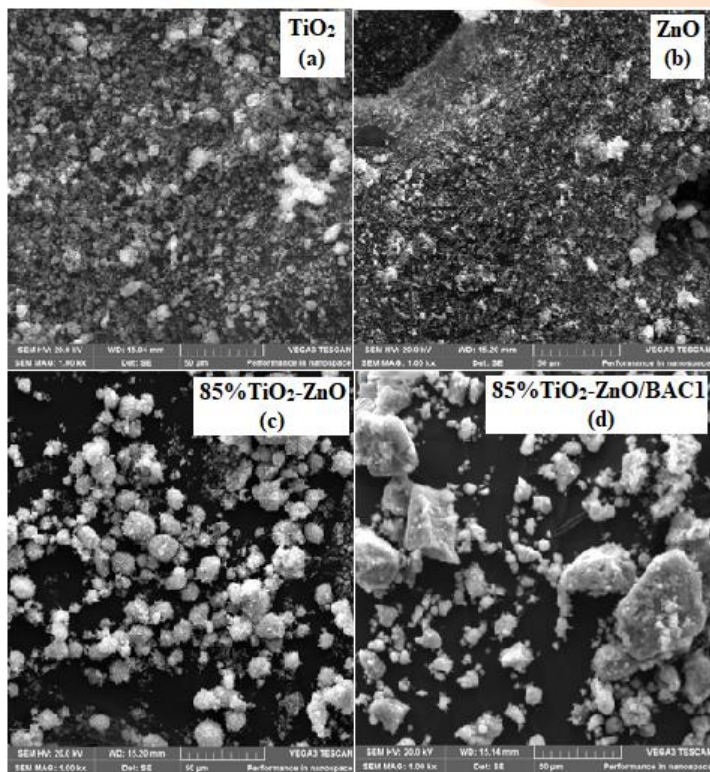


Figure 4-4. SEM images for TiO₂ (a), ZnO (b), 85%TiO₂-ZnO hybrid (c), and 85%TiO₂-ZnO/BAC1(d).

The SEM images of TiO₂ and ZnO show the existence of almost uniform spherical shape particles with a degree of homogeneity (Figure 4-4 a-b). The 85%TiO₂-ZnO micrographs exhibit a plausible high tendency of agglomeration, confirming successful hybridization (Figure 4-4 c). Siwińska-Stefańska *et al.* (2018) demonstrated the synthesized TiO₂-ZnO via the sol-gel method, showing the presence of spherical particles with a high tendency of agglomeration. In Figure 4-4 d, the 85%TiO₂-ZnO/BAC1 depicts the undefined morphology but with good adherence to the compositions signifying the good binding property of inert colloidal silica used in the preparation (Benton *et al.*, 2016; El *et al.*, 2019).

4.1.4 Brunauer-Emmett-Teller

The specific surface area of an adsorbent used as support material is a key factor influencing adsorption activity and consequently photocatalytic performance (Li *et al.*, 2016). The pores of catalysts and activated carbon derived from the banana peel (BAC) were determined using N₂ adsorption-desorption isotherms as shown in Figure 4-5 a-d. It is observed that the adsorption capacities increased remarkably from BAC0 to BAC1 (1:1 activation ratio) followed by a slight decrease with an increase of activation ratios of 1:2 (BAC2) and 1:3 (BAC3) revealing the enhanced pore volume and surface area attributed to KOH activation. At a temperature around 700 °C, metallic K produced after reduction of K₂O intercalate into the carbon skeleton structure which consequently leads to the formation of more mesopores but also micropores (Xue *et al.*, 2019). However, it is difficult to maintain micropores at higher KOH activation thus consequently some created pores tend to collapse leading to decreased surface area and pore size. The BET surface areas (S_{BET}) of the BAC0, BAC1, BAC2 and BAC3 are 2, 2229, 1862, and 1639 m²/g, respectively. The highest S_{BET} of 2229 m²/g was observed for sample BAC1 having an activation ratio of 1:1. BAC0 exhibited the lowest N₂ adsorption capacity with 2 m²/g indicating the material is non-porous. Furthermore, at a higher KOH activation ratio, the adsorption capacity by BAC2 and BAC3 decreased indicating the reduction of pore size and surface area (Figure 4-5a). According to IUPAC classification, the BAC0 sample belongs to type I isotherm with no abrupt uptake of adsorbed volume at lower relative pressure, suggesting the presence of only micropores. Moreover, BAC1, BAC2, and BAC3 samples exhibit type IV isotherms with a hysteresis loop at P/P₀ of 0.4 to 1.0, suggesting the presence of well-developed mesopores (Elisadiki *et al.*, 2019).

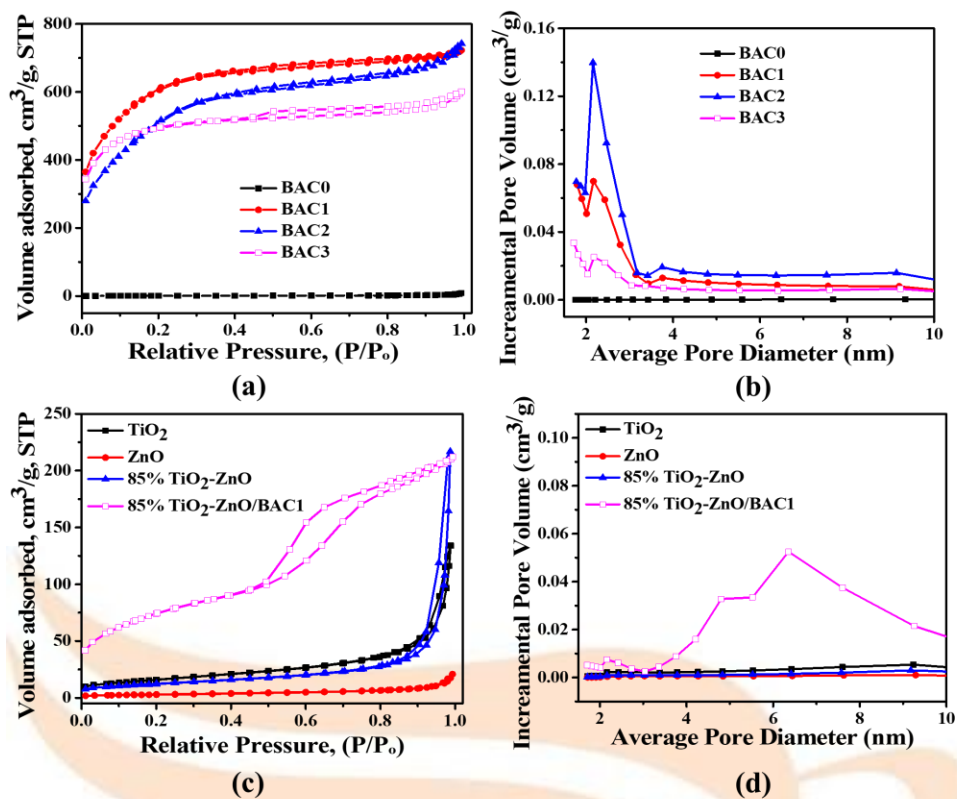


Figure 4-5 (a) and (c) N_2 sorption isotherms. (b) and (d) Pore size distribution curves

The pore size distribution of BAC samples was calculated using Barrett-Joyner-Halenda (BJH) methods. The obtained results (Figure 4-5a) indicated a general increase in the differential volumes and more pores formation when the samples were activated at different KOH activation ratios. However, at a higher activation ratio of more than 1:1, the differential volumes decreased because of pores collapsing. From the BJH curves of BAC samples, it is evident that the pore diameters of all the samples are around 2.5 nm, representing the mesoporous structure of the samples (Elisadiki *et al.*, 2019). The presence of mesopores is fundamentally important since it contributes to a large surface area and consequently high adsorption capacity favouring photocatalytic activity. BAC1 showing the highest surface area of 2229 m²/g was further used as catalyst support material.

The significant increase in the surface area 85%TiO₂-ZnO/BAC1 composite validates that BAC1 support material is successfully immobilized on 85%TiO₂-ZnO. Figure 4-5c, the observed increased BET surface areas (S_{BET}) of the 85%TiO₂-ZnO/BAC1 compared to 85%TiO₂-ZnO reveals the effect of BAC1 support addition. In addition, 85%TiO₂-ZnO/BAC1 composite shows a lower surface area of 268 m²/g compared to

the BAC1 support with 2229 m²/g. The 85%TiO₂-ZnO/BAC1 lower surface may be attributed to the low amount of BAC1 composition and blockage of BAC pores by TiO₂-ZnO constituents. All the unsupported catalysts exhibit type III isotherm with a convex shape at high relative pressure. Whereas the supported catalyst, 85%TiO₂-ZnO/BAC1 belongs to type IV with a type H₄ hysteresis loop at P/P_o > 0.4 which features an abundance of mesopores (Li *et al.*, 2016). Table 4-2 summarizes the surface area of all the samples.

Table 4-2 BET surface areas and pore volumes of the samples

Sample	Surface area, S _{BET} (m ² /g)	Pore volume, V _T (cm ³ /g)	Pore diameter, D average (nm)
BAC0 (1:0)	2	0.013694	22.563
BAC1 (1:1)	2229	0.487988	2.5834
BAC2 (1:2)	1862	0.385706	2.9812
BAC3 (1:3)	1639	0.301165	3.5639
TiO ₂	58	0.204235	15.283
ZnO	10	0.031058	14.496
85% TiO ₂ -ZnO	44	0.333581	32.484
85%TiO ₂ -ZnO/BAC1	268	0.310138	5.1384

4.1.5 Optical properties

Figure 4-6 shows the UV-vis adsorption (a) and photoluminescence (PL) (b) spectra of TiO₂, ZnO, and 85%TiO₂-ZnO materials. The bandgap energy (E_g) of the materials were estimated according to equation 29 (Benton *et al.*, 2017).

$$E_g = \frac{1240}{\lambda_{ex}} \quad (29)$$

where λ_{ex} is the exciting light wavelength on the semiconductor material. From the calculation, the bandgap energies of TiO₂, ZnO and 85%TiO₂-ZnO materials were found to be about 3.2, 3.5, and 3.1, respectively. It is clear that the bandgap of TiO₂ was reduced due to the shift of the visible spectrum (redshift). The 85%TiO₂-ZnO hybrid redshift is due to the presence of ZnO, which may be related to the formation of heterojunctions posing a synergistic effect.

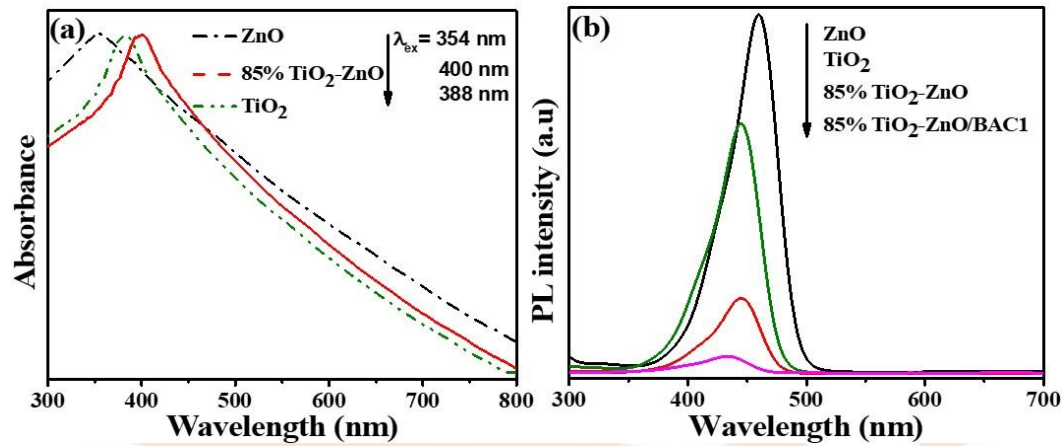


Figure 4-6. UV-vis spectrum in water (a) and PL (b) spectra of the materials.

In addition, the conduction band (CB) and Valence band (VB) positions of the semiconductor in the hybrid (85%TiO₂-ZnO) was calculated using Milliken electronegativity given by equations (30)-(31), a method adopted from Bai *et al.* (2021)

$$E_{CB} = \chi - E^e - 0.5E_g \quad (30)$$

$$E_{VB} = E_{CB} + E_g \quad (31)$$

where χ is the Milliken electronegativity of semiconductors present in the material. The χ values for SC, TiO₂ and ZnO are 5.82 and 5.78 eV, respectively. E_{CB} and E_{VB} are conduction and valence potentials edge. E^e is the free electron energy on the hydrogen scale equivalent to ca. 4.5 eV. The estimated E_{CB} and E_{VB} of the SC is summarized in Table 4-3.

Table 4-3. The estimated Conduction and Valence potential edge of the material.

SC	TiO ₂	ZnO
χ	5.82	5.78

E_g (eV)	3.2	3.5
E_{CB}	-0.28	-0.47
E_{VB}	2.92	3.03

The photoluminescence (PL) study was used to explore the fate of photogenerated species in the SC. In principle, the higher the electron-hole recombination, the higher the PL intensity and vice versa. [Benton *et al.*, \(2016\)](#) reported that, when the PL intensity is high, it implies high electron-hole recombination, leading to a low quantum yield of photogenerated species and subsequent reduced photocatalytic activity. The PL spectra of the TiO₂, ZnO, 85% TiO₂-ZnO hybrid and, 85% TiO₂-ZnO/BAC1 measured with an excitation wavelength of 450 nm is shown in Figure 4-6 (b). The PL intensity follows ZnO > TiO₂ > 85% TiO₂-ZnO > 85% TiO₂-ZnO/BAC1 order.

The results revealed that the combination of TiO₂ with ZnO greatly decreased the resultant PL intensity which is attributed to reduced recombination. The reduced recombination showed by the 85% TiO₂-ZnO hybrid may be due to the formation of the heterojunction. The formation of heterojunction plays a significant role in charge separation by allowing the electron transfer from CB of TiO₂ to ZnO and hole from VB of ZnO to TiO₂ ([Juan *et al.*, 2018](#)). Furthermore, the introduction of activated carbon (BAC1) to 85% TiO₂-ZnO hybrid further reduces PL intensity, which proves to suppress electron-hole recombination. From these results, 85% TiO₂-ZnO/BAC1 showed the lowest PL intensity attributed to the lowest electron-hole recombination, which can lead to an improved photocatalytic degradation performance.

4.1.6 Thermal decomposition behaviour

The thermal analysis and the stability of the material were determined by thermal gravimetric analysis (TGA), and the result are shown in Figure 4-7. The thermogram of BAC1 shows a mass loss at a temperature of approximately 90 °C, a slow decline in weight from 90 °C to 600 °C, then an increase in weight loss rate at a temperature beyond 600 °C.

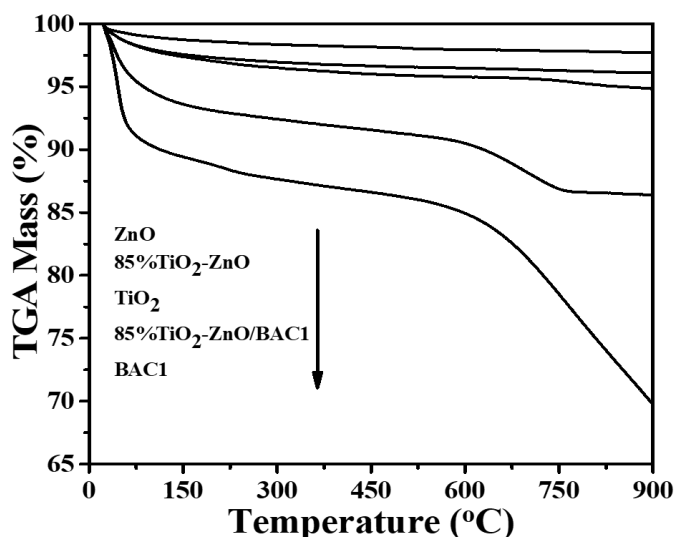


Figure 4-7. TGA analysis of the synthesized materials.

The initial mass loss of 9.5% at 90 °C is due to the evaporation of moisture from the material. The second weight loss of 5.6% (>90-600 °C) can be assigned to the decomposition of some functional groups such as hydroxyl or carboxylic present in the BAC1 structure (Table 4-1). The third weight loss (>600-900 °C) with a mass loss of 14.9% occurs due to the decomposition of the carbon skeleton. For ZnO TGA profile showed a mass loss of 1.4% (25-200 °C), followed by 0.6 % and finally 0.3 %. The TiO₂ TGA curve showed two distinct stages. The first stage (25-200 °C) with a mass loss of 2.9 % is associated with the evaporation of absorbed water and solvent (methanol) molecules absorbed on the surface of the material. The second mass loss of 1.4 % in the range 400-900°C can be attributed to phase transformation to rutile from anatase crystalline structure (above 600 °C). Such results are in line with reports in the literature Benton *et al.* (2016). The TiO₂-ZnO exhibited higher thermal stability as compared to pure TiO₂. However, pure ZnO proved to be more thermally stable. This implies ZnO acted as a thermal stabilizer on the TiO₂-ZnO hybrid. From the literature, the mass loss of TiO₂-ZnO prepared by the sol-gel method is associated by mainly three distinct steps evaporation of the water of crystallization (25-300 °C), dihydroxylation of precursors (300-470 °C) and (above 400°C) TiO₂ phase transformation (Siwińska-Stefańska *et al.*, 2018). It is also worth noting, 85%TiO₂-ZnO/BAC1 and BAC1 almost share the same mass loss profile. Therefore, the unexpected significant mass loss in 85%TiO₂-ZnO/BAC1 could be due to the composition of the thermally unstable BAC1.

4.1.7 Particle size distribution of 85%TiO₂-ZnO/BAC1

The 85%TiO₂-ZnO/BAC1 particle size was analysed using laser diffraction (Malvern Mastersizer 3000E coupled with a wet dispersion unit). The size volume and distributions were determined from the resultant bimodal and unimodal distribution curves, respectively and results are shown in Figure 4-8 a-b (Appendix E). The cumulative undersize for both number and volume fractions is shown in Figure 4-8 (c)-(d).

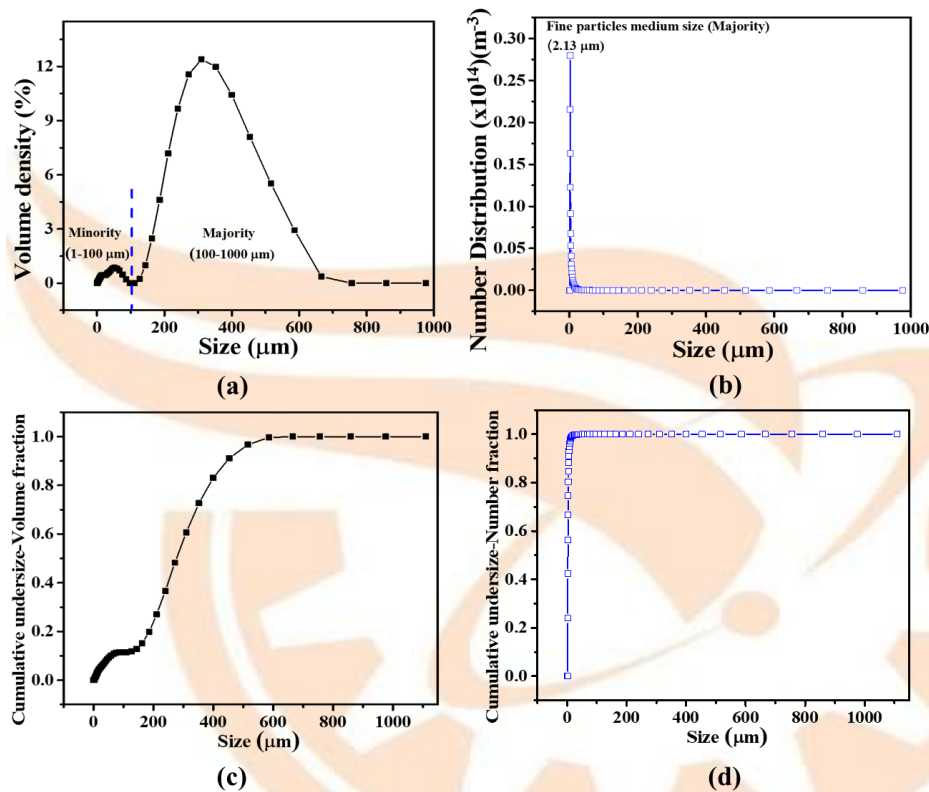


Figure 4-8. Particle size volume distribution (a), number distribution (b), and cumulative undersize for both number and volume fraction (c)-(d).

The bimodal distribution can be ascribed to agglomeration and Figure 4-4 c-b shows that the TiO₂-ZnO has a high tendency of agglomeration during synthesis via the sol-gel method (Siwińska-Stefańska *et al.*, 2018). The bimodal volume distribution shows that 85%TiO₂-ZnO/BAC1 larger particles, ranging from 100-1000 μm were dominant whereas the finer particles ranging from 1-100 μm had an insignificant contribution to particle volume. From the unimodal distribution, it was found that 85%TiO₂-ZnO/BAC1 composition has a higher number of fine particles with medium size of 2.13 μm compared to larger particles. In addition, the external surface area of 85%TiO₂-

ZnO/BAC1 was calculated using the method of moments, Ntuli and Lewis. (2010) and was found to be 3.2 m²/g.

4.2 Photodegradation in lab-scale stirred tank reactor experiments

4.2.1 Effect of the KOH activation ratio on the AC adsorption activity

The surface properties and texture of an activated carbon governing its adsorption performance usually differ depending on carbon source, carbonization, and activation conditions. Therefore, the effect of the KOH impregnation ratio on banana peel activated carbon adsorption activity was studied. In this experiment, 0.024 g of adsorbent (BAC0, BAC1, BAC2, or BAC3) was dispersed in 80 mL of 30 ppm R6G (pH 7) under constant stirring (250 rpm) until equilibrium was attained. Samples were collected at predetermined time intervals for analysis, and the results are shown in Figure 4-9 (a)-(b). It can be inferred that the adsorption capacity of the carbon greatly depends on the surface area and pore volume which is significantly influenced by the KOH activation ratio (See Figure 4-5a).

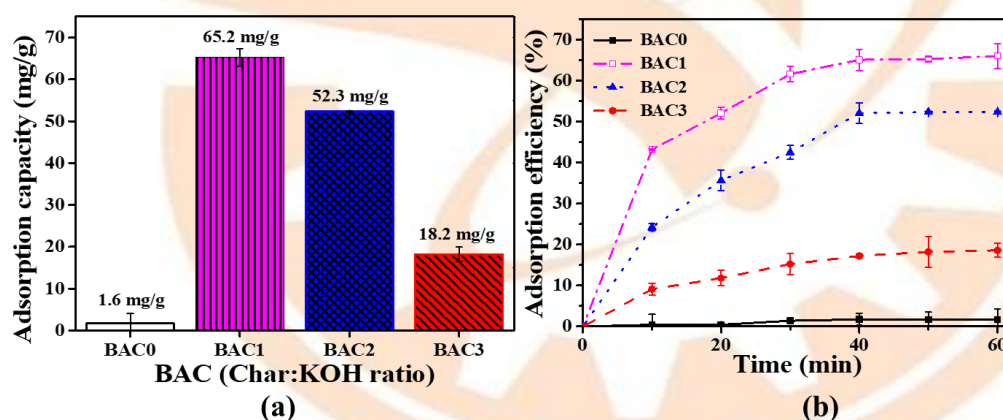


Figure 4-9. Effect of KOH: char ratio on adsorption performance.

All banana peel activated carbons (BAC), showed a higher adsorption capacity and efficiency compared to non-activated carbon from banana peels. The low adsorption capacity of 1.6 mg/g showed by non-activated carbon from banana (BAC0) is due to a small surface area that widens through the activation process. In contrast (refer Figure 4-9), the decrease in adsorption capacity of BAC with an increase in KOH impregnation ratio higher than 1 was observed. The decrease in adsorption capacity results from a high degree of intercalation of metallic K on the carbon surface which not only forms more mesopores but also larger which easily collapse (Xue *et al.*, 2019). Under the

KOH activation ratio ranges for activated carbon tested, BAC1 had the highest adsorption capacity (65.2 mg/g) on R6G dye. Therefore, BAC1 with an impregnation ratio of 1:1 (Char: KOH) with the highest surface area of 2229 m²/g was further used as the catalyst support material (Table 4-2).

4.2.2 TiO₂-ZnO photocatalytic activity based on their mass ratio

The effect of TiO₂ and ZnO composition on the hybrid photocatalytic activity was investigated by varying their mass ratios in a lab-scale stirred reactor. Briefly, 80 mg of solid loading and 15 ppm R6G suspension was first stirred in the dark to achieve adsorption equilibrium before being exposed to UV irradiation to initiate photodegradation. Samples collected at predetermined time intervals were analysed using a UV-vis spectrophotometer to monitor the adsorption and photodegradation process. From the results (Figure 4-10 a), the hybrids with 80%, 85%, and 95% of TiO₂ composition showed higher photocatalytic activity corresponding to 95.7%, 97.9%, and 94.8% colour reduction, respectively, as compared to pure TiO₂ and ZnO, which showed 85.3% and 39.5%, respectively. The hybrid (85% TiO₂ composition) had the highest colour removal of 97.9%.

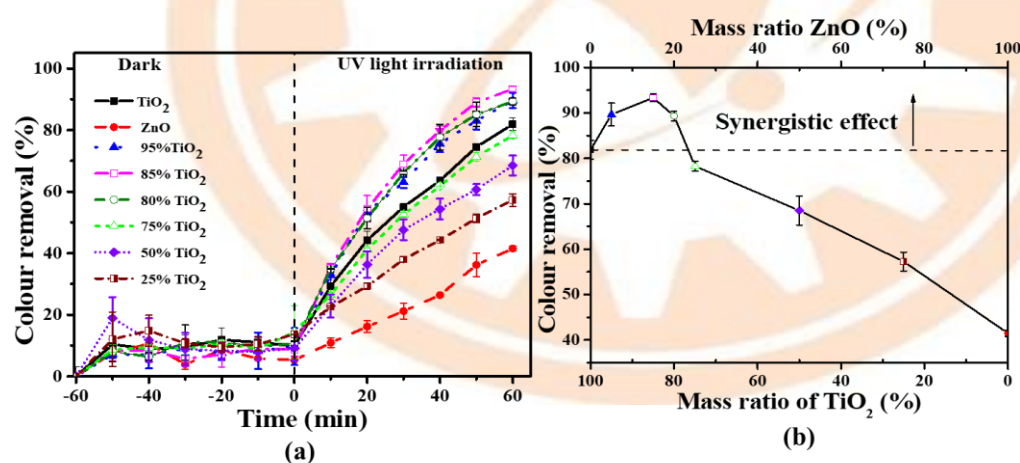


Figure 4-10. (a) Effect of hybridization by the different mass ratios of TiO₂-ZnO on adsorption and photodegradation rate. (b). Synergistic effect of the hybrids based on the varied mass fraction.

A synergistic effect is revealed when the activity of a hybrid exceeds both individual constituents. The results (Figure 4-10 b) showed that a synergistic effect was obtained at 80-95% TiO₂ composition, and 85% was the optimum. The improved photocatalytic activity showing a synergistic effect is attributed to the sufficient electron-hole

separation which is related to reduced PL intensity observed in Figure 4-6 (b). Combining TiO₂ and ZnO can result in the formation of heterojunction allowing the transfer of electrons from the TiO₂ conduction band to ZnO and holes from the ZnO valence band to TiO₂. The synergistic effect is enhanced by having enough ZnO to trap electrons (Benton *et al.*, 2016). The low colour removal showed by ZnO and hybrids (< 80% TiO₂ composition) is due to rapid recombination resulting from inadequate electron-hole separation as shown in Figure 4-6 b. The optimum TiO₂ to ZnO mass ratio varies from one study to another. A 75% and 99.5% composition in TiO₂-ZnO showed the highest degradation of molasses and antipyrine, respectively (Benton *et al.*, 2016; Tobajas *et al.*, 2017). The 15% of ZnO on TiO₂ (referred to as 85%TiO₂-ZnO) proving to be superior was used in the subsequent experiment.

4.2.3 Photocatalytic efficiency of TiO₂- ZnO based on BAC1 composition

Supporting a photocatalyst onto an adsorbent plays an important role in enhancing photocatalytic activity. The adsorbent concentrates the substrates near the active surface and consequently degraded more quickly with the short-living active species (Wang *et al.*, 2016). However, exceeding the optimum amount of adsorbent on the photocatalyst, most pollutants are not degraded but transferred from one phase to another, leading to secondary pollution (Benton *et al.*, 2016). Consequently, making the process not feasible based on green chemistry principles. Therefore, the percentage composition of optimized banana peel activated carbon (BAC1) on a superior 85%TiO₂-ZnO hybrid was evaluated. The experiment was done in a lab-scale stirred tank reactor using 0.6 g/L loadings, 30 ppm R6G (80 mL), pH 7, and 250 rpm as experimental conditions were kept constant. The adsorption equilibrium and photodegradation time was 1 h and 2.4 h, respectively.

At first, colour removal due to adsorption was monitored until equilibrium was achieved before turning on the UV to initiate photodegradation. Colour removal due to photodegradation increased with an increase in BAC1 loading up to 40% composition, indicating BAC1 as a photocatalytic promoter (Figure 4-11). In contrast, the composition of BAC1 above 40% resulted in a decrease in photocatalytic activity. The decrease in degradation efficiency is because of the decreased amount of active photocatalyst present as more 85%TiO₂-ZnO/BAC1 composite composed of BAC1 than TiO₂-ZnO (85% TiO₂). Consequently, most of the adsorbed substrates are not fully degraded.

Besides, the adsorption efficiency is found to increase continuously with increasing BAC1 composition. The continuous increase in adsorption is due to an increased number of available adsorption sites (Benton *et al.*, 2016). On the other hand, adsorption at a higher BAC1 loading (>40%) only concentrates the substrate around the catalyst surface without them being fully degraded. It is evident that the photocatalytic degradation of R6G is strongly favoured at 40% BAC loading (Figure 4-11). The enhanced photocatalytic activity is attributed to the integrated function of 85%TiO₂-ZnO and activated carbon (BAC1) acting as a good electron donor and acceptor, respectively, leading to sufficient electron-hole recombination (refer Figure 4-6 a-b). Moreover, activated carbon acting as a good adsorbent concentrate the substrates near the active site of the catalyst surface which is quickly degraded by the unstable active species.

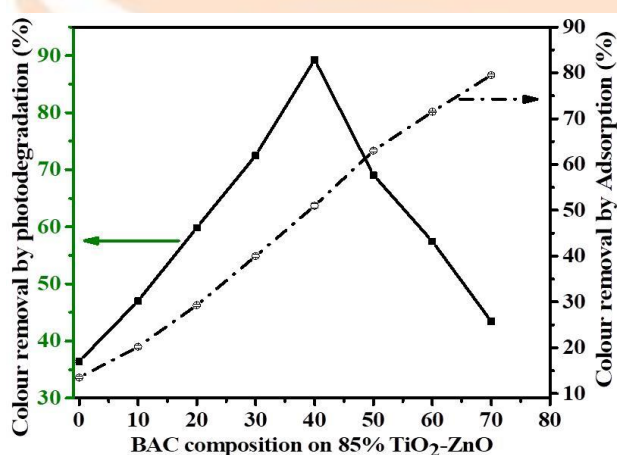


Figure 4-11. Effect of BAC1 support composition on TiO₂-ZnO hybrid activity.

Experimental condition: 30 ppm, 0.7 g/L catalyst dosage, and pH 7.

At 40% BAC1 composition, colour removal due to adsorption was 49.4% resulting in the highest photodegradation rate of 91.0%. Therefore, 40% BAC1 composition was selected as optimum for feasible degradation of R6G dye. Sivakumar *et al.* (2016) reported 10% activated carbon composition in TiO₂-based composite showed the highest photocatalytic degradation of R6G dye. However, in this study, 40% activated carbon composition was found to be the optimum. The optimum composition referred to as 85%TiO₂-ZnO/BAC1 was used throughout the subsequent experiments.

4.2.4 Effect of BAC1 composition on photocatalytic reaction kinetics

The kinetic analysis was studied to understand the degradation rate and feasibility based on banana activated carbon (BAC1) composition onto superior 85%TiO₂-ZnO. The kinetics of the heterogeneous photocatalytic reaction in aqueous solutions is widely described by Langmuir-Hinshelwood (L-H) model expressed in Equation (32).

$$r = -\frac{dC}{dt} = k_r\theta_s = \frac{k_r k_{ad} C}{1 + k_{ad} C} \quad (32)$$

where r equal to $-dC/dt$ are degradation rate, θ_s is the substrate concentration, k_r is the rate constant (mMh^{-1}), t is the time of irradiation to light and k_{ad} refers to adsorption constant (mM^{-1}). But when the initial concentration of the substrate used is low ($C_0 = <10^{-3} \text{ M}$), $k_{ad}C$ becomes negligible ($k_{ad}C \ll 1$). At this condition, the degradation process could be explained by pseudo-first-order kinetic law with respect to C , a simplified form of L-H Equation (33)-(34).

$$r = -\frac{dC}{dt} = k_r k_{ad} C = kC \quad (33)$$

Integrated to:

$$\ln \frac{C_0}{C} = kt \quad (34)$$

where k represents the first-order reaction constant (min^{-1}), C_t is the dye concentration at time t , and C_0 is the initial dye concentration ($t = 0$).

As demonstrated by [Benton *et al.* \(2016\)](#), the degradation process involving a photocatalyst supported on activated carbon, the degradation rate can be monitored using the second-order reaction model as:

$$\frac{1}{C} - \frac{1}{C_0} = k_2 t \quad (35)$$

where k_2 is the second-order rate constant (min^{-1})

Therefore, the experimental data obtained under the effects of BAC1 composition to R6G degradation were subjected to two kinetics models (pseudo-first-order reaction and second-order reaction models). Table 4-4 shows the effect of BAC1 loading on degradation rate-based kinetics data summarized from equation (34) and equation (35)

plots (Appendix F). The k and k_2 values were obtained from the graph slope. The R^2 values were used as a measure of model adequacy in describing the degradation process. The results in Table 5-1 show that k values increased from 0.0030 min^{-1} to 0.0790 min^{-1} , corresponding to BAC1 composition from 0 to 40%, respectively. However, a decrease in k values with BAC1 composition above 40% was observed. In contrast, the k_2 value increased simultaneously with an increase in BAC1 loading. It is evident that $\text{TiO}_2\text{-ZnO}$ based composite with 40% BAC1 had the highest k of 0.0790 min^{-1} , thus confirming its highest R6G colour removal due to photodegradation (refer Figure 4-12).

The R^2 value for pseudo-first-order reaction decreased, while the R^2 value for the second-order model increased with increased BAC1 composition. The R^2 trend indicates the predominance of adsorption over the photodegradation process (Table 4-3). The increase in BAC1 composition favours the adsorption process over photodegradation due to the reduced amount of 85% $\text{TiO}_2\text{-ZnO}$ in the composite. Therefore, the degradation process ends up fitting the second-order model. This is expected as the AC adsorption tends to fit the second-order model (Jonidi-Jafari *et al.*, 2015).

Table 4-4. Shows summarized kinetic data for photodegradation by varying BAC1 loading. Experimental condition: C_0 - 30ppm, 0.7 g/L catalyst dosage and pH 7.

Reaction Order	1 st Order		2 nd Order	
BAC1 loading.	k	R^2	k_2	R^2
(%)	(Min^{-1})		(Min^{-1})	
0	0.0030	0.9964	0.0015	0.9440
10	0.0042	0.9937	0.0024	0.9895
20	0.0055	0.9904	0.0042	0.9665
30	0.0630	0.9818	0.0065	0.9755
40	0.0790	0.9834	0.0109	0.9637

50	0.0680	0.9625	0.0119	0.9948
60	0.0640	0.9385	0.0131	0.9856
70	0.0053	0.9481	0.0148	0.9896

4.2.5 Comparison of photodegradation activity of catalysts

The photocatalytic performance for pure photocatalysts (TiO₂ and ZnO), superior 85%TiO₂-ZnO hybrid, and 85%TiO₂-ZnO/BAC1 composite was compared (Figure 4-12). Supported photocatalyst 85%TiO₂-ZnO/BAC1 showed the highest photocatalytic efficiency of 95.7.0% compared to unsupported TiO₂, ZnO, and 85%TiO₂-ZnO with 46.3%, 30.9%, and 55.5%, respectively. The increased efficiency for the 85%TiO₂-ZnO/BAC1 is attributed to BAC1, which increases absorptivity. The enhanced concentration of substrate molecules near the composite photoactive layer is advantageous for photocatalytic degradation because the absorbed molecules are immediately degraded with the short-living active radicals (Li *et al.*, 2016).

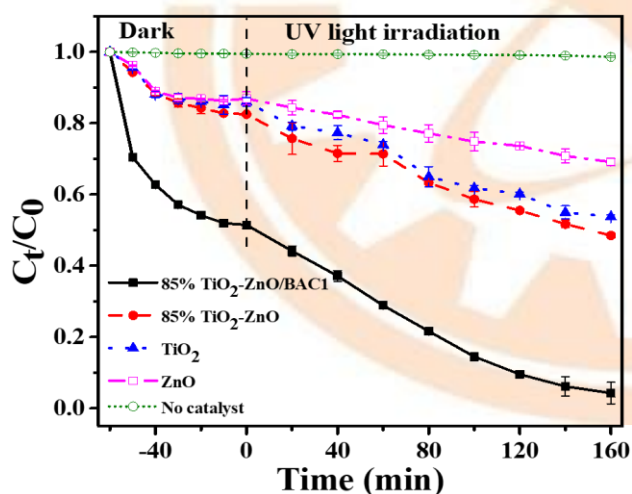


Figure 4-12. Compares adsorption and photodegradation performance of R6G dye over pure, superior hybrid and composite. Experiment conditions: 1.3 g/L catalyst dosage, 50 ppm, and pH 7.

Moreover, the TiO₂, ZnO and 85%TiO₂-ZnO showed low adsorption efficiency compared to the supported 85%TiO₂-ZnO/BAC1. This phenomenon is attributed to the inadequate adsorption capacity posed by the unsupported photocatalyst (Li *et al.*, 2016;

Wang *et al.*, 2016). Conversely, pollutants may not be concentrated near the active sites of the photocatalyst hence, the degradation rate is not favoured.

4.2.6 Main active species on photodegradation and its reaction mechanism

To further explore the 85%TiO₂-ZnO/BAC1 active species responsible for the degradation of R6G under UV irradiation, *in situ* capture experiment was conducted. This was achieved by adding ammonium oxalate (AO, quencher of h⁺), benzoquinone (BQ, quencher of O₂^{•-}), and isopropanol (IPOH, quencher of HO[•]) separately into the 50 ppm R6G dye solution and 85%TiO₂-ZnO/BAC1 1.3g/L suspension. With the addition of IPOH and BQ scavengers, the photocatalytic activity was decreased by 11.7% and 41.7%, respectively, compared to degradation of 91.6% without scavengers (Figure 4-13). However, the photocatalytic activity was significantly retarded by the addition of AO, corresponding to 61.0%. According to the results, the free radical species activity photogenerated from 85%TiO₂-ZnO/BAC1 composite for R6G degradation follows the h⁺ > O₂^{•-} > HO[•] order. It is evident that h⁺ and O₂^{•-} radicals are primarily the main active species responsible for the degradation of R6G under UV irradiation. However, h⁺ is more dominant in degrading R6G compared to O₂^{•-}.

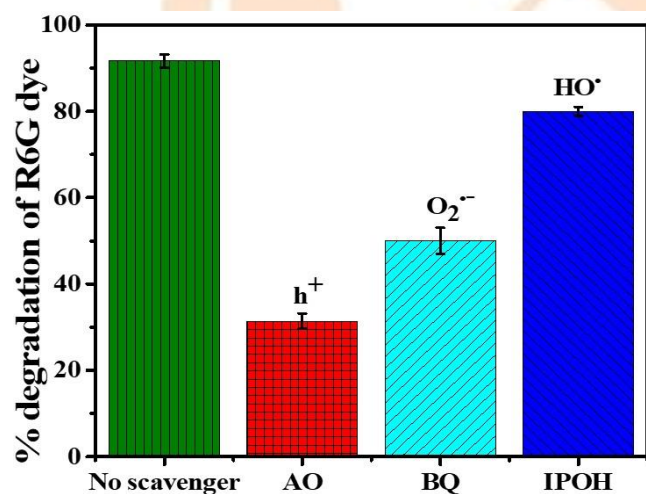


Figure 4-13. Percentage colour removal of R6G dye over 85%TiO₂-ZnO/BAC1 composite in the presence of various radical scavengers.

A previous study demonstrated an enhanced photocatalytic degradation of organic matter by the photosensitizing of dye toward TiO₂ (Lutic *et al.*, 2012). Dye photosensitization involves absorption of photons by dye molecule to generate dye cationic radical and indirect formation of free radicals responsible for degradation of

pollutants. Upon irradiation, electrons ejected from the dye HOMO can be transferred to the surface adsorbed oxygen to form $O_2^{\bullet-}$, further protonated to hydroperoxyl radical (HO_2^{\bullet}) and subsequently to hydrogen peroxide (H_2O_2). The conduction band edge (E_{CB}) potential of TiO_2 (-0.28eV) is less negative than the potential of R6G lowest unoccupied molecular orbital (LUMO) (-1.42) excited state conveying that, the electron transfer from the CB of TiO_2 is feasible. The transferred electron can participate in the generation of superoxide radical anions ($O_2^{\bullet-}$) responsible for the degradation of organic pollutants. In addition, the potential of R6G highest occupied molecular orbital (HOMO) (0.94) is less positive than the redox potential of HO^{\bullet}/H_2O , confirming that the holes cannot react with the surface OH groups to produce hydroxyl radicals (HO^{\bullet}). Hence, the formation of the HO^{\bullet} channel to degrade the R6G is impeded. According to the results, the dominance of h^+ can be attributed to the reduced formation of $O_2^{\bullet-}$. Figure 4-14 shows a proposed schematic diagram of the 85% TiO_2 -ZnO/BAC1 photocatalyst with their estimated conduction band (E_{CB}) and Valence band (E_{VB}) values (refer Table 4-3) and positions with respect to HOMO-LUMO levels of R6G dye.

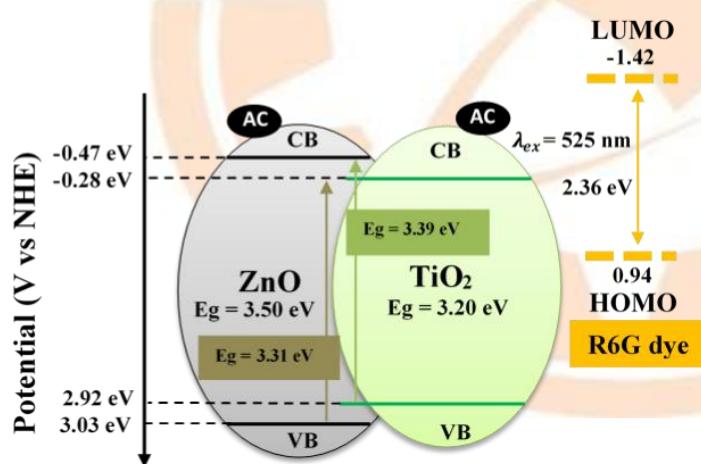


Figure 4-14. Proposed schematic diagram of the 85% TiO_2 -ZnO/BAC1 photocatalyst.

Figure 4-15 further illustrates the possible mechanisms of self-sensitized 85% TiO_2 -ZnO active species on degrading R6G dye.

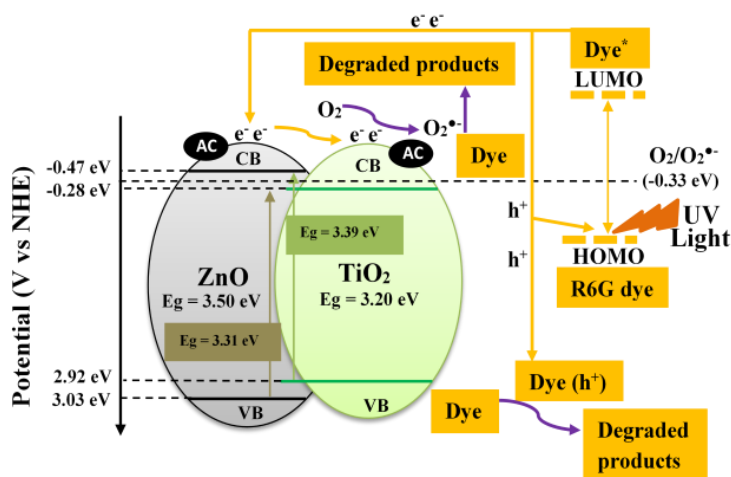


Figure 4-15. The possible mechanisms of self-sensitized 85%TiO₂-ZnO/BAC1 active species on degrading R6G dye.

As mentioned, since activated carbon is a good electron scavenger, some of the e⁻ photogenerated are trapped, leading to a decrease in O₂^{•-} formation to a certain extent. Besides taking advantage of increased electron-hole recombination in self-sensitized TiO₂, dyes can further extend the range of absorption of the photocatalyst to the visible light spectrum. Thus, minimizing the use of high external UV energy radiation. Nevertheless, dye sensitization can only be possible if the energy level of the excited state of the dye (dye^{*}) is higher than the energy level of the CB of the catalyst.

4.2.7 Photodegradation of the different dyes

The 85%TiO₂-ZnO/BAC1 photocatalytic activity was further tested on the degradation of different dyes (50 ppm, catalyst loading 1.3 g/L, pH 7) under 160 min UV irradiation after adsorption equilibrium was attained. The results of photocatalytic degradation of different dyes studied are presented in Figure (4-16). The equilibrium percentage adsorption of MB, MG, and R6G was 59.4%, 54.3% and 48.6%, respectively. The difference in adsorption is attributed to hydrophobic-hydrophobic interactions, and hydrogen bonding for adsorption of MB was stronger compared to the coulombic interactions responsible for the adsorption of the MG and R6G. The R6G had the lowest adsorption rate due to the weak coulombic attractions, hydrophobic-hydrophobic and hydrogen bonding. Similar behaviour was also observed by *Al-degs et al. (2008)*. Under 160 min UV irradiation, the percentage degradation of MB, MG, and R6G was 95.6%, 97.0% and 91.0%.

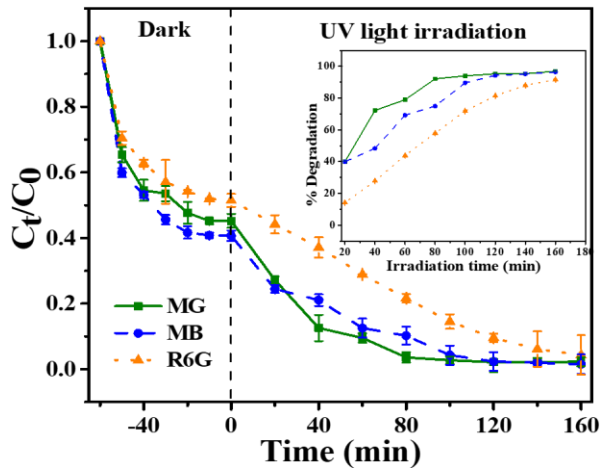


Figure 4-16. Degradation of different dyes using 85%TiO₂-ZnO/BACl.

Figure (4-16) shows the percentage colour under different irradiation. Interestingly, the MB was highly adsorbed compared to R6G and MG. However, MG had the highest percentage degradation after 20 min of irradiation. This was because the adsorption of the substrate onto the photocatalyst surface affects photons adsorption and subsequent generation of reactive radicals, leading to a significant effect on the rate of photodegradation. Despite increased adsorption and subsequently enhanced photodegradation rate by allowing the adsorbed substrate to be quickly degraded by the unstable active species. However, reaching the critical level due to strong interactions, the active surface of the photocatalyst is covered causing an inhibitive effect on the reaction between the active species generated and adsorbed dye molecules (Li *et al.*, 2016). Apart from MG showing relatively high adsorption affinity onto the photocatalyst surface, photosensitization of the photocatalyst can occur. Upon UV irradiation, MG ejects an electron either to positive holes or photocatalyst conduction band resulting in the generation of free radicals and dye cationic radical (MG^{•+}). As a result, dye cationic radical can undergo either hydrolysis or deprotonation to form a simple organic acid which is easily mineralized into simple products (Maria *et al.*, 2017).

4.2.8 Estimated COD removal of the dyes

It is vital to assess the chemical oxygen demand (COD) removal efficiency in any wastewater treatment process. The determination of the photocatalytic process on COD removal can provide useful information on the organic matter strength present in wastewater. The COD measurement is related to the total quantity of oxygen required

to oxidize slowly biodegradable and recalcitrant organic matter to simple compounds, CO₂, and water. The chemical oxygen demand (COD) spectrophotometric kit was used to measure the COD level of the samples using the dichromate method (Lawson-wood, 2016). The photodegradation experiments were carried out using 1.3 g/L 85%TiO₂-ZnO/BAC1 catalyst loading, 50 ppm solution of the dye at pH 7, 60 mins adsorption equilibrium time and 2.4 h UV irradiation time. The initial and final COD of the individual dye sample methylene blue (MB), malachite green (MG), and rhodamine 6G dye (R6G) was analysed using a spectrophotometer and the results are shown in Table 4-5. The initial concentration of the dyes used was 50 mg/L.

Table 4-5. *Estimated COD of the dyes before and after photodegradation.*

Sample COD	MB	MG	R6G
Before (mg/L)	131.0	124.7	137.4
After (mg/L)	38.8	28.3	27.9
COD removal %	70.4	77.3	79.7

The results show that COD removal in MB, MG and R6G was 70.4, 77.3 and 79.7%, respectively. The difference in COD removal on the dye may be due to different mineralization pathways followed by the dyes forming a recalcitrant intermediate which requires more time to be degraded into simpler products (Houas *et al.*, 2001; Maria *et al.*, 2017; Rasheed *et al.*, 2017). It was demonstrated that dye molecules like MG absorb UV light and subsequently undergo oxidative transformation leading to an indirect form of dye cationic radicals and free radicals. Thereafter, the dye cationic radicals may undergo either hydrolysis or protonation to produce degradable products and further mineralized simple products. Alternatively, MG mineralization may involve a series of free radical degradation chain reactions. This includes attack of chromophores ring structure (colour disappearing step), destruction of unsaturated double bonds, methylated diaminotriphenylmethane degradation and N-de-methylation process (Maria *et al.*, 2017). It was also revealed that photo-holes generated by the photocatalyst are not involved in the initial step to degrade MB dye. Instead, hydroxyl radicals generated from the oxidation of water by holes attack the C-S⁺=C functional

group in MB, followed by a series of mineralization step down to the final products. Therefore, depending on the degradation and mineralization pathways followed by different dyes, more time may be required for complete mineralization to reduce the recalcitrance of the compound present.

4.2.9 Photodegradation operational parameters and kinetics

Operating parameters are known to affect photocatalytic activity. These include pH, catalyst loading, initial concentration, temperature, reusability, and energy requirements. Therefore, the effect of operation parameters on the degradation of R6G dye was evaluated.

4.2.9.1 Effect of initial solution pH

The solution pH is an important parameter affecting the overall photocatalytic degradation of dyes. Therefore, it was of interest to study the influence of pH on the adsorption and photodegradation of R6G dye using 85% TiO₂-ZnO/BAC1 (1.3 g/L) by varying the initial pH of R6G dye solution (pH 2-11) and keeping the concentration of 70 ppm constant under UV irradiation. The initial pH of the solution was adjusted using HCl or NaOH. The highest adsorption and degradation efficiency were achieved at pH 8 of 23.9% and 86.7%, respectively, resulting in the highest overall colour removal of 89.9% ($k = 0.0126 \text{ min}^{-1}$) as shown in Figure 4-17 (a)-(b). High colour removal was observed in basic media compared to acidic media. However, beyond pH 8, a significant decrease in colour removal was observed. This effect can be mainly explained by the surface charge of TiO₂ and the cationic nature of the R6G dye.

Moreover, Wang *et al.* (2013) reported a PZC of 7.2 for a hybrid composed of TiO₂-ZnO supported on bamboo charcoal almost similar to the determined PZC of 85% TiO₂-ZnO/BAC1 (PZC 7.6 shown in Appendix G). In alkaline and acidic conditions, the TiO₂-ZnO based composite surface could be protonated or deprotonated. Thus, the surface of the TiO₂-ZnO/BAC1 catalyst would be positively charged when pH is below 7.6 (pH < PZC) and negatively charged when the pH is above 7.6 (pH > PZC).

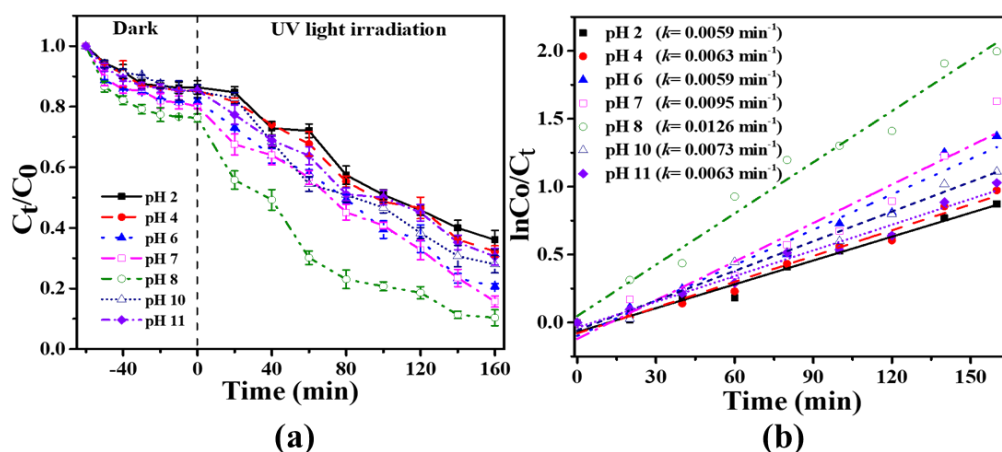


Figure 4-17. (a) Effect of pH on adsorption and photodegradation of R6G dye colour. (b) Degradation kinetics at different initial pH.

In addition, the R6G dye poses a net positive charge due to its cationic nature. At pH above 7.6, the TiO₂-ZnO/BAC1 surface is highly negatively charged thus, it results in high adsorption of the cationic dye substrate due to coulombic attraction forces. Below pH 7, there was a decrease in the adsorption efficiency of the substrate. The decrease in adsorption at pH (Below 7.6) was due to coulombic repulsion between the 85%TiO₂-ZnO/BAC1 positive charged surface and the positively charged R6G molecules. The R6G adsorption efficiency is inhibited by a decrease in pH (pH < 7.6) and enhanced with an increase in pH (pH > 7.6), consequently affecting the overall photocatalytic reaction. In contrast, a decrease in photocatalytic efficiency has been observed, with a pH above 8. Shengyan *et al.* (2017) reported that in a strongly alkaline aqueous solution (pH 11) an onium ion on the R6G structure is transformed into ammonium hydroxide and subsequently R6G is decomposed into an electroneutral molecule. Therefore, the decrease in adsorption leading to a sudden decline in R6G degradation at pH 10 may be attributed to the formation of R6G neutral molecule which impedes dye coulombic attraction towards the negative charge surface of 85%TiO₂-ZnO/BAC1. According to the results, operating at pH 7 and pH 8 had the highest rate constant (k) of 0.0095 min⁻¹ and 0.0126 min⁻¹, respectively (Figure 4-17 b). Based on the economic approach, it is more feasible to operate at pH 7 to avoid the need for pH adjustment using low-cost solar energy. However, it is reasonable to operate at pH 8 when using an external UV source due to the high degradation rate and consequently reduced energy input.

4.2.9.2 Catalyst loading

The effect of the photocatalyst (85%TiO₂-ZnO/BAC1) loading on degrading R6G was evaluated. The solid loading on degrading 50 ppm R6G (pH 7) solution was varied from 0.4 g/L to 1.4 g/L under room temperature. As shown in Figure 4-18 (a) with the increase of catalyst loading from 0.4 g/L to 1.3 g/L, both adsorption and subsequently degradation efficiencies were significantly improved. Under the dark condition, the amount of dye adsorbed onto the photocatalyst increases, thereafter slowing down reaching the state of equilibrium. This phenomenon is attributed to the saturation of the available adsorption open sites. Generally, the colour removal due to adsorption increases with an increase in catalyst loading. Further increase of solid loading (above 1.3 g/L) led to a decrease in photodegradation efficiency. The enhanced degradation efficiency may be due to the increased number of adsorption and active sites on the surface of the catalyst. However, at higher catalyst loading, degradation may be impeded due to the light screening effect and subsequently decreased the number of catalyst active sites (Li *et al.*, 2016).

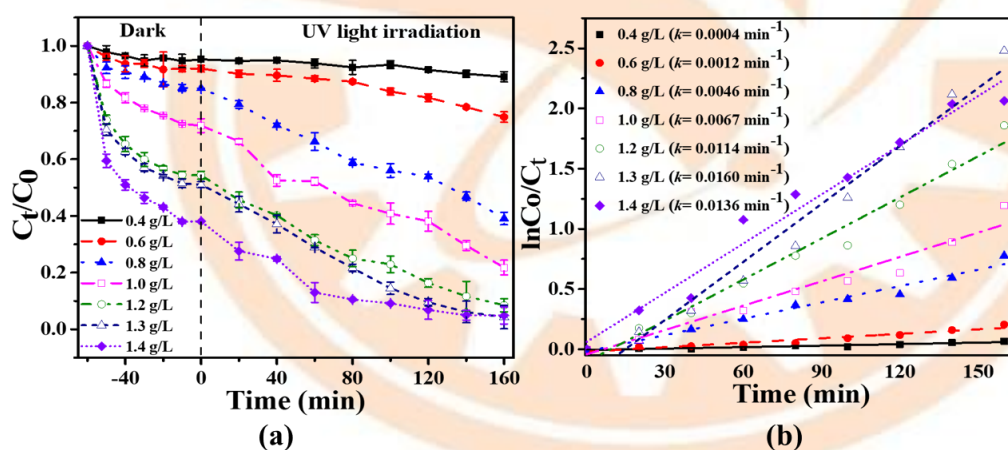


Figure 4-18. (a) Effect of 85%TiO₂-ZnO/BAC1 loading on R6G photodegradation. (b) Degradation kinetics at different photocatalyst loading.

A kinetic study was used to explore the photodegradation rate based on catalyst loading from 0.4 g/L to 1.4 g/L. The apparent rate constant (k) was calculated based on analogous of Equation 34, where the initial concentration (C_0) was the concentration at the point of equilibrium (0 irradiation time). Figure 4-18 (b) shows that, with an increase of catalyst loading from 0.4 g/L to 1.3 g/L, the rate of reaction is increased from 0.004 min^{-1} to 0.0160 min^{-1} . Further increase to 1.4 g/L, apparent rate constant decreased to 0.0136 min^{-1} . High adsorption efficiency of 61.9% showed on 1.4 g/L

compared to 1.3 g/L catalyst loading showing 49.0%. In contrast, 1.3 g/L catalyst loading showed a higher k of 0.0160 min^{-1} than 1.4 g/L catalysts having k of 0.0136 min^{-1} . As mentioned, the decrease in k when increasing the catalyst loading from 1.3 g/L to 1.4 g/L is attributed to the increased light screening effect and subsequently decreased the number of catalyst active sites (Li *et al.*, 2016). According to the results, there is a difference in the apparent rate constant between 1.3 g/L and 1.4 g/L. In the view of economic concern, an optimum catalyst loading of 1.3 g/L is preferred since less energy is required to achieve a higher degradation.

4.2.9.3 Initial concentration

In photodegradation, initial concentration is a key parameter that requires consideration. As mentioned, operating with an excessive initial concentration is likely to impede the degradation due to saturation of the photocatalyst active surface and screening of light for activation (Li *et al.*, 2016). Therefore, the effect of the initial concentration of R6G on the degradation efficiency using 85%TiO₂-ZnO/BAC1 was investigated by varying the concentration from 40 ppm to 70 ppm at constant pH 7. As depicted in Figure 4-19 (a)-(b), the degradation rate was decreased with the increase in the dye initial concentration which harmonizes with the literature (Chiu *et al.*, 2019).

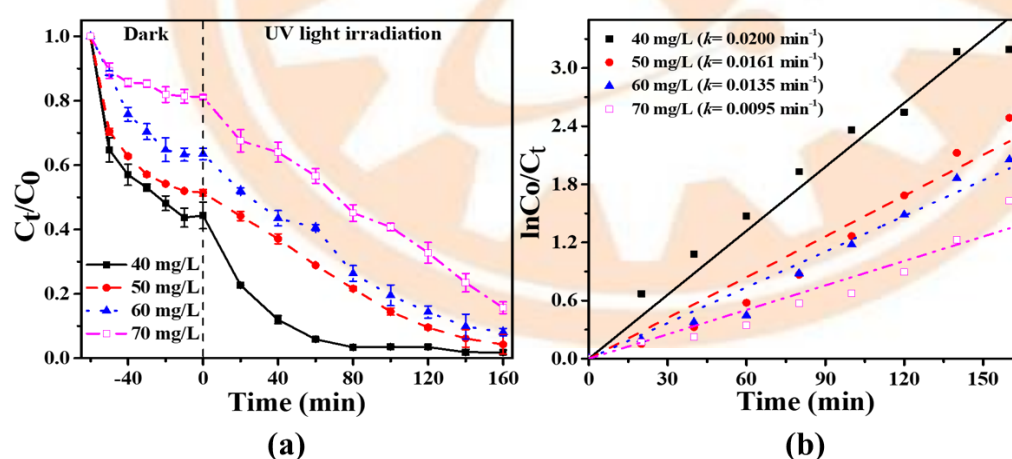


Figure 4-19. (a) Effect of initial concentration on photocatalytic efficiency of 85%TiO₂-ZnO/BAC1. (b) Degradation kinetics at different initial concentrations.

Increased initial concentration results in saturation of catalyst active sites and reduced light penetration onto the surface of the catalyst. At higher concentrations, R6G molecules are likely to compete for the available sites, leading to reduced efficiency of the photodegradation reaction. Moreover, Figure 4-19 (b) confirms the adequacy of the

Langmuir-Hinshelwood model on the photodegradation of R6G dye. The apparent rate constant (k) was found to decrease with an increase in initial concentration which agrees with the model.

4.2.9.4 Temperature

The effect of temperature on photodegradation was carried out in a controlled temperature system. As shown in Figure 4-20 (a)-(b), the temperature was varied from 30°C to 80°C under 70 ppm R6G solution at pH 7, and 1.3 g/L 85%TiO₂-ZnO/BAC1 catalyst loading experimental condition.

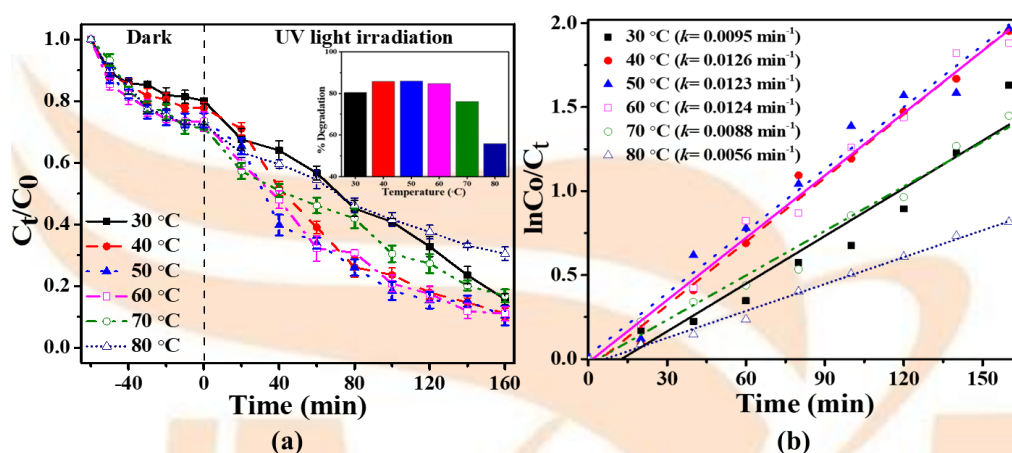


Figure 4-20. (a) Effect of temperature on photocatalytic efficiency of 85%TiO₂-ZnO/BAC1. (b) Degradation kinetics at different temperatures.

When the temperature was increased from 30 °C to 40 °C, the degradation increased slightly from 80.4% to 85.8%. With a further increase from 40 °C to 60 °C, the degradation remained almost constant. However, when the temperature was increased from 60°C to 80°C, the degradation was significantly reduced from 84.7 % to 55.8%, corresponding to a reduced apparent rate constant (k) from 0.0124 min⁻¹ to 0.056 min⁻¹. The reduced percentage of degradation may be attributed to reduced adsorption of the pollutants and the generation rate of active species. At a high temperature of 80 °C, electron-hole recombination and desorption of the adsorbed pollutants are favoured, leading to reduced photocatalytic activity (Chiu *et al.*, 2019). According to the results, operating at ambient temperature is eco-feasible since it requires less energy input to achieve relatively high degradation compared to high temperatures. Additionally, the result can serve as evidence that a temperature controller is required on the solar system due to the thermal effect from the radiation.

In addition, the thermodynamic parameters for the adsorption of R6G dye 85%TiO₂-ZnO/BAC1 were determined to establish the adsorption system. Adsorption experiments were carried out at varying temperatures (303, 313, 323, 333, and 343 K) with 70 ppm initial dye concentration, 7 pH, and 1.3 g/L catalyst loading. The thermodynamic parameters including Gibbs energy change (ΔG), enthalpy (ΔH°), and entropy (ΔS°) were computed according to the thermodynamic equations (36)-(37) reported by Benton *et al.* (2016).

$$\Delta G = -RT \ln K_L \quad (36)$$

$$\ln K_L = \frac{\Delta S^\circ}{R} - \frac{\Delta H^\circ}{RT} \quad (37)$$

Where R is the universal gas constant ($R= 8.314 \text{ J/mol K}$), T is the absolute temperature (K), $K_L = q_e/C_e$. ΔG , ΔH° , and ΔS° is the Gibbs energy change, enthalpy change, and entropy change (kJ/mol), respectively. The plotting $\ln K_L$ against $1/T$ gives a straight-line $y=mx + c$ analogous to equation 37 (Figure 4-21).

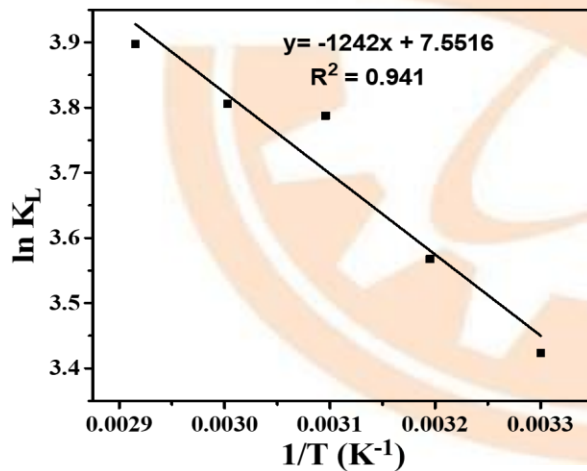


Figure 4-21. A plot of $\ln K_L$ against $1/T$ for 70 ppm R6G dye adsorption by 85%TiO₂-ZnO/BAC1.

The negative values of ΔG (Appendix H) indicate that adsorption of the R6G dye is spontaneous and thermodynamically feasible. From the plot, the computed average standard values of ΔH° and ΔS° is 10.3 kJ/mol and 62.9 kJ/mol, respectively. The positive value of ΔH° confirms the endothermic nature of the adsorption by 85%TiO₂-ZnO/BAC1. Moreover, the calculated ΔH° of 10.3 kJ/mol was found to be less than 40 kJ/mol thus, confirming the possibility of physical adsorption (Foo and Hameed, 2010).

In physical adsorption, an increase in temperature leads to an increase in dye adsorption, thus ruling out the possibility of chemisorption (Figure 4-19). The positive value of ΔS° (62.9 kJ/mol) shows the affinity of banana activated carbon (BAC1) on dye and increased randomness at the solid-solute interface. Similar attribution of the positive value of ΔH° and ΔS° was obtained in the adsorption of rhodamine 6 G (R6G) and methylene blue (MB) using activated carbon (Jarrah, 2017).

4.2.9.5 Stability and reusability

Immobilizing a photocatalyst onto support material is vital based on its stability and recoverability. Supporting a photocatalyst helps the catalyst to be recovered and reused, therefore, reducing the operational costs. The recycling experiments were carried out for 85%TiO₂-ZnO/BAC1 (1.3 g/L) on R6G (50 ppm, pH 7) degradation under 160 min UV irradiation, as shown in Figure 4-22 (a).

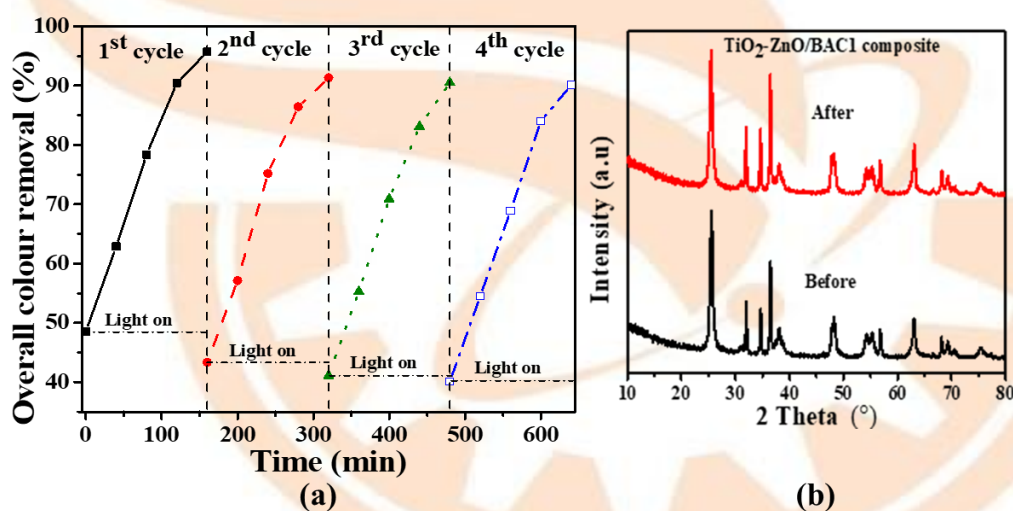


Figure 4-22. (a) Recycling runs in photocatalytic degradation of R6G over 85%TiO₂-ZnO/BAC1 composite. (b) XRD pattern of the composite before and after photocatalytic degradation of R6G dye.

From the results, it was found that colour removal due to adsorption on the 1st and 2nd cycles was different, but from the 2nd to 4th cycles were almost similar. On the first run, the colour removal was 96.1%. However, the overall colour removal was still as high as 90% after four recycling runs, confirming the good stability and reusability of the photocatalyst composite. The slight decrease in colour removal observed maybe be attributed to the loss of photocatalysts and strong attachment of intermediates onto the surface of the photocatalyst. Moreover, no detectable change in nature of the

photocatalyst as confirmed by XRD Figure 4-22 (b) before and after the photocatalytic reaction was observed, indicating good stability in the UV-driven photodegradation reaction.

4.2.9.6 Energy requirement for decolourization and COD reduction.

Any wastewater treatment process must be efficient and economically feasible. Therefore, the efficiency based on the cost of energy required for the UV photo catalysed process was evaluated using electrical energy per order (E_0) given by Equation 38 (Jonidi-Jafari *et al.*, 2015). The experiment was carried out of a volume of 0.08 L, 1.3 g/L 85%TiO₂-ZnO/BAC1 catalyst loading, 50 ppm dye concentration, 1 h adsorption equilibrium time, and 2.4 h irradiation time (6 W UV lamp) experimental condition were.

$$E_0 = \frac{P \times t \times 1000}{V \times \log \left(\frac{C_0}{C_f} \right)} \quad (38)$$

where P is the lamp power (kW), t is the irradiation time (h), V is the volume of wastewater degraded (L). C_0 and C_f represent the initial and final concentration of the dye measured solutions, respectively. Figure 4-23 shows the energy requirement of three dyes (methylene blue, malachite green and rhodamine 6G).

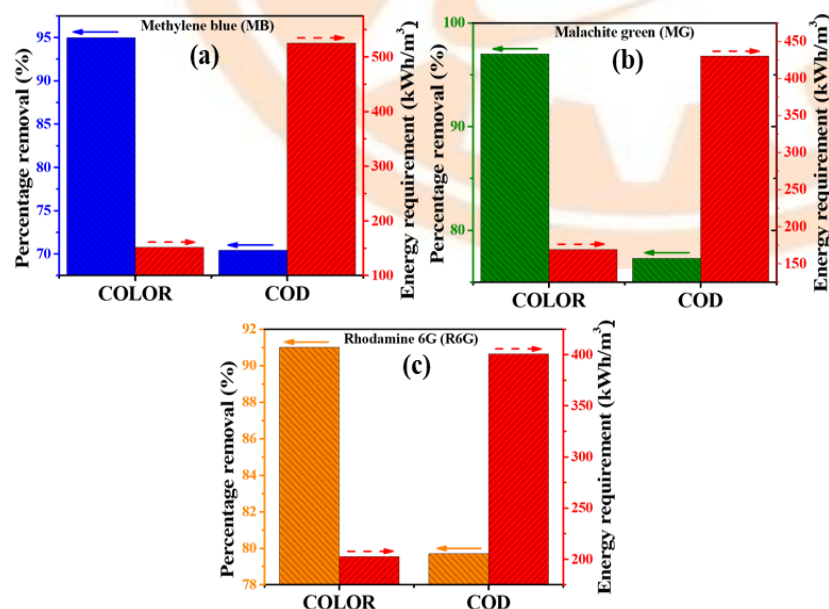


Figure 4-23. Energy requirement for colour removal and COD reduction of the dyes using 85%TiO₂-ZnO/BAC1 at 1.3 g/L catalyst loading, pH 7 and 3.4 h reaction time.

The results show that the energy required for COD reduction of dyes is higher than the energy used for colour removal. The energy required for 95.6% MB, 97.0% MG, and 91.0% R6G colour removal was estimated to be 151.5 kWhm⁻³, 169.2 kWhm⁻³, and 202.7 kWhm⁻³, respectively. In comparison, 525 kWhm⁻³, 430 kWhm⁻³, and 400.8 kWhm⁻³ energy were required for 70.4% MB, 77.3% MG, and 79.7 R6G COD reduction, respectively which is much higher compared to the energy required for colour removal. The high energy required for COD reduction can be attributed to incomplete mineralization and the fact that colour disappearing is the initial step as free radicals first attack chromophores ring structure responsible for colour (Houas *et al.*, 2001; Maria *et al.*, 2017; Rasheed *et al.*, 2017).

4.3 Comparison of various dyes degradation studies

The comparison of 85%TiO₂-ZnO/BAC1 photocatalytic efficiency on the dyes is compared to the work reported by other researchers, summarized in Table 4-6. However, the photodegradation process could be influenced by operation parameters such as type of lamp, light intensity, nature of the photocatalyst (bandgap and particle size), reaction time, catalyst loading, type of substrate, initial substrate concentration, pH, reaction temperature, reactor geometry and hydrodynamic conditions. Therefore, it is difficult to fairly compare the degradation performance.

Table 4-6. Comparison of 85%TiO₂-ZnO/BAC1 photocatalytic efficiency on the dyes with other similar work.

Systems	Initial Concentration (mg/L)	Catalyst Loading (g/L)	Lamp (w)	Irradiation time (min)	Removal efficiency (%)	Ref.
TiO ₂	30 (R6G)	0.3	UV-A	90	92.4	(Lutic <i>et al.</i> , 2012)
ZnO/			9	90	94.3	
Urea						
AC/TiO ₂	50 (R6G)	0.25	Hg	60	85.0	(Sivakumar <i>et al.</i> , 2016)
			125			

TiO₂/ZnO/ Graphene oxide	20 (MB)	0.5	Xe	120	99.6	(Nguyen <i>et al.</i> , 2020)
	20 (RhB)		300	180	99.2	
Bi₂WO₆	10 (MG)	1.0	Xe	30	87.0	(Yijie <i>et al.</i> , 2012)
			500			
TiO₂- ZnO/AC	50 (R6G)	1.3	UV-C	160	91.0	Present
	50 (MB)		6		95.6	study
	50 (MG)				97.0	

4.4 Fluidized bed reactor experiments

Among the photoreactors used in water treatment, a fluidized bed reactor is widely used in wastewater treatment (Gao *et al.*, 2011; Haribabu and Sivasubramanian, 2014; Haroun and Idris, 2009). The application of a photoreactor favouring photocatalytic activity is therefore vital. Therefore, a lab-scale fluidized bed reactor was designed considering geometric conditions favouring the photodegradation process (Rodríguez *et al.*, 2004). Firstly, a hydrodynamics study was conducted to understand the solid distribution, phases, and mass properties. The results obtained from the hydrodynamic study was further used to evaluate the effect of hydrodynamic conditions affecting the photodegradation process.

4.4.1 Hydrodynamics study

Operationally, solid distribution and phase holdups play a key role in the performance of the photoreactor based on mass transfer and ensuring catalyst availability. Thus, solid distribution and phase holdups governed by gas velocities are important parameters to study when carrying out photodegradation in a fluidized bed reactor. The hydrodynamic experiment was carried out to evaluate the effect of superficial fluidization velocity on global gas holdup and solid concentration distribution. Thereafter, this enabled us to understand the homogeneity of the phases in the system favouring the photodegradation process.

4.4.1.1 Gas holdup

The effect of aspect ratio (AR) and inclination angle (IA) on the global gas holdup (ϵ_g) and oxygen mass transfer were determined using 1.3 gL⁻¹ solid loading (Dx50= 320.0 μm (Appendix D), $\rho= 3941 \text{ kgm}^{-3}$). From the results shown in Table 4-7 and Figure 4-24, the ϵ_g increased with an increase in U_g up to 0.024 ms⁻¹ after which it remained nearly constant. At an aspect ratio of 2, the ϵ_g increased significantly from 0.131 to 0.2811 when U_g was increased from 0.009 to 0.024 ms⁻¹. As U_g increases, the number of bubbles tends to increase, therefore increasing the fractional volume occupied by the gas. As shown (Table 4-7), the ϵ_g decreased with an increase in aspect ratio from 2 to 12. Although there was a small decrease in ϵ_g with an increase of aspect ratio beyond 8. This behaviour is as a result of the increased travel distance of the bubbles in the reactor column, a similar phenomenon reported by [Ochieng *et al.* \(2002\)](#). Typically, the longer the bubbles travel distance, the greater opportunity for the bubbles to coalesce. Consequently, this results in bigger bubbles rising faster in the solution to the splash zone ([Ochieng *et al.*, 2002](#)). The increase in aspect ratio means bubbles travel a longer distance which leads to an increase in bubble coalesce and size with shorter residence time in the solution, leading to a decrease in the ϵ_g .

The U_g and ϵ_g share a linear relationship. Not limited to that, there is also a simple linear correlation between U_g and mass transfer coefficient (K_{La}) [Ochieng *et al.* \(2002\)](#). The ϵ_g and K_{La} to U_g separate correlation from this work is depicted in Table 4-7 (Analogous to Equation 26-28). The lower the aspect ratio, the higher the value of n is expected due to minimal bubbles coalesces, a similar observation made by [Haribabu and Sivasubramanian, \(2014\)](#). As shown in Figure 4-24, it is evident that there is an almost a linear relationship observed between ϵ_g and U_g . For an aspect ratio of 2, the highest aspect ratio of 0.2811 at 0.024 ms⁻¹ with an n value of 0.57 was achieved.

Table 4-7. Global gas hold-up and mass transfer correlations.

Aspect	U_g (ms ⁻¹)	ϵ_g	Correlation	K_{La}	Correlation
ratio			(ϵ_g and U_g)	($K_{La}=1.53\epsilon_g$)	(K_{La} and U_g)
2	0.009 - 0.033	0.111 – 0.303	$\epsilon_g = 2.32U_g^{0.57}$	0.169 – 0.463	$K_{La} = 3.55U_g^{0.57}$
4	0.009 - 0.033	0.115 – 0.267	$\epsilon_g = 1.84U_g^{0.55}$	0.175 – 0.408	$K_{La} = 2.82U_g^{0.55}$
6	0.009 - 0.033	0.109 - 0.239	$\epsilon_g = 1.61U_g^{0.54}$	0.166 – 0.365	$K_{La} = 2.46U_g^{0.54}$
8	0.009 - 0.033	0.112 – 0.214	$\epsilon_g = 1.64U_g^{0.56}$	0.171 – 0.327	$K_{La} = 2.50U_g^{0.56}$
10	0.009 - 0.033	0.116 – 0.197	$\epsilon_g = 1.03U_g^{0.47}$	0.177 – 0.301	$K_{La} = 1.58U_g^{0.47}$
12	0.009 - 0.033	0.115 – 0.194	$\epsilon_g = 1.04U_g^{0.47}$	0.175 – 0.296	$K_{La} = 1.59U_g^{0.47}$

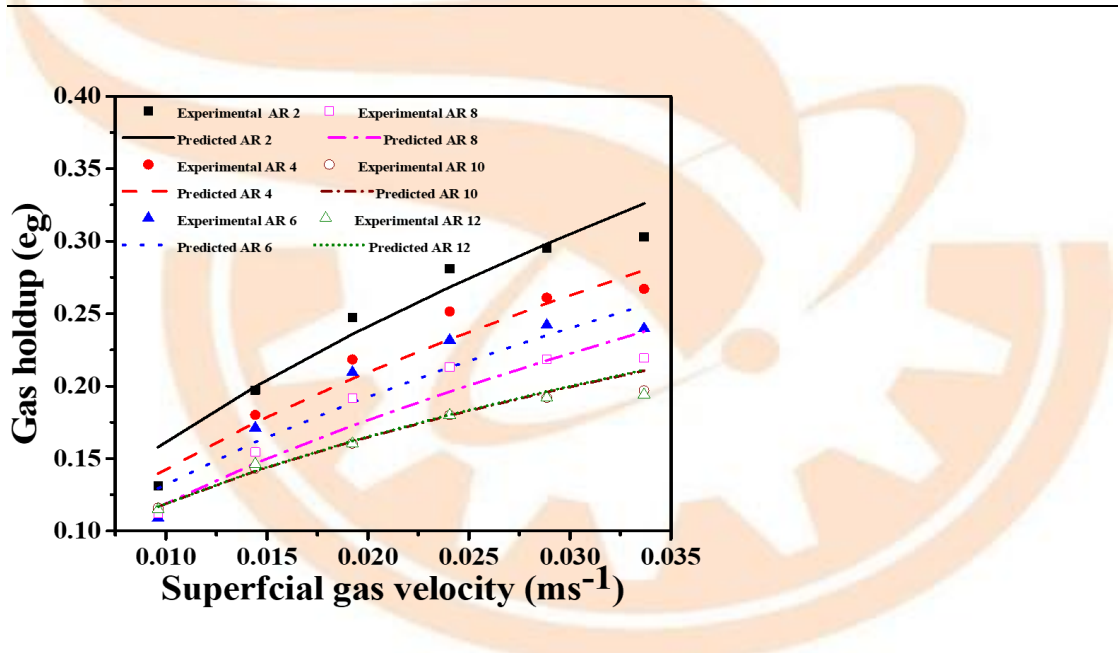


Figure 4-24. The relation between the experimental and predicted global gas holdup at different superficial velocities and aspect ratio (AR).

Moreover, the global gas holdup at different superficial gas velocity range correlations reported in the present work was compared with other studies, summarised in Table 4-8. The gas-holdup values reported by Haribabu and Sivasubramanian, (2014) and Ochieng *et al.* (2003) of 0.290 and 0.300, respectively with a corresponding n value of 0.444 and 0.535, respectively were slightly lower as compared with ϵ_g of 0.303 and n value of 0.578 for the present work. The slight difference may be due to the fact of operating at an almost similar gas velocity range (0.009-0.080 ms⁻¹) but different

particle density. Sur and Mukhopadhyay, (2017) operated at a much lower gas velocity range (0.003-0.004 ms⁻¹) with a particle density of 723 kgm⁻³ and obtained a higher n value of 0.99. This phenomenon is possible due to the fact that operating at low gas velocity and with low particle density, a higher value of n almost near 1 is expected.

Table 4-8. Comparison of gas holdup correlation with other studies.

U_g (ms ⁻¹)	ϵ_g	Correlation	Ref.
0.010-0.003	0.160-0.290	$3.899U_g^{0.444}$	(Haribabu and Sivasubramanian, 2014)
0.010-0.080	0.050-0.300	$0.710U_g^{0.535}$	(Ochieng <i>et al.</i> , 2003)
0.009-0.033	0.111–0.303	$2.320U_g^{0.578}$	Present study
0.003-0.004	0.008-0.011	$0.006U_g^{0.99}$	(Sur and Mukhopadhyay, 2017)

The effect of the reactor inclination angle on ϵ_g and K_{La} under different superficial velocities was evaluated under 1.3 g/L solid loadings and an aspect ratio of 8. In this study, the reactor angle of inclination was varied from 90° - 50° at different gas superficial velocities and the results are presented in Figure 4-25 (a)-(b). According to the results, a general decrease in ϵ_g and K_{La} with the decrease in reactor inclination angle is observed.

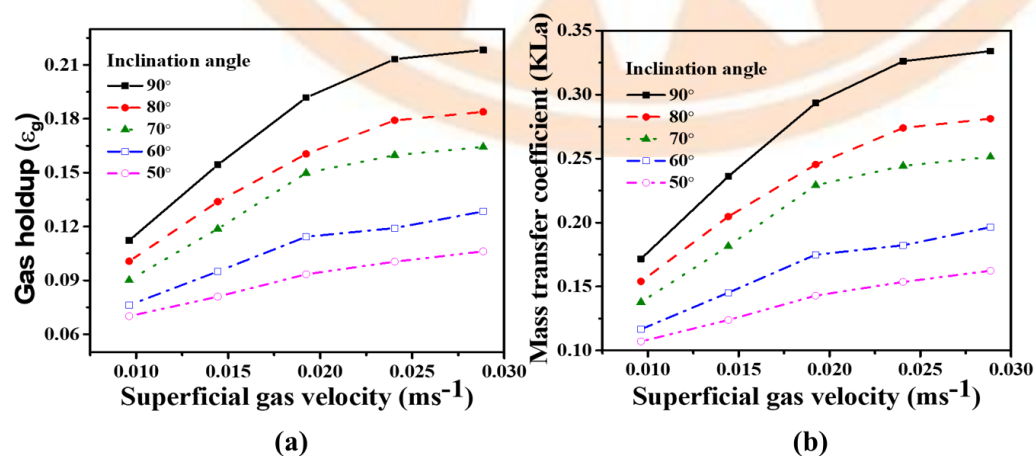


Figure 4-25. Effect of reactor angle inclination on gas holdup (a) and mass transfer (K_{La}) (b) characteristic.

Based on the results obtained, the ϵ_g decreased remarkably with the decrease in reactor inclination, mostly at high gas superficial velocities. With inclining the reactor to 50° from 90° vertical position, the ϵ_g decreases radically to 0.1061 from 0.2183, respectively at a superficial velocity of 0.0288 ms^{-1} . The decrease in ϵ_g is attributed to reduced bubble travel distance and extensively induced bubble coalescence on the upper wall of the reactor, which collectively accounts for gas volume fraction. From the available literature, bigger bubbles have shorter residence times in the solution, consequently reducing the ϵ_g (Ochieng *et al.*, 2002). It is evident from the results that the reactor inclination angle from 90° to 50° significantly affect the ϵ_g and K_{La} . A similar observation was made by Ugwu and Ogbonna (2002) who reported a decrease in ϵ_g and K_{La} from 0.022 and 0.188, respectively to 0.0158 and 0.105 when the column is inclined from 45° to 8° , horizontal surface marked as 0° .

4.4.1.2 Estimation of solid concentration axial distribution.

The effect of the solid loading on the solid concentration axial distribution profile was evaluated at different gas superficial velocities from 0.00962 ms^{-1} to 0.02405 ms^{-1} and 90° inclined reactor (vertical position). Figure 4-26 (a)-(d) shows a general dispersion of solids is increased while increasing the solid loading at the same U_g . The concentration of solids at the bottom also increases with an increase in solid loading. For low and high gas velocities under varied solid loading, the solid particles are highly concentrated at the bottom of the column thus, uneven dispersion of particles. The solid particles used tend to concentrate at the bottom of the bed as compared to the lean bed region since they are not sensitive to the gas superficial velocity range used. Moreover, an increase in solid loading resulted in a steeper concentration profile from 5 cm and 15 cm of the gas distributor. This can be explained by the high tendency of less concentrated particles carryover by the wake. As a result, less concentrated particles loading is slightly distributed compared to high concentrated particles loading.

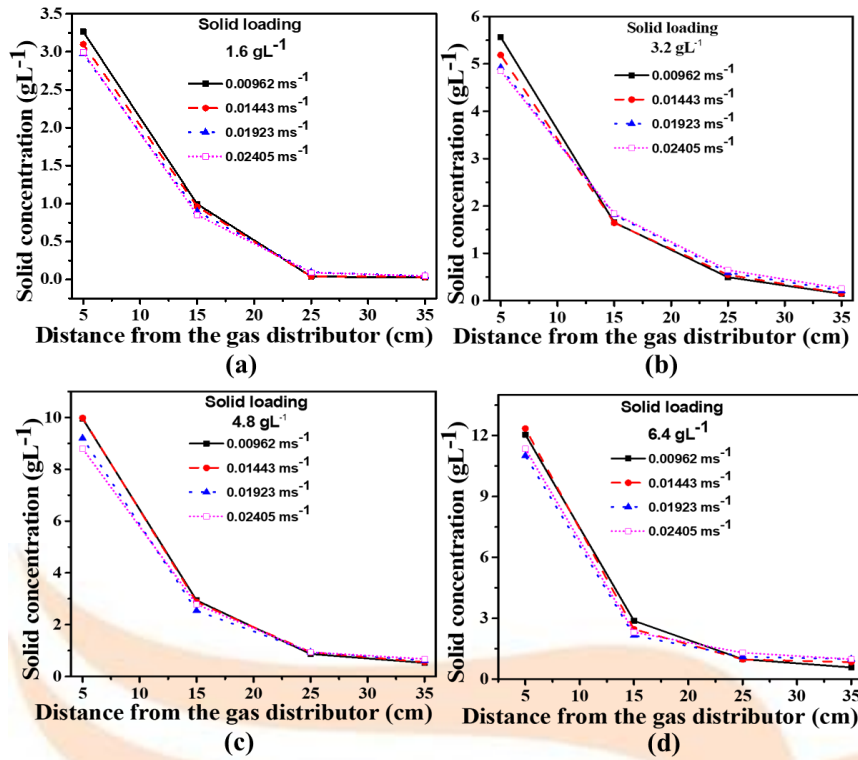


Figure 4-26. Particle distribution profile on solid loading at different gas superficial velocities.

A further experiment was carried out to evaluate the effect of reactor inclination angle from 90° – 50° on the solid concentration distribution profile under different superficial gas velocities. In this experiment, a constant solid loading of 4.8 gL^{-1} and the results are shown in Figure 4-27 (a)-(e).

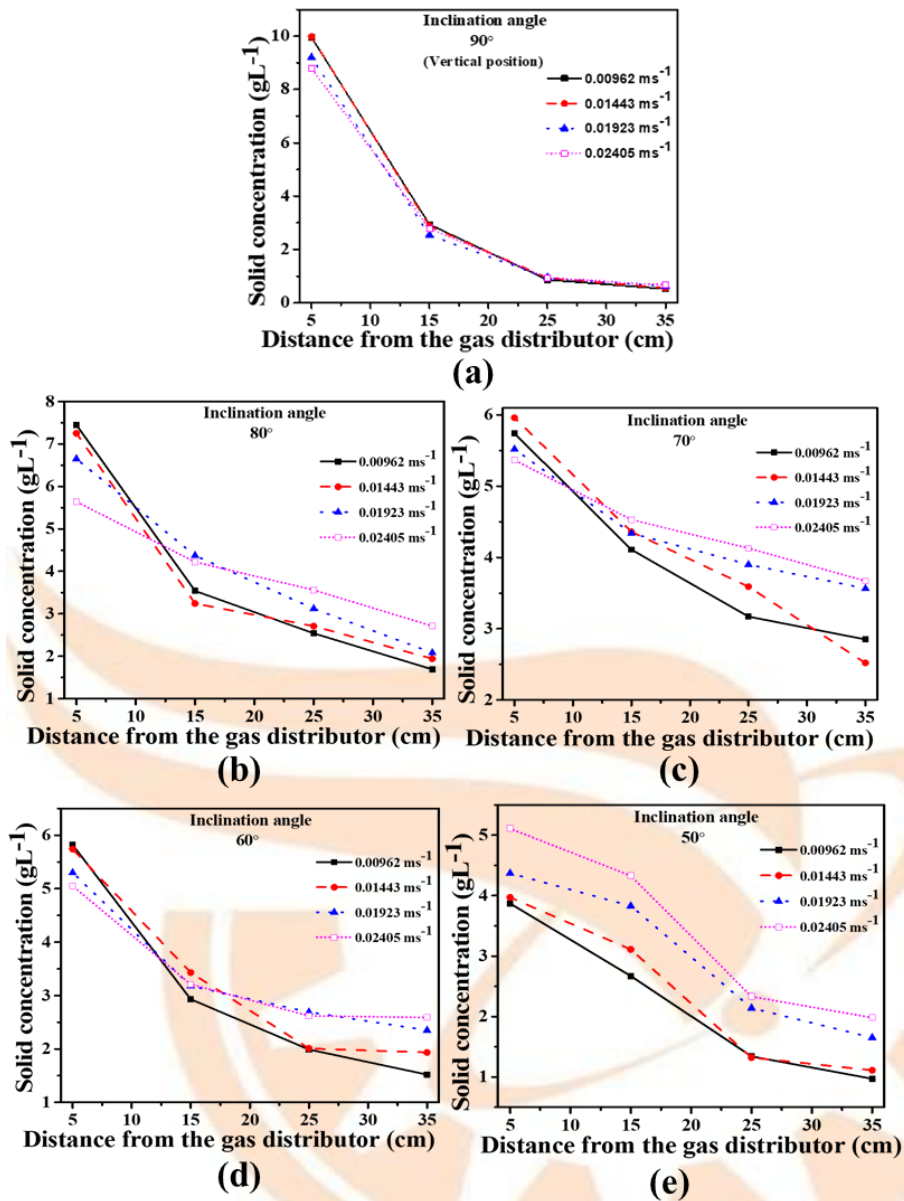


Figure 4-27. Effect of inclination angle on particle distribution at different superficial gas velocities.

The curves in Figure 4-27 (a)-(e) show a general decrease in axial solid concentration from the gas distributor to the splash zone. For instance, in 90° inclination angle at 0.009 to 0.024 ms⁻¹ (Figure 4-27 a), a sudden drop of not less than 70% solid concentration between 5 cm and 15 cm from the gas distributor, followed by a gradual decrease in solid concentration beyond 15 cm was observed in both low and high gas velocity. Furthermore, reducing the inclination angle below 90° to 50° resulted in a less steep solid concentration profile at different superficial gas velocities, confirming an improvement in solid concentration along the reactor column. For inclination angles

below 90° to 50°, it was found that the solid concentration profile along the column is greatly dependent on the superficial gas velocity. Therefore, different solid concentration patterns were identified at different inclination angles and gas superficial velocities.

Moreover, a good solid concentration profile along the column was found to be at 70 ° of the reactor inclination angle (Figure 4-27 c). In contrast, when the reactor inclination angle was reduced to 60°, the relatively uniform solid distribution profile began to reduce. The reduction is a result of an increase in solid concentration along the lower side of the inclined column. For the inclination angle at 50°, the solid distribution is greatly reduced since most of the solids happen to crawl occupying the lower side of the inclined column. As observed, this can be explained by an increase in air bubbles occupying the upper surface of the inclined reactor, resulting in a low-density region. Thus, the fluid in this low-density transport the particles in their wake. Concurrently, the space at bottom of the reactor created by the upward moving liquid-solid phase is therefore filled by the liquid-solid phase from the splash zone along the lower inclined reactor to the low-dense region. The down moving liquid transports back the particles to the low density and is moved back again by upward moving fluid wakes, creating an upwards and downwards circulation stream. A proposed flow regime (Figure 4-28) illustrates how the solid concentration distribution, and the fluid circulation imitates the airlift reactor fluid circulation regime. The low dense (ascending flow) region and high dense (descending flow) region are separated by an imaginary line (non-physical boundary).

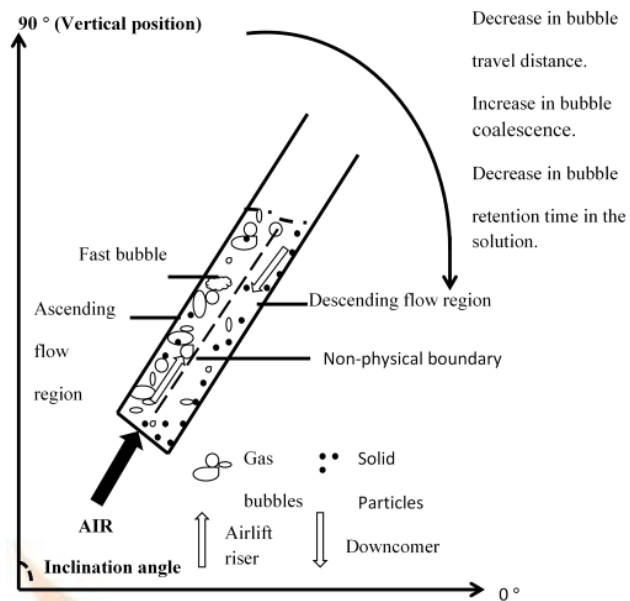


Figure 4-28. Model of flow scheme in an inclined column.

From the literature, the airlifts reactor is operated with entrained or free gas in the downcomer while the riser is sparged with a gas (Chisti and Moo-Young, 1993). This operation condition induces the gas holdup difference between the riser and downcomer region, hence, inducing the fluid circulation and particle carryover. Compared to the present work, the upper and the lower side of the inclined reactor surface acted as risers and downcomer, respectively.

4.4.1.3 Optimum hydrodynamic conditions.

From the preliminary study, the optimum hydrodynamic condition was determined based on gas holdup and particle distribution. According to the hydrodynamic results, the 90° showed higher gas holdup but poor solid distribution along the column compared to other inclination angles referenced in Figures 4-24 and 4-27. Moreover, the 70° inclined reactor showed a better solid distribution compared to other inclined angles studied. Furthermore, the 70° inclined reactor showed a better solid distribution profile but with a slightly lower gas hold of 0.1498 at 0.01923 ms⁻¹ compared to the gas holdup of 0.1597 obtained at a superficial gas velocity of 0.0288 ms⁻¹. Although high gas velocity ensures enhanced mass transfer by increased gas holdup, however, this may result in increased energy consumption. Therefore, based on economic concern and good fluidization, an inclined reactor at 70° and 0.024 ms⁻¹ gas superficial velocity is considered to be the optimum hydrodynamic condition.

4.4.2 Effect of hydrodynamic parameters on photodegradation

A high homogeneity of the phases and solid distribution attributed to high solid-liquid, liquid-gas mass transfer and catalyst availability to utilize UV light is essential to achieve high photodegradation efficiency (Ray, 1998). To achieve efficient photodegradation, high mass transfer of the substrate in the liquid phase to the activated catalyst surface and maximum catalyst surface activation by photon has to occur. Moreover, dissolved oxygen from air plays an important role in prolonging electron-hole recombination resulting in enhanced photocatalytic efficiency (Dong *et al.*, 2015). Therefore, the liquid-solid, gas-liquid mass transfer and catalyst availability is considered important to achieve an efficient photodegradation activity. The mass transfer, catalyst availability and light utilization depend on the solid distribution and the local gas holdup which is governed by gas superficial velocity. In the preliminary study of hydrodynamics, it is confirmed that the inclination angle of the reactor and superficial gas velocity affect the solid distribution and global gas holdup. Therefore, it is of interest to delve into reactor inclination angle and superficial gas velocity parameters affecting the solid distribution and global gas holdup which can influence the photocatalytic activity.

4.4.2.1 Reactor inclination angle

The photocatalytic efficiency of 85%TiO₂-ZnO/BAC1 on R6G was carried under the constant experimental condition of 1.3 g/L catalyst loading, 185 mL of 70 ppm concentration, pH 7, 0.019 ms⁻¹ U_g, but varied reactor inclination angle from 90° (vertical position) to 60°. From the results (Figure 4-29), the colour removal due to adsorption slightly increased when the reactor was changed from 90° to 60°.

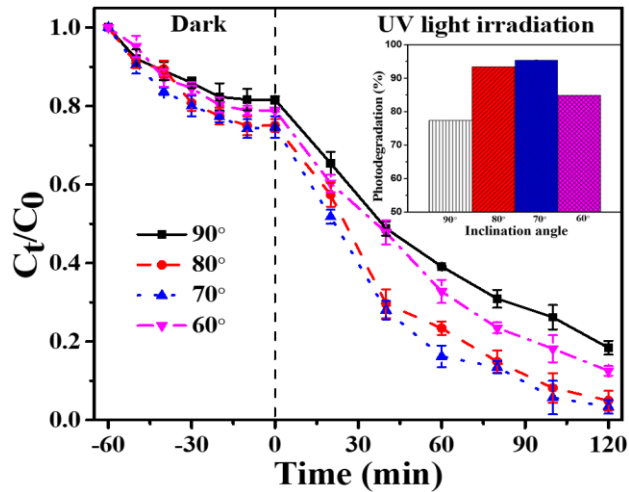


Figure 4-29. Effect of reactor inclination angle on photocatalytic efficiency.

Moreover, a high colour removal of 95.4% due to photodegradation was achieved at 70° compared with an 80° inclination angle having a relatively low colour removal of 93.4%. Whereas, in 90° and 60° inclination angles a much lower colour removal of 84.8% and 77.4%, respectively were achieved inset Figure 4-29. This phenomenon can be explained based on the solid distribution profile shown in Figure 4-27. According to the results, it was observed that an inclined angle of 90° showed a steep concentration distribution profile along the column. Further inclining the reactor to 70°, an improved solid concentration distribution profile was achieved but then lowered when the reactor was inclined to 60° from 70°. At a 90° inclination angle, most of the catalysts are concentrated at the bottom while few catalysts are at the top of the reactor thus reducing utilization of UV irradiation from the lamps, resulting in a low photodegradation process. Similarly, a relatively low colour removal due to photodegradation at an inclination angle of 60° was observed. The low colour removal is attributed to the minimal utilization of UV lamps placed on the upper side compared to the lower side of the inclined reactor since the catalysts are mostly on the lower side as observed in this study. Incidentally, catalysts concentrated at the lower side may pose a light scattering and screening effect to each other leading to reduced photocatalytic efficiency. The hypothesis was evaluated by an experiment placing the UV lamp either on the upper or lower side of the 60° inclined reactor and keeping other conditions constant and the result is shown in Figure 4-30.

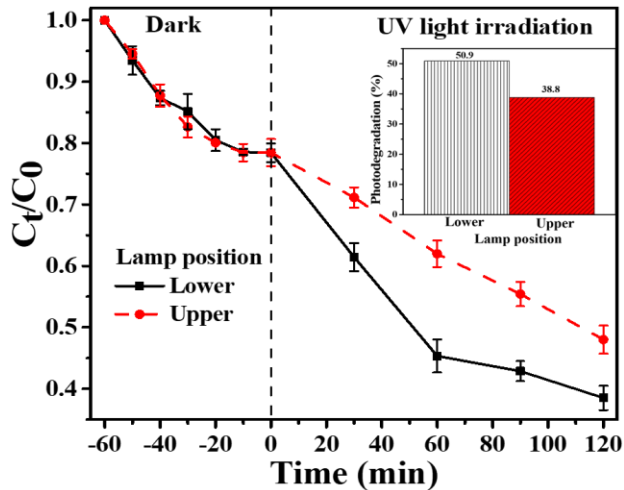


Figure 4-30. Effect of lamp position on photocatalytic efficiency.

A higher colour removal of 50.9% due to photodegradation is achieved when the lamp is placed lower compared to the upper side of the inclined reactor having 38.8% colour removal. Due to the considerable high concentration of catalysts on the lower inclined reactor wall, the catalysts are more activated by the lower lamp compared to the upper lamp where catalysts are less concentrated. Reactor inclined at 90° and 60° photocatalytic efficiencies are impeded due to the inefficiency to fully utilize UV irradiation from the lamps. Moreover, despite high gas holdup observed when the reactor is inclined at 90° and 80° (Figure 4-25), the reactor inclined at 70° with low gas holdup still had higher photocatalytic efficiency. This confirms that solid distribution is a significant limiting factor for photodegradation compared to gas holdup.

4.4.2.2 Superficial gas velocity

A high fluidization velocity consequently increases power consumption. Therefore, it is vital to keep the fluidization velocity as low as possible but high enough to suspend the catalysts and increase gas holdup for maximum utilization of photons and improved mass transfer. It was of interest to investigate the effect of superficial gas velocity on photocatalytic efficiency at different gas velocities. The study was conducted using 1.3 g/L catalyst loading, 70 ppm R6G dye concentration, pH 7, 70° inclination angle, and at varied U_g from 0 to 0.02405 ms^{-1} . As presented in Figure 4-31, the adsorption and photodegradation increased when the U_g was increased from 0 to 0.01923 ms^{-1} , followed by a slight increase when increased to 0.02405 ms^{-1} . At 0 ms^{-1} U_g , colour removal due to adsorption was low. This is due to a high concentration of catalyst at the bottom of the gas diffuser which resulted in a poor mass transfer of aqueous

pollutants across the axial region. Upon UV irradiation, a relatively low photodegradation was achieved. The degradation of the dye only occurred by a few suspended catalysts which are less dense than water and direct photolysis.

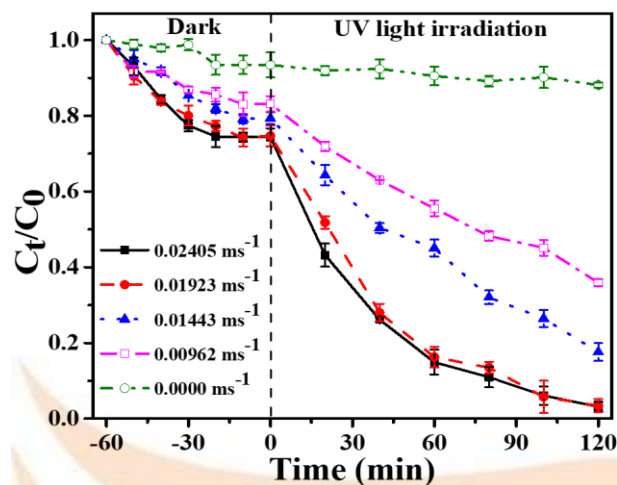


Figure 4-31. Effect of superficial gas velocity on photocatalytic efficiency.

At $0.00923 \text{ ms}^{-1} U_g$, some catalysts were suspended thus, increasing pollutants mass transfer and catalyst activation leading to improved photocatalytic efficiency. Similarly, an increase to 0.01443 ms^{-1} and further to optimum 0.01923 ms^{-1} resulted in further enhanced photocatalytic efficiency. At 0.01923 ms^{-1} , the superficial gas velocity is high enough to suspend most of the catalyst, therefore, ensuring maximum catalyst availability toward the light and mass transfer. Beyond 0.01923 ms^{-1} resulted in improved particle distribution and increased gas holdup, but a slightly increased photocatalytic activity was observed. The trend of the result agrees with the previous work reported by [Matsumura et al. \(2007\)](#), using a reactor equipped with a draft tube. It was found that degradation of cresol increased with an increase in superficial gas velocity up to a certain point (optimum) where no further degradation rate was observed. However, 0.006 ms^{-1} was found to be the optimum U_g which is much lower compared to 0.019 ms^{-1} for the present work. This was achieved since they used less dense particles of 570 kgm^{-3} compared to the 3941 kgm^{-3} used in the present study. In consideration of an economic point of view, operating at a low superficial high enough to ensure high photocatalytic efficiency is considered feasible. Therefore, operating under 0.019 ms^{-1} would be preferred as optimum as less energy would be required for maximum degradation.

CHAPTER 5

5 CONCLUSION AND RECOMMENDATIONS

5.1 Conclusion

Based on the series of experiments conducted, it can be confirmed that the hybrid supported on activated carbon from banana peels ($\text{TiO}_2\text{-ZnO/BAC}$) showed multi-promising characteristics feasible for the treatment of textile wastewater. TiO_2 surface was modified using ZnO and banana peel activated carbon to form $\text{TiO}_2\text{-ZnO/BAC}$ composite. The physicochemical properties of the prepared materials were characterized using X-ray diffractometer (XRD), Fourier transform infrared (FTIR), Scanning electron microscopy (SEM), Photoluminescence (PL), Thermal gravimetric analysis (TGA), Brunauer-Emmett-Teller (BET) and Laser diffraction techniques. The degradation performance of the catalysts was tested on dye model(s) based on colour removal and COD reduction under UV light. Moreover, the effect of photocatalytic operation parameters and kinetics were also studied in a lab-scale stirred tank reactor system (STR). Furthermore, the scavenging experiment was conducted to further understand the degradation mechanism of the dye. A fluidized bed reactor (FRB) system was fabricated and used to understand the effect hydrodynamic of photodegradation efficiency. Therefore, the experimental data and information produced from three-phase FBR can be used for practical application. The following conclusions from the present can be made as summarized:

- i. The pure TiO_2 , ZnO and their Hybrid were successfully prepared using sol-gel, precipitation, and physical mixing, respectively. Activated carbon from the banana peel (BAC) using different impregnation ratios (char: KOH of 1:1, 1:2, and 1:3) was effectively prepared at 700°C for 1 hr (heating rate: 10°C per min) under a nitrogen atmosphere. Using colloidal silica (30% binding loading to water) as a binder, activated carbon (BAC) was uniformly dispersed on $\text{TiO}_2\text{-ZnO}$ to form a composite ($\text{TiO}_2\text{-ZnO/BAC}$).
- ii. The XRD analysis showed defined phases for tetragonal anatase and hexagonal wurtzite for pure TiO_2 and ZnO. Similarly, $\text{TiO}_2\text{-ZnO}$ showed the existence of defined phases for tetragonal anatase and hexagonal wurtzite confirming the successful hybridization of the pure catalyst (TiO_2

and ZnO). The commercial AC and BAC showed only two broad diffractions at 2θ 23.5° and 43° with an absence of a sharp peak revealing a predominantly amorphous structure, typically characteristic of activated carbon.

- iii. FTIR spectra of TiO₂ and ZnO showed an adsorption peak at around 500 cm⁻¹ and 680 cm⁻¹ Zn-O and Ti-O stretching, respectively. With the introduction of BAC support on TiO₂-ZnO, the peak width at around 1079 cm⁻¹ assigned to C-N which correspond to the peak observed on BAC became broad. The broadening of the peak at 1079 cm⁻¹, successfully confirms the incorporation of BAC onto the TiO₂-ZnO hybrid.
- iv. SEM micrographs for char obtained from banana peel via carbonization showed the existence of a small pore cavity on the char surface. With an increased KOH activation ratio, surface roughness and structural defect on the pores also increased, resulting in high surface area but to a certain extent. SEM micrographs of TiO₂ and ZnO showed almost uniform spherical shape particles with a degree of homogeneity. For the TiO₂-ZnO micrograph, a plausible high tendency of agglomeration was observed, confirming successful hybridization. For TiO₂-ZnO/BAC micrograph, undefined morphology was observed but with good adherence of the compositions thus, signifying the good binding property of inert colloidal silica used.
- v. On immobilization of ZnO onto TiO₂, the energy bandgap of TiO₂ changed from 3.2 eV to 3.1 eV thus, revealing the formation heterojunction posing a synergistic effect and subsequently enhanced photocatalytic activity. PL analysis showed that the combination of TiO₂ with ZnO greatly decreased the resultant PL intensity which is attributed to reduced electron-hole recombination. Thus, resulting in a high quantum yield of excitons and enhanced photocatalytic activity. Incidentally, with the introduction of BAC1 to TiO₂-ZnO hybrid, a further reduced PL intensity was observed. Hence, revealing doubly prolonged recombination results in higher photocatalytic activity.
- vi. TGA analysis showed an improved TiO₂-ZnO thermal stability due to thermal stable ZnO. However, TiO₂-ZnO/BAC composite showed a significantly sudden mass loss due to BAC introduction which is thermally unstable.

- vii. The prepared support material (BAC1), activated at a KOH impregnation ratio of 1:1 showed a higher adsorption efficiency on the R6G dye model compared to banana peel activated carbon at 1:2 and 1:3. Thus, the BAC1 (1:1) was used as a support material for the superior hybrid. On hybridization of TiO₂ and ZnO, the hybrids with 80%, 85%, and 95% of TiO₂ composition showed higher photocatalytic activity corresponding to 95.7%, 97.9%, and 94.8% colour reduction, respectively, as compared to pure TiO₂ and ZnO, which showed 85.3% and 39.5%, respectively. Superior hybrid (85% TiO₂ composition) with the highest photocatalytic efficiency of 97.9% was further supported using the optimized banana activated carbon (BAC1). With the introduction of BAC1 on superior hybrid, the composite showed an increase in degradation efficiency with an increase in BAC1 composition up to 40%. Beyond 40% BAC1 composition, the degradation suddenly began to decrease but adsorption continues to increase, showing the predominance of adsorption over the photodegradation process. The increase in colour removal due to adsorption is not feasible as pollutants are not fully degraded but transferred from one phase to another resulting in secondary pollution. Therefore, the hybrid composite with 40% BAC1 composition as the optimum was used in subsequent experiments.
- viii. The photocatalytic efficiency of 85%TiO₂-ZnO/BAC1 for the colour removal of R6G, MB, and MG was 91.0%, 95.6%, and 97.0%, respectively. However, the COD reduction on R6G, MB, and MG was 79.7%, 70.4%, and 77.3%, respectively lower than colour reduction. Therefore, the catalyst proved to be more effective in the treatment of organic dyes especially on colour removal. UV photodegradation was found to be more effective on colour removal compared to COD reduction. Incidentally, COD reduction required more energy for complete mineralization. From the reusability test, the overall colour removal was still as high as 90% after four recycling runs, confirming the good stability and reusability of the 85%TiO₂-ZnO/BAC1 composite.
- ix. For optimum hydrodynamic conditions based on gas hold and solid distribution, the 90° reactor vertical position showed a higher gas holdup but steep solid distribution as most of the solids concentrated near the gas distributor. Compared to 90°, the 80° inclined reactor showed slight

improved solid distribution but with a drop in gas holdup. At 50° inclination angle, a good axial solid distribution with high solid settling on the lower side of the inclined reactor and poor gas holdup was observed. Apart from good solid distribution, the reactor inclined at 70° had low solid settling and high gas holdup compared to the 60° inclination angle. Therefore, 70° inclination angle and 0.019 ms⁻¹ superficial gas velocity was chosen to be the optimum condition for photodegradation. Under 70° inclination angle, photodegradation increased when the U_g was increased from 0 to 0.01923 ms⁻¹, followed by a slight increase when increased to 0.02405 ms⁻¹. This signifies that 0.01923 ms⁻¹ superficial gas velocity is high enough to suspend most of the catalyst, ensuring maximum catalyst availability to light irradiation and facilitating the mass transfer. Therefore, chosen to be the superficial gas velocity for high photodegradation efficiency with respect to power input.

5.2 Recommendation

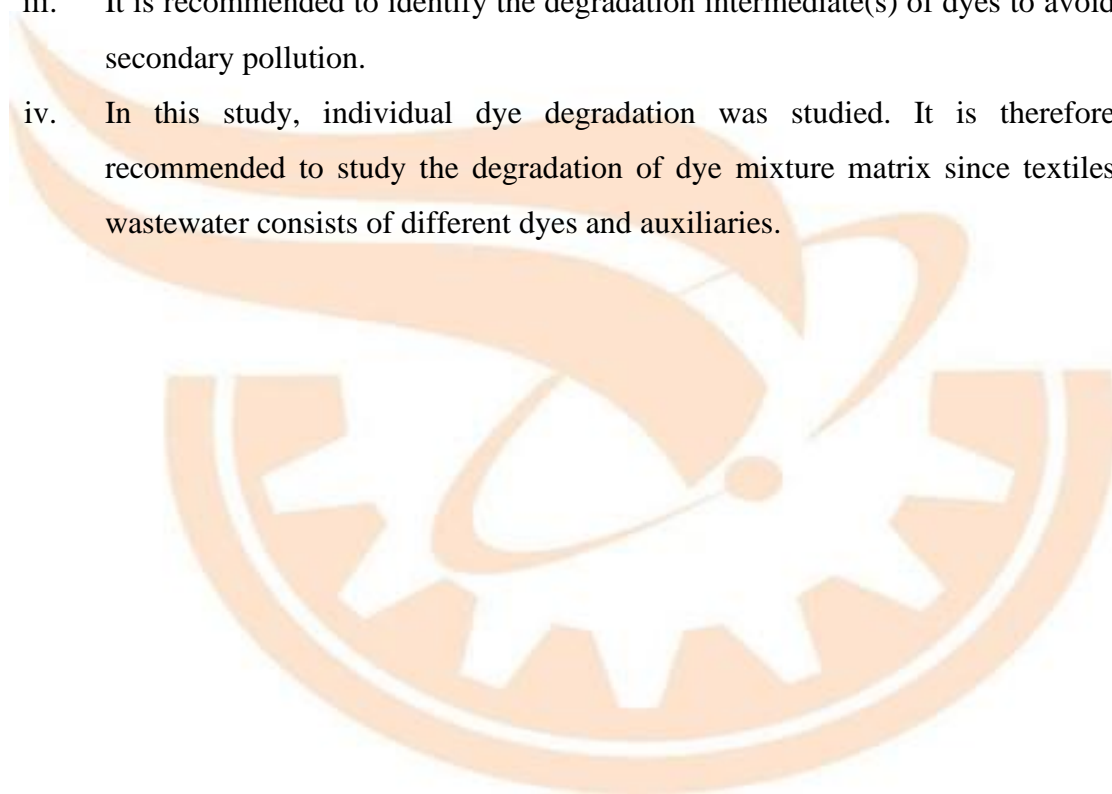
5.2.1 Engineering significance and recommendation

Over the years emerging contaminants (EC) have led to widespread recalcitrant compounds which eventually end up in water bodies. The main example of EC is synthetic dyes, known to pose high biochemical oxygen demand, chemical oxygen demand, and dense colour resulting in several ecotoxicological effects and limitations to water benefits. Therefore, the use of low-cost photocatalyst supported onto AC from the banana peel (agricultural waste) is a feasible promising way of improving water quality. Typically, a wastewater treatment plant involves a series of stages including preliminary, primary, secondary, and tertiary. However, the biological method in secondary is considered ineffective for recalcitrant compounds. Moreover, in the tertiary stage, the adsorption method is known to remove a wide range of dyes but only transfer pollutants from one phase to another leading to secondary pollution. Therefore, the use of supported photocatalyst (photodegradation) is considered a better effective way of degrading a wide range of recalcitrant compounds. Apart from favouring photocatalytic activity, the use of agricultural waste as a source of support material offers economical and agricultural waste management advantages. The use of

supported photocatalyst eliminates separation post-treatment and significantly reduces the cost in the tertiary process.

5.2.2 Recommendation for future work

- i. In this study, only one catalyst size was used throughout the experiments conducted. However, it is recommended that different particles size should be studied since photocatalytic activity and solid distribution in FBR is influenced by catalyst size.
- ii. Solar energy to activate the catalyst should be explored since this will further reduce the cost of operation based on energy input.
- iii. It is recommended to identify the degradation intermediate(s) of dyes to avoid secondary pollution.
- iv. In this study, individual dye degradation was studied. It is therefore recommended to study the degradation of dye mixture matrix since textiles wastewater consists of different dyes and auxiliaries.



REFERENCE

- Al-degs, Y. S., El-barghouthi, M. I., El-sheikh, A. H., & Walker, G. M. (2008). Effect of solution pH, ionic strength, and temperature on adsorption behaviour of reactive dyes on activated carbon. *77*, 16–23. <https://doi.org/10.1016/j.dyepig.2007.03.001>
- Asiri, A. M., Al-Amoudi, M. S., Al-Talhi, T. A., & Al-Talhi, A. D. (2011). Photodegradation of Rhodamine 6G and phenol red by nanosized TiO₂ under solar irradiation. *Journal of Saudi Chemical Society*, *15*(2), 121–128. <https://doi.org/10.1016/j.jscs.2010.06.005>
- Babuponnusami, A., & Muthukumar, K. (2014). A review on Fenton and improvements to the Fenton process for wastewater treatment. *Journal of Environmental Chemical Engineering*, *2*(1), 557–572. <https://doi.org/10.1016/j.jece.2013.10.011>
- Bai, N., Liu, X., Li, Z., Ke, X., Zhang, K., & Wu, Q. (2021). High-efficiency TiO₂/ZnO nanocomposites photocatalysts by sol-gel and hydrothermal methods. *Journal of Sol-Gel Science and Technology*. <https://doi.org/10.1007/s10971-021-05552-8>
- Balmer, M. E., Buser, H. R., Müller, M. D., & Poiger, T. (2005). Occurrence of some organic UV filters in wastewater, in surface waters, and in fish from Swiss lakes. *Environmental Science and Technology*, *39*(4), 953–962. <https://doi.org/10.1021/es040055r>
- Banerjee, S., Pillai, S. C., Falaras, P., O'shea, K. E., Byrne, J. A., & Dionysiou, D. D. (2014). New insights into the mechanism of visible light photocatalysis. *Journal of Physical Chemistry Letters*, *5*(15), 2543–2554. <https://doi.org/10.1021/jz501030x>
- Bedoux, G., Roig, B., Thomas, O., Dupont, V., & Le Bot, B. (2012). Occurrence and toxicity of antimicrobial triclosan and by-products in the environment. *Environmental Science and Pollution Research*, *19*(4), 1044–1065. <https://doi.org/10.1007/s11356-011-0632-z>
- Behnajady, M. A., Eskandarloo, H., Modirshahla, N., & Shokri, M. (2011). Investigation of the effect of sol-gel synthesis variables on structural and photocatalytic properties of TiO₂ nanoparticles. *Desalination*, *278*(1–3), 10–17. <https://doi.org/10.1016/j.desal.2011.04.019>
- Benton, O., Apollo, S., Naidoo, B., & Ochieng, A. (2016). Photodegradation of Molasses Wastewater Using TiO₂-ZnO Nanohybrid Photocatalyst Supported on Activated Carbon. *Chemical Engineering Communications*, *203*(11), 1443–1454. <https://doi.org/10.1080/00986445.2016.1201659>
- Bouaifi, M., Hebrard, G., Bastoul, D., & Roustan, M. (2001). A comparative study of gas hold-up, bubble size, interfacial area and mass transfer coefficients in stirred gas-liquid reactors and bubble columns. *Chemical Engineering and Processing*, *40*(2), 97–111. [https://doi.org/10.1016/S0255-2701\(00\)00129-X](https://doi.org/10.1016/S0255-2701(00)00129-X)
- Brigden, K., Hetherington, S., Wang, M., Santillo, D., & Johnston, P. (2013). Hazardous chemicals in branded textile products on sale in 25 countries/regions during 2013. *Greenpeace Research Laboratories Technical Report 06/2013, December*, 47.

- Caldwell, J. C. (2012). DEHP: Genotoxicity and potential carcinogenic mechanisms-A review. *Mutation Research - Reviews in Mutation Research*, 751(2), 82–157. <https://doi.org/10.1016/j.mrrev.2012.03.001>
- Carmen, Z., & Daniel, S. (2012). Textile Organic Dyes – Characteristics, Polluting Effects and Separation/Elimination Procedures from Industrial Effluents – A Critical Overview. *Organic Pollutants Ten Years After the Stockholm Convention - Environmental and Analytical Update*, 142, 0–1. <https://doi.org/10.5772/32373>
- Carp, O. (2004). Photoinduced reactivity of titanium dioxide. *Progress in Solid State Chemistry*, 32(1–2), 33–177. <https://doi.org/10.1016/j.progsolidstchem.2004.08.001>
- Carr, K. (1995). Reactive dyes, especially bioactive molecules: structure and synthesis. *Modern Colorants: Synthesis and Structure*, 87–122. https://doi.org/10.1007/978-94-011-1356-4_4
- Castañeda-Juárez, M., Martínez-Miranda, V., Almazán-Sánchez, P. T., Linares-Hernández, I., Santoyo-Tepole, F., & Vázquez-Mejía, G. (2019). Synthesis of TiO₂ catalysts doped with Cu, Fe, and Fe/Cu supported on clinoptilolite zeolite by an electrochemical-thermal method for the degradation of diclofenac by heterogeneous photocatalysis. *Journal of Photochemistry and Photobiology A: Chemistry*, 380(October 2018), 111834. <https://doi.org/10.1016/j.jphotochem.2019.04.045>
- Chen, Yijie, Zhang, Y., Liu, C., Lu, A., & Zhang, W. (2012). Photodegradation of malachite green by nanostructured Bi₂WO₆ visible-light-induced photocatalyst. *International Journal of Photoenergy*, 2012. <https://doi.org/10.1155/2012/510158>
- Chen, You hua, Wen, X. wei, Wang, B., & Nie, P. yan. (2017). Agricultural pollution and regulation: How to subsidize agriculture? *Journal of Cleaner Production*, 164, 258–264. <https://doi.org/10.1016/j.jclepro.2017.06.216>
- Chisti, Y., & Moo-Young, M. (1993). Improve the performance of airlift reactors. In *Chemical Engineering Progress* (Vol. 89, Issue 6, pp. 38–45).
- Chiu, Y. H., Chang, T. F. M., Chen, C. Y., Sone, M., & Hsu, Y. J. (2019). Mechanistic insights into photodegradation of organic dyes using heterostructure photocatalysts. *Catalysts*, 9(5). <https://doi.org/10.3390/catal9050430>
- Chong, M. N., Jin, B., Chow, C. W. K., & Saint, C. (2010). Recent developments in photocatalytic water treatment technology: A review. *Water Research*, 44(10), 2997–3027. <https://doi.org/10.1016/j.watres.2010.02.039>
- Daou, I., Zegaoui, O., & Elghazouani, A. (2017). Physicochemical and photocatalytic properties of the ZnO particles were synthesized by two different methods using three different precursors. *Comptes Rendus Chimie*, 20(1), 47–54. <https://doi.org/10.1016/j.crci.2016.04.003>
- Dong, H., Zeng, G., Tang, L., Fan, C., Zhang, C., He, X., & He, Y. (2015). An overview of limitations of TiO₂-based particles for photocatalytic degradation of organic pollutants and the corresponding countermeasures. *Water Research*, 79, 128–146. <https://doi.org/10.1016/j.watres.2015.04.038>

- Drumond Chequer, F. M., de Oliveira, G. A. R., Anastacio Ferraz, E. R., Carvalho, J., Boldrin Zanoni, M. V., & de Oliveir, D. P. (2013). Textile Dyes: Dyeing Process and Environmental Impact. *Eco-Friendly Textile Dyeing and Finishing*. <https://doi.org/10.5772/53659>
- El Mragui, A., Daou, I., & Zegaoui, O. (2019). Influence of the preparation method and ZnO/(ZnO + TiO₂) weight ratio on the physicochemical and photocatalytic properties of ZnO-TiO₂ nanomaterials. *Catalysis Today*, 321–322(January 2018), 41–51. <https://doi.org/10.1016/j.cattod.2018.01.016>
- El, R., Eimer, G. A., Rodríguez, P. A. O., Benzaquén, T. B., Pecchi, G. A., Casuscelli, S. G., Elías, V. R., & Eimer, G. A. (2019). Novel Route to Obtain Carbon Self-Doped TiO₂ Mesoporous Nanoparticles as Efficient Photocatalysts Visible Light. *Materials*, 12(20). <https://pubmed.ncbi.nlm.nih.gov/31615094/>
- Elisadiki, J., Jande, Y. A. C., Machunda, R. L., & Kibona, T. E. (2019). Porous carbon derived from Artocarpus heterophyllus peels for capacitive deionization electrodes. *Carbon*, 147, 582–593. <https://doi.org/10.1016/j.carbon.2019.03.036>
- Farré, M. la, Pérez, S., Kantiani, L., & Barceló, D. (2008). Fate and toxicity of emerging pollutants, their metabolites and transformation products in the aquatic environment. *TrAC-Trends in Analytical Chemistry*, 27(11), 991–1007. <https://doi.org/10.1016/j.trac.2008.09.010>
- Foo, K. Y., & Hameed, B. H. (2010). An overview of dye removal via the activated carbon adsorption process. *Desalination and Water Treatment*, 19(1–3), 255–274. <https://doi.org/10.5004/dwt.2010.1214>
- Fu, P., Feng, J., Yang, T., & Yang, H. (2015). Comparison of alkyl xanthates degradation in aqueous solution by the O₃ and UV/O₃ processes: Efficiency, mineralization and ozone utilization. *Minerals Engineering*, 81, 128–134. <https://doi.org/10.1016/j.mineng.2015.08.001>
- Fujishima, A., Rao, T. N., & Tryk, D. A. (2000). Titanium dioxide photocatalysis. *Journal of Photochemistry and Photobiology C: Photochemistry Reviews*, 1(1), 1–21. [https://doi.org/10.1016/S1389-5567\(00\)00002-2](https://doi.org/10.1016/S1389-5567(00)00002-2)
- Fujishima, A., Zhang, X., & Tryk, D. A. (2008). TiO₂ photocatalysis and related surface phenomena. *Surface Science Reports*, 63(12), 515–582. <https://doi.org/10.1016/j.surfrep.2008.10.001>
- Gao, B., Seng, P., Mariana, T., & Lim, T. (2011). Adsorption-photocatalytic degradation of Acid Red 88 by supported TiO₂: Effect of activated carbon support and aqueous anions. *Chemical Engineering Journal*, 171(3), 1098–1107. <https://doi.org/10.1016/j.cej.2011.05.006>
- Gao, D. W., & Wen, Z. D. (2016). Phthalate esters in the environment: A critical review of their occurrence, biodegradation, and removal during wastewater treatment processes. *Science of the Total Environment*, 541, 986–1001. <https://doi.org/10.1016/j.scitotenv.2015.09.148>
- Gao, H. T., Si, C. D., Zhou, J., & Liu, G. J. (2011). Sound assisted photocatalytic degradation of formaldehyde in fluidized bed reactor. *Journal of the Taiwan*

- Institute of Chemical Engineers*, 42(1), 108–113.
<https://doi.org/10.1016/j.jtice.2010.05.005>
- Gaya, U. I., & Abdullah, A. H. (2008). Heterogeneous photocatalytic degradation of organic contaminants over titanium dioxide: A review of fundamentals, progress and problems. *Journal of Photochemistry and Photobiology C: Photochemistry Reviews*, 9(1), 1–12. <https://doi.org/10.1016/j.jphotochemrev.2007.12.003>
- Gupta, D., Chauhan, R., Kumar, N., Singh, V., Srivastava, V. C., Mohanty, P., & Mandal, T. K. (2020). Enhancing photocatalytic degradation of quinoline by ZnO: TiO₂ mixed oxide: Optimization of operating parameters and mechanistic study. *Journal of Environmental Management*, 258(May 2019), 110032. <https://doi.org/10.1016/j.jenvman.2019.110032>
- Haribabu, K., & Sivasubramanian, V. (2014). Treatment of wastewater in fluidized bed bioreactor using low-density biosupport. *Energy Procedia*, 50, 214–221. <https://doi.org/10.1016/j.egypro.2014.06.026>
- Haroun, M., & Idris, A. (2009). Treatment of textile wastewater with an anaerobic fluidized bed reactor. *Desalination*, 237(1–3), 357–366. <https://doi.org/10.1016/j.desal.2008.01.027>
- Hassanpour, M., Safardoust-Hojaghan, H., & Salavati-Niasari, M. (2017). Degradation of methylene blue and Rhodamine B as water pollutants via green synthesized Co₃O₄/ZnO nanocomposite. *Journal of Molecular Liquids*, 229, 293–299. <https://doi.org/10.1016/j.molliq.2016.12.090>
- Helm, J. S., Nishioka, M., Brody, J. G., Rudel, R. A., & Dodson, R. E. (2019). Re: Measurement of endocrine disrupting and asthma-associated chemicals in hair products used by Black women. *Environmental Research*, 172(November 2018), 719–721. <https://doi.org/10.1016/j.envres.2018.11.029>
- Herrmann, J. M., Duchamp, C., Karkmaz, M., Hoai, B. T., Lachheb, H., Puzenat, E., & Guillard, C. (2007). Environmental green chemistry as defined by photocatalysis. *Journal of Hazardous Materials*, 146(3), 624–629. <https://doi.org/10.1016/j.jhazmat.2007.04.095>
- Herrmann, Jean Marie. (1999). Heterogeneous photocatalysis: fundamentals and applications to the removal of various types of aqueous pollutants. *Catalysis Today*, 53(1), 115–129. [https://doi.org/10.1016/S0920-5861\(99\)00107-8](https://doi.org/10.1016/S0920-5861(99)00107-8)
- Horn, O., Nalli, S., Cooper, D., & Nicell, J. (2004). Plasticizer metabolites in the environment. *Water Research*, 38(17), 3693–3698. <https://doi.org/10.1016/j.watres.2004.06.012>
- Houas, A., Lachheb, H., Ksibi, M., Elaloui, E., Guillard, C., & Herrmann, J. M. (2001). Photocatalytic degradation pathway of methylene blue in the water. *Applied Catalysis B: Environmental*, 31(2), 145–157. [https://doi.org/10.1016/S0926-3373\(00\)00276-9](https://doi.org/10.1016/S0926-3373(00)00276-9)
- Huang, Y. hua, Dsikowitzky, L., Yang, F., & Schwarzbauer, J. (2020). Emerging contaminants in municipal wastewaters and their relevance for the surface water contamination in the tropical coastal city Haikou, China. *Estuarine, Coastal and*

- Shelf Science*, 235(December 2019), 106611.
<https://doi.org/10.1016/j.ecss.2020.106611>
- Hussain, S., Quinn, L., Li, J., Casey, E., & Murphy, C. D. (2017). Simultaneous removal of malachite green and hexavalent chromium by *Cunninghamella elegans* biofilm in a semi-continuous system. *International Biodeterioration and Biodegradation*, 125, 142–149. <https://doi.org/10.1016/j.ibiod.2017.09.003>
- Jarrah, N. (2017). Competitive adsorption isotherms of rhodium 6G and methylene blue on activated carbon prepared from residual fuel oil. *Journal of Environmental Chemical Engineering*, 5(5), 4319–4326. <https://doi.org/10.1016/j.jece.2017.08.006>
- Jelic, A., Gros, M., Ginebreda, A., Cespedes-Sánchez, R., Ventura, F., Petrovic, M., & Barcelo, D. (2011). Occurrence, partition and removal of pharmaceuticals in sewage water and sludge during wastewater treatment. *Water Research*, 45(3), 1165–1176. <https://doi.org/10.1016/j.watres.2010.11.010>
- Jonidi-Jafari, A., Shirzad-Siboni, M., Yang, J. K., Naimi-Joubani, M., & Farrokhi, M. (2015). Photocatalytic degradation of diazinon with illuminated ZnO-TiO₂ composite. *Journal of the Taiwan Institute of Chemical Engineers*, 50, 100–107. <https://doi.org/10.1016/j.jtice.2014.12.020>
- K'oreje, K. O., Vergeynst, L., Ombaka, D., De Wispelaere, P., Okoth, M., Van Langenhove, H., & Demeestere, K. (2016). Occurrence patterns of pharmaceutical residues in wastewater, surface water and groundwater of Nairobi and Kisumu city, Kenya. *Chemosphere*, 149, 238–244. <https://doi.org/10.1016/j.chemosphere.2016.01.095>
- K'oreje, Kenneth Otieno, Demeestere, K., De Wispelaere, P., Vergeynst, L., Dewulf, J., & Van Langenhove, H. (2012). From multi-residue screening to target analysis of pharmaceuticals in water: Development of a new approach based on magnetic sector mass spectrometry and application in the Nairobi River basin, Kenya. *Science of the Total Environment*, 437, 153–164. <https://doi.org/10.1016/j.scitotenv.2012.07.052>
- Kohtani, S., Kawashima, A., & Miyabe, H. (2017). Reactivity of Trapped and Accumulated Electrons in Titanium Dioxide Photocatalysis. *Catalysts*, 7(10), 303. <https://doi.org/10.3390/catal7100303>
- Lawson-wood, K. (2016). *Water Analysis Using LAMBDA UV-Visible Spectrophotometers : nitrate-nitrogen Determination*. 9–11.
- Lellis, B., Fávaro-Polonio, C. Z., Pamphile, J. A., & Polonio, J. C. (2019). Effects of textile dyes on health and the environment and bioremediation potential of living organisms. *Biotechnology Research and Innovation*, 3(2), 275–290. <https://doi.org/10.1016/j.biori.2019.09.001>
- Li, Z. D., Wang, H. L., Wei, X. N., Liu, X. Y., Yang, Y. F., & Jiang, W. F. (2016). Preparation and photocatalytic performance of magnetic Fe₃O₄@TiO₂ core-shell microspheres supported by silica aerogels from industrial fly ash. *Journal of Alloys and Compounds*, 659, 240–247. <https://doi.org/10.1016/j.jallcom.2015.10.297>

- Liao, D. L., Badour, C. A., & Liao, B. Q. (2008). Preparation of nanosized TiO₂/ZnO composite catalyst and its photocatalytic activity for degradation of methyl orange. *Journal of Photochemistry and Photobiology A: Chemistry*, 194(1), 11–19. <https://doi.org/10.1016/j.jphotochem.2007.07.008>
- Liu, X., Chen, Z., Zhou, N., Shen, J., & Ye, M. (2010). Degradation and detoxification of microcystin-LR in drinking water by sequential use of UV and ozone. *Journal of Environmental Sciences*, 22(12), 1897–1902. [https://doi.org/10.1016/S1001-0742\(09\)60336-3](https://doi.org/10.1016/S1001-0742(09)60336-3)
- Luo, S., Gao, L., Wei, Z., Spinney, R., Dionysiou, D. D., Hu, W. P., Chai, L., & Xiao, R. (2018). Kinetic and mechanistic aspects of hydroxyl radical-mediated degradation of naproxen and reaction intermediates. *Water Research*, 137, 233–241. <https://doi.org/10.1016/j.watres.2018.03.002>
- Luo, Y., Guo, W., Ngo, H. H., Nghiem, L. D., Hai, F. I., Zhang, J., Liang, S., & Wang, X. C. (2014). A review on the occurrence of micropollutants in the aquatic environment and their fate and removal during wastewater treatment. *Science of the Total Environment*, 473–474, 619–641. <https://doi.org/10.1016/j.scitotenv.2013.12.065>
- Lutic, D., Coromelci-Pastravanu, C., Cretescu, I., Poullos, I., & Stan, C. D. (2012). Photocatalytic treatment of rhodamine 6G in wastewater using photoactive ZnO. *International Journal of Photoenergy*, 2012. <https://doi.org/10.1155/2012/475131>
- Madikizela, L. M., Tavengwa, N. T., & Chimuka, L. (2017). Status of pharmaceuticals in African water bodies: Occurrence, removal and analytical methods. *Journal of Environmental Management*, 193, 211–220. <https://doi.org/10.1016/j.jenvman.2017.02.022>
- Mahamuni, N. N., & Adewuyi, Y. G. (2010). Advanced oxidation processes (AOPs) involving ultrasound for wastewater treatment: A review with emphasis on cost estimation. *Ultrasonics Sonochemistry*, 17(6), 990–1003. <https://doi.org/10.1016/j.ultsonch.2009.09.005>
- Mallakpour, S., & Nikkhoo, E. (2014). Surface modification of nano-TiO₂ with trimellitylimido-amino acid-based diacids for preventing aggregation of nanoparticles. *Advanced Powder Technology*, 25(1), 348–353. <https://doi.org/10.1016/j.appt.2013.05.017>
- Manickum, T., & John, W. (2014). Occurrence, fate and environmental risk assessment of endocrine disrupting compounds at the wastewater treatment works in Pietermaritzburg (South Africa). *Science of the Total Environment*, 468–469, 584–597. <https://doi.org/10.1016/j.scitotenv.2013.08.041>
- Maria Magdalane, C., Kaviyarasu, K., Judith Vijaya, J., Jayakumar, C., Maaza, M., & Jeyaraj, B. (2017). Photocatalytic degradation effect of malachite green and catalytic hydrogenation by UV-illuminated CeO₂/CdO multilayered nanoplatelet arrays: Investigation of antifungal and antimicrobial activities. *Journal of Photochemistry and Photobiology B: Biology*, 169(March), 110–123. <https://doi.org/10.1016/j.jphotobiol.2017.03.008>
- Martín-Sómer, M., Pablos, C., van Grieken, R., & Marugán, J. (2017). Influence of

- light distribution on the performance of photocatalytic reactors: LED vs mercury lamps. *Applied Catalysis B: Environmental*, 215, 1–7. <https://doi.org/10.1016/j.apcatb.2017.05.048>
- Matsumura, T., Noshiroya, D., Tokumura, M., Znad, H. T., & Kawase, Y. (2007). Simplified model for the hydrodynamics and reaction kinetics in a gas-liquid-solid three-phase fluidized-bed photocatalytic reactor: Degradation of o-cresol with immobilized TiO₂. *Industrial and Engineering Chemistry Research*, 46(8), 2637–2647. <https://doi.org/10.1021/ie061509r>
- Miklos, D. B., Remy, C., Jekel, M., Linden, K. G., Drewes, J. E., & Hübner, U. (2018). Evaluation of advanced oxidation processes for water and wastewater treatment – A critical review. *Water Research*, 139, 118–131. <https://doi.org/10.1016/j.watres.2018.03.042>
- Mofokeng, S. J., Kumar, V., Kroon, R. E., & Ntwaeaborwa, O. M. (2017). Structure and optical properties of Dy³⁺ activated sol-gel ZnO-TiO₂ nanocomposites. *Journal of Alloys and Compounds*, 711, 121–131. <https://doi.org/10.1016/j.jallcom.2017.03.345>
- Mosleh, S., Rahimi, M. R., Ghaedi, M., Dashtian, K., Hajati, S., & Wang, S. (2017). Ag₃PO₄/AgBr/Ag-HKUST-1-MOF composites as novel blue LED light active photocatalyst for enhanced degradation of a ternary mixture of dyes in a rotating packed bed reactor. *Chemical Engineering and Processing - Process Intensification*, 114, 24–38. <https://doi.org/10.1016/j.cep.2017.01.009>
- Natarajan, K., Bajaj, H. C., & Tayade, R. J. (2016). Photocatalytic efficiency of bismuth oxyhalide (Br, Cl and I) nanoplates for RhB dye degradation under LED irradiation. *Journal of Industrial and Engineering Chemistry*, 34, 146–156. <https://doi.org/10.1016/j.jiec.2015.11.003>
- Navntoft, C., Ubomba-Jaswa, E., McGuigan, K. G., & Fernández-Ibáñez, P. (2008). Effectiveness of solar disinfection using batch reactors with non-imaging aluminium reflectors under real conditions: Natural well-water and solar light. *Journal of Photochemistry and Photobiology B: Biology*, 93(3), 155–161. <https://doi.org/10.1016/j.jphotobiol.2008.08.002>
- Nawrocki, J., & Kasprzyk-Hordern, B. (2010). The efficiency and mechanisms of catalytic ozonation. *Applied Catalysis B: Environmental*, 99(1–2), 27–42. <https://doi.org/10.1016/j.apcatb.2010.06.033>
- Nguyen, C. H., Tran, M. L., Tran, T. T. Van, & Juang, R. S. (2020). Enhanced removal of various dyes from aqueous solutions by UV and simulated solar photocatalysis over TiO₂/ZnO/rGO composites. *Separation and Purification Technology*, 232(July 2019). <https://doi.org/10.1016/j.seppur.2019.115962>
- Nieto-Sandoval, J., Munoz, M., de Pedro, Z. M., & Casas, J. A. (2018). Fast degradation of diclofenac by catalytic hydrochlorination. *Chemosphere*, 213, 141–148. <https://doi.org/10.1016/j.chemosphere.2018.09.024>
- Nikolov, V., Farag, I., & Nikov, I. (2000). Gas-liquid mass transfer in a bioreactor with the three-phase inverse fluidized bed. *Bioprocess Engineering*, 23(5), 427–429. <https://doi.org/10.1007/s004499900124>

- Nowak, K., Ratajczak-Wrona, W., Górska, M., & Jabłońska, E. (2018). Parabens and their effects on the endocrine system. *Molecular and Cellular Endocrinology*, 474(December 2017), 238–251. <https://doi.org/10.1016/j.mce.2018.03.014>
- Ntuli, F., & Lewis, A. E. (2010). The precipitation kinetics of nickel powder produced by hydrogen reduction in commercial batch autoclaves. *AIP Conference Proceedings*, 1247(November 2014), 301–312. <https://doi.org/10.1063/1.3460239>
- Ochieng, A., Odiyo, J. O., & Mutsago, M. (2003). Biological treatment of mixed industrial wastewaters in a fluidised bed reactor. *Journal of Hazardous Materials*, 96(1), 79–90. [https://doi.org/10.1016/S0304-3894\(02\)00166-8](https://doi.org/10.1016/S0304-3894(02)00166-8)
- Ochieng, A., Ogada, T., Sisenda, W., & Wambua, P. (2002). Brewery wastewater treatment in a fluidised bed bioreactor. *Journal of Hazardous Materials*, 90(3), 311–321. [https://doi.org/10.1016/S0304-3894\(01\)00373-9](https://doi.org/10.1016/S0304-3894(01)00373-9)
- Orge, C. A., Pereira, M. F. R., & Faria, J. L. (2017). Photocatalytic-assisted ozone degradation of metolachlor aqueous solution. *Chemical Engineering Journal*, 318, 247–253. <https://doi.org/10.1016/j.cej.2016.06.136>
- Otieno, B. O., Apollo, S. O., Naidoo, B. E., Ochieng, A., Otieno, B. O., Apollo, S. O., Naidoo, B. E., & Ochieng, A. (2017). Toxic/Hazardous Substances and Environmental Engineering Photodecolorisation of melanoidins in vinasse with illuminated TiO₂-ZnO / activated carbon composite. *Journal of Environmental Science and Health, Part A*, 52(7), 616–623. <https://doi.org/10.1080/10934529.2017.1294963>
- Paíga, P., Santos, L. H. M. L. M., Ramos, S., Jorge, S., Silva, J. G., & Delerue-Matos, C. (2016). Presence of pharmaceuticals in the Lis river (Portugal): Sources, fate and seasonal variation. *Science of the Total Environment*, 573, 164–177. <https://doi.org/10.1016/j.scitotenv.2016.08.089>
- Parfitt, J., Barthel, M., & MacNaughton, S. (2010). Food waste within food supply chains: Quantification and potential for change to 2050. *Philosophical Transactions of the Royal Society B: Biological Sciences*, 365(1554), 3065–3081. <https://doi.org/10.1098/rstb.2010.0126>
- Parrino, F., Camera-Roda, G., Loddo, V., Augugliaro, V., & Palmisano, L. (2015). Photocatalytic ozonation: Maximization of the reaction rate and control of undesired by-products. *Applied Catalysis B: Environmental*, 178, 37–43. <https://doi.org/10.1016/j.apcatb.2014.10.081>
- Pashai Gatabi, M., Milani Moghaddam, H., & Ghorbani, M. (2016). Point of zero charges of maghemite decorated multiwalled carbon nanotubes fabricated by chemical precipitation method. *Journal of Molecular Liquids*, 216, 117–125. <https://doi.org/10.1016/j.molliq.2015.12.087>
- Peng, S., Ke, Z., Cao, X., Shan, C., Zhao, F., Guan, M., Shi, L., Sun, Y., Yang, Y., & Ma, L. (2020). A novel type of borosilicate glass with excellent chemical stability and high ultraviolet transmission. *Journal of Non-Crystalline Solids*, 528(October 2019), 1–6. <https://doi.org/10.1016/j.jnoncrsol.2019.119735>
- Planelló, R., Herrero, O., Martínez-Guitarte, J. L., & Morcillo, G. (2011). Comparative

- effects of butyl benzyl phthalate (BBP) and di(2-ethylhexyl) phthalate (DEHP) on the aquatic larvae of *Chironomus riparius* based on gene expression assays related to the endocrine system, the stress response and ribosomes. *Aquatic Toxicology*, 105(1–2), 62–70. <https://doi.org/10.1016/j.aquatox.2011.05.011>
- Rasheed, T., Bilal, M., Iqbal, H. M. N., Hu, H., & Zhang, X. (2017). Reaction Mechanism and Degradation Pathway of Rhodamine 6G by Photocatalytic Treatment. *Water, Air, and Soil Pollution*, 228(8). <https://doi.org/10.1007/s11270-017-3458-6>
- Ray, A. K. (1998). *Development of a New Photocatalytic Reactor for Water Purification*, *Catalysis Today* 40 (1) (1998) pp.73. 40, 73–83.
- Reingruber, H., & Pontel, L. B. (2018). Formaldehyde metabolism and its impact on human health. *Current Opinion in Toxicology*, 9, 28–34. <https://doi.org/10.1016/j.cotox.2018.07.001>
- Renz, L., Volz, C., Michanowicz, D., Ferrar, K., Christian, C., Lenzner, D., & El-Hefnawy, T. (2013). A study of parabens and bisphenol A in surface water and fish brain tissue from the Greater Pittsburgh Area. *Ecotoxicology*, 22(4), 632–641. <https://doi.org/10.1007/s10646-013-1054-0>
- Richardson, S. D., Plewa, M. J., Wagner, E. D., Schoeny, R., & DeMarini, D. M. (2007). Occurrence, genotoxicity, and carcinogenicity of regulated and emerging disinfection by-products in drinking water: A review and roadmap for research. *Mutation Research - Reviews in Mutation Research*, 636(1–3), 178–242. <https://doi.org/10.1016/j.mrrev.2007.09.001>
- Rodríguez, S. M., Gálvez, J. B., Rubio, M. I. M., Ibáñez, P. F., Padilla, D. A., Pereira, M. C., Mendes, J. F., & De Oliveira, J. C. (2004). Engineering of solar photocatalytic collectors. *Solar Energy*, 77(5), 513–524. <https://doi.org/10.1016/j.solener.2004.03.020>
- Santhana Raj, D., Nagarajan, S. V., Raman, T., Venkatachalam, P., & Parthasarathy, M. (2021). Remediation of textile effluents for water reuse: Decolorization and desalination using *Escherichia fergusonii* followed by detoxification with activated charcoal. *Journal of Environmental Management*, 277(October 2020), 111406. <https://doi.org/10.1016/j.jenvman.2020.111406>
- Segura, P. A., Takada, H., Correa, J. A., El Saadi, K., Koike, T., Onwona-Agyeman, S., Ofosu-Anim, J., Sabi, E. B., Wasonga, O. V., Mghalu, J. M., dos Santos, A. M., Newman, B., Weerts, S., & Yargeau, V. (2015). Global occurrence of anti-infectives in contaminated surface waters: Impact of income inequality between countries. *Environment International*, 80, 89–97. <https://doi.org/10.1016/j.envint.2015.04.001>
- Shengyan, P., Rongxin, Z., Hui, M., Daili, D., Xiangjun, P., Fei, Q., & Wei, C. (2017). Applied Catalysis B: Environmental Facile in-situ design strategy to disperse TiO₂ nanoparticles on graphene for the enhanced photocatalytic degradation of rhodamine. *“Applied Catalysis B, Environmental,”* 218, 208–219. <https://doi.org/10.1016/j.apcatb.2017.06.039>
- Singh, J., Kumar, S., Rishikesh, Manna, A. K., & Soni, R. K. (2020). Fabrication of

- ZnO–TiO₂ nanohybrids for rapid sunlight driven photodegradation of textile dyes and antibiotic residue molecules. *Optical Materials*, 107(May), 110138. <https://doi.org/10.1016/j.optmat.2020.110138>
- Sivakumar Natarajan, T., Bajaj, H. C., & Tayade, R. J. (2016). Palmyra tuber peel derived activated carbon and anatase TiO₂ nanotube-based nanocomposites with enhanced photocatalytic performance in rhodamine 6G dye degradation. *Process Safety and Environmental Protection*, 104, 346–357. <https://doi.org/10.1016/j.psep.2016.09.021>
- Siwińska-Stefańska, K., Kubiak, A., Piasecki, A., Goscińska, J., Nowaczyk, G., Jurga, S., & Jesionowski, T. (2018). TiO₂-ZnO binary oxide systems: Comprehensive characterization and tests of photocatalytic activity. *Materials*, 11(5), 1–19. <https://doi.org/10.3390/ma11050841>
- Sur, D. H., & Mukhopadhyay, M. (2017). COD reduction of textile effluent in three-phase fluidized bed bioreactor using *Pseudomonas aureofaciens* and *Escherichia coli*. *3 Biotech*, 7(2), 1–11. <https://doi.org/10.1007/s13205-017-0771-0>
- Taggart, M. A., Senacha, K. R., Green, R. E., Jhala, Y. V., Raghavan, B., Rahmani, A. R., Cuthbert, R., Pain, D. J., & Meharg, A. A. (2007). Diclofenac residues in carcasses of domestic ungulates are available to vultures in India. *Environment International*, 33(6), 759–765. <https://doi.org/10.1016/j.envint.2007.02.010>
- Tobajas, M., Belver, C., & Rodriguez, J. J. (2017). Degradation of emerging pollutants in water under solar irradiation using novel TiO₂-ZnO/clay nanoarchitectures. *Chemical Engineering Journal*, 309, 596–606. <https://doi.org/10.1016/j.cej.2016.10.002>
- Tong, A. Y. C., Peake, B. M., & Braund, R. (2011). Disposal practices for unused medications around the world. *Environment International*, 37(1), 292–298. <https://doi.org/10.1016/j.envint.2010.10.002>
- Tran, T. M., Hoang, A. Q., Le, S. T., Minh, T. B., & Kannan, K. (2019). A review of contamination status, emission sources, and human exposure to volatile methyl siloxanes (VMSs) in indoor environments. *Science of the Total Environment*, 691, 584–594. <https://doi.org/10.1016/j.scitotenv.2019.07.168>
- Ugwu, U. S., & Ogbonna, J. C. (2002). Improvement of mass transfer characteristics and productivities of inclined tubular photobioreactors by the installation of internal static mixers. *October 2014*. <https://doi.org/10.1007/s00253-002-0940-9>
- Wang, H. L., Qi, H. P., Wei, X. N., Liu, X. Y., & Jiang, W. F. (2016). Photocatalytic activity of TiO₂ supported SiO₂-Al₂O₃ aerogels prepared from industrial fly ash. *Cuihua Xuebao/Chinese Journal of Catalysis*, 37(11), 2025–2033. [https://doi.org/10.1016/S1872-2067\(16\)62546-9](https://doi.org/10.1016/S1872-2067(16)62546-9)
- Wang, Jianlong, & Zhuan, R. (2020). Degradation of antibiotics by advanced oxidation processes: An overview. *Science of the Total Environment*, 701, 135023. <https://doi.org/10.1016/j.scitotenv.2019.135023>
- Wang, Juan, Wang, G., Wei, X., Liu, G., & Li, J. (2018). ZnO nanoparticles implanted in TiO₂ macro channels as an effective direct Z-scheme heterojunction

- photocatalyst for degradation of RhB. *Applied Surface Science*, 456(June), 666–675. <https://doi.org/10.1016/j.apsusc.2018.06.182>
- Wang, X., Wu, Z., Wang, Y., Wang, W., Wang, X., Bu, Y., & Zhao, J. (2013). Adsorption – photodegradation of humic acid in water by using ZnO coupled TiO₂/bamboo charcoal under visible light irradiation. *Journal of Hazardous Materials*, 262, 16–24. <https://doi.org/10.1016/j.jhazmat.2013.08.037>
- Xue, M., Lu, W., Chen, C., Tan, Y., Li, B., & Zhang, C. (2019). Optimized synthesis of banana peel derived porous carbon and its application in lithium-sulfur batteries. *Materials Research Bulletin*, 112(December 2018), 269–280. <https://doi.org/10.1016/j.materresbull.2018.12.035>
- Yan, H., Lu, P., Pan, Z., Wang, X., Zhang, Q., & Li, L. (2013). Ce/SBA-15 as a heterogeneous ozonation catalyst for efficient mineralization of dimethyl phthalate. *Journal of Molecular Catalysis A: Chemical*, 377, 57–64. <https://doi.org/10.1016/j.molcata.2013.04.032>
- Yar, A., Haspulat, B., Üstün, T., Eskizeybek, V., Avci, A., Kamiş, H., & Achour, S. (2017). Electrospun TiO₂/ZnO/PAN hybrid nanofiber membranes with efficient photocatalytic activity. *RSC Advances*, 7(47), 29806–29814. <https://doi.org/10.1039/c7ra03699j>
- Yousuf, M., Baloch, J., Sajid, & Mangi, H. (2019). Treatment of Synthetic Greywater by Using Banana, Orange and Sapodilla Peel as a Low Cost Activated Carbon. *J. Mater. Environ. Sci*, 10(10), 966. www.jmaterenvirosci.com
- Zhang, T., Yang, Y., Ni, J., & Xie, D. (2019). Adoption behaviour of cleaner production techniques to control agricultural non-point source pollution: A case study in the Three Gorges Reservoir Area. *Journal of Cleaner Production*, 223, 897–906. <https://doi.org/10.1016/j.jclepro.2019.03.194>
- Zheng, X., Shen, Z. P., Shi, L., Cheng, R., & Yuan, D. H. (2017). Photocatalytic membrane reactors (PMRs) in water treatment: Configurations and influencing factors. *Catalysts*, 7(8). <https://doi.org/10.3390/catal7080224>
- Zyoud, A. H., Asaad, S., Zyoud, S. H., Zyoud, S. H., Helal, M. H., Qamhieh, N., Hajamohideen, A. R., & Hilal, H. S. (2020). Raw clay supported ZnO nanoparticles in photodegradation of 2-chlorophenol under direct solar radiations. *Journal of Environmental Chemical Engineering*, 8(5), 104227. <https://doi.org/10.1016/j.jece.2020.104227>
- Zyoud, A. H., Zubi, A., Hejjawi, S., Zyoud, S. H., Helal, M. H., Zyoud, S. H., Qamhieh, N., Hajamohideen, A., & Hilal, H. S. (2020). Removal of acetaminophen from water by simulated solar light photodegradation with ZnO and TiO₂ nanoparticles: Catalytic efficiency assessment for future prospects. *Journal of Environmental Chemical Engineering*, 8(4), 104038. <https://doi.org/10.1016/j.jece.2020.104038>

APPENDIX

Appendix A: Industrial applications and ecotoxicological of Malachite green (MG), methylene blue (MB) and Rhodamine6G (R6G) azo dyes.

Industrial applications

Used in the dyeing of fabrics, leather, and plastic products (MG, MB and R6G).

Used in the commercial fish hatchery to treat fungal infections (MG and MB).

Used as staining in conducting surgery especially for treatment methemoglobinemia and urinary tract infections (MB).

Food colouring agent and food additive (MG, and MB).

Antiseptic, and anthelmintic drugs for humans (MG, and MB).

Used in biotechnology such as fluorescence microscopy and flow cytometry (R6G).

Ecotoxicological effects (MG, MB and R6G).

Persistent in different environmental conditions due to its complex molecular structure.

Reduces photosynthesis activity by limiting sunlight penetration in water, and subsequently dissolved oxygen deficiency which adversely affects the aquatic life.

Damage human organs such as the central nervous system, lungs, spleen, kidney, and liver when ingested.

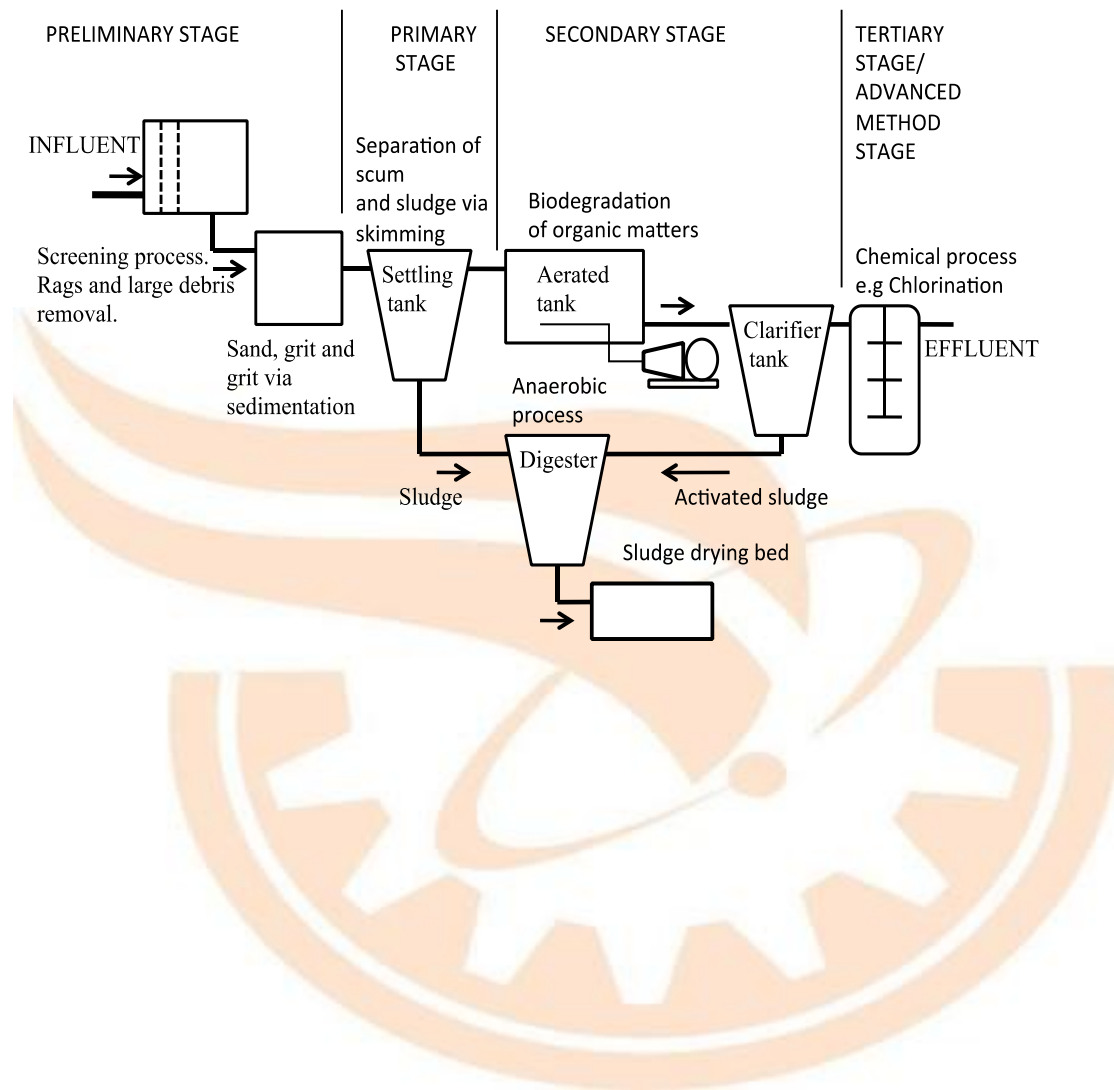
Inflict carcinogenic, mutagenic effects and result in tetra genic effects.

Trigger eye burns, dermatitis, allergic conjunctivitis, asthma, and other allergic reactions.

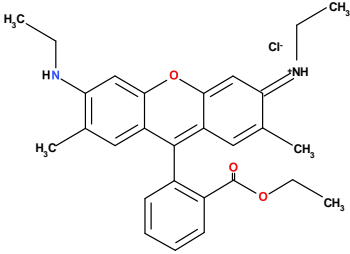
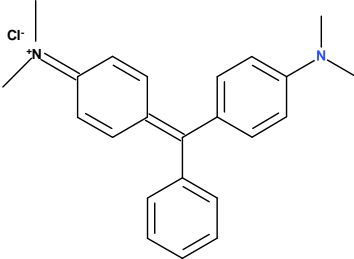
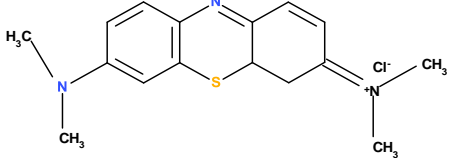
Cytotoxic effects on mammalian cells

Alteration of human body blood counts causes blood dyscrasias, anaemia, leukaemia, and delay in blood coagulation.

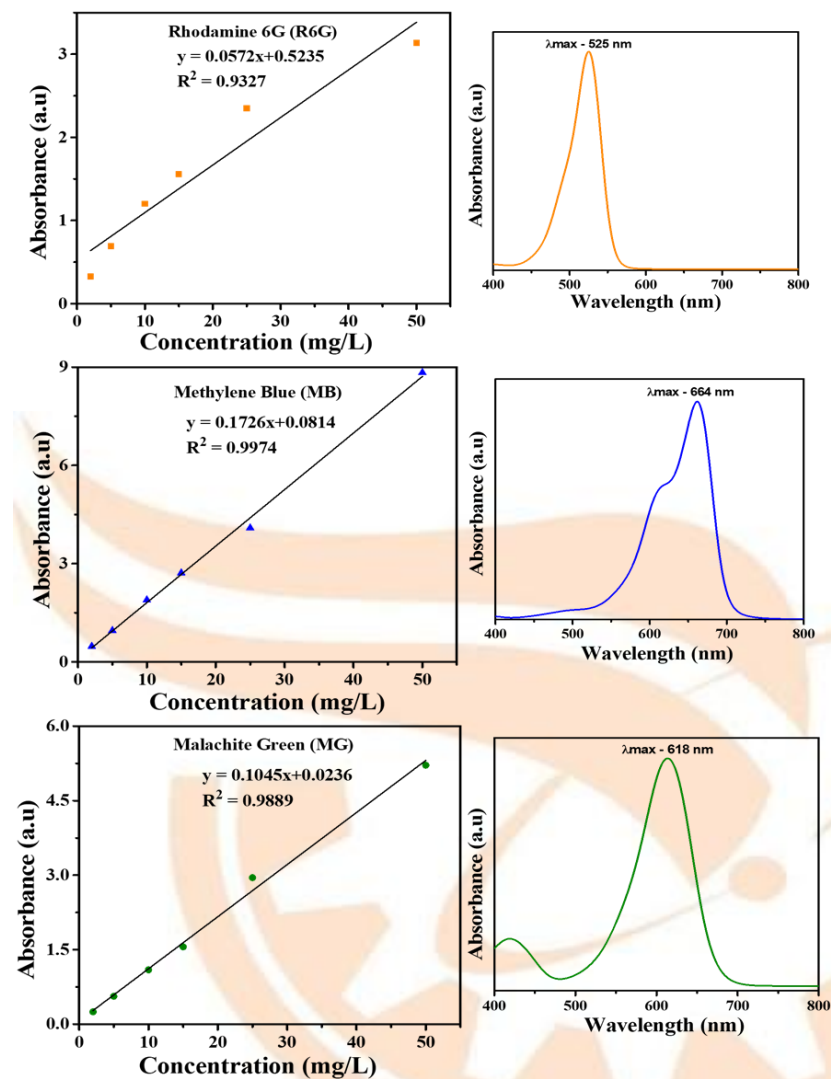
Appendix B: Typical conventional wastewater treatment plant.



Appendix C: Physicochemical properties of rhodamine 6G (R6G), malachite green (MG) and methylene blue (MB) dye (Chiu et al., 2019).

Dye name	Rhodamine 6G	Malachite Green Chloride	Methylene Blue
Molecular structure			
Molecular formula	C ₂₈ H ₃₁ ClN ₂ O ₃	C ₂₅ H ₂₅ ClN ₂	C ₁₆ H ₁₈ N ₃ SCl
Molecular weight (g/mol)	479.02	364.91	319.86
IUPAC name	[9-(2-ethoxycarbonylphenyl)-6-(ethylamino)-2,7-dimethylxanthen-3-ylidene]-ethylazanium; chloride	4-[[4-(dimethyl amino)phenyl]-phenyl methylidene] cyclohexa-2,5-dien-1-ylidene]-dimethylazanium; chloride	3,7-bis (Dimethyl amino)-phenothiazin-5-ium chloride
Adsorption Maximum (Y_{Max})	525 nm	618 nm	664 nm
Class	Xanthene	Triphenylmethane	Thiazine
Colour Index number	45160	42000	42780
CAS registry number	989-38-8	569-64-2	61-73-4

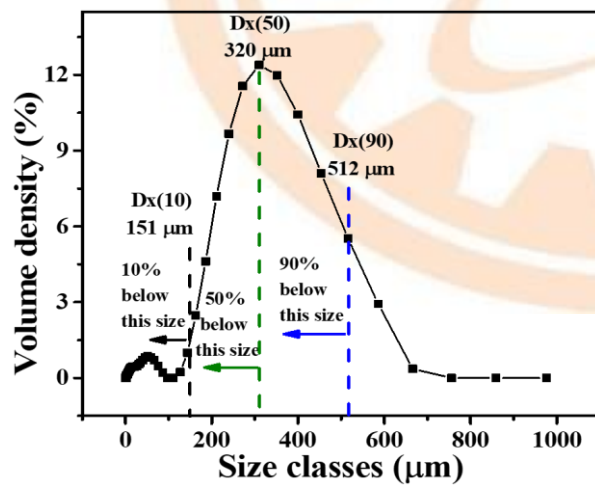
Appendix D: Physicochemical properties of rhodamine 6G (R6G), malachite green (MG) and methylene blue (MB) dye and their maximum absorbance wavelength.



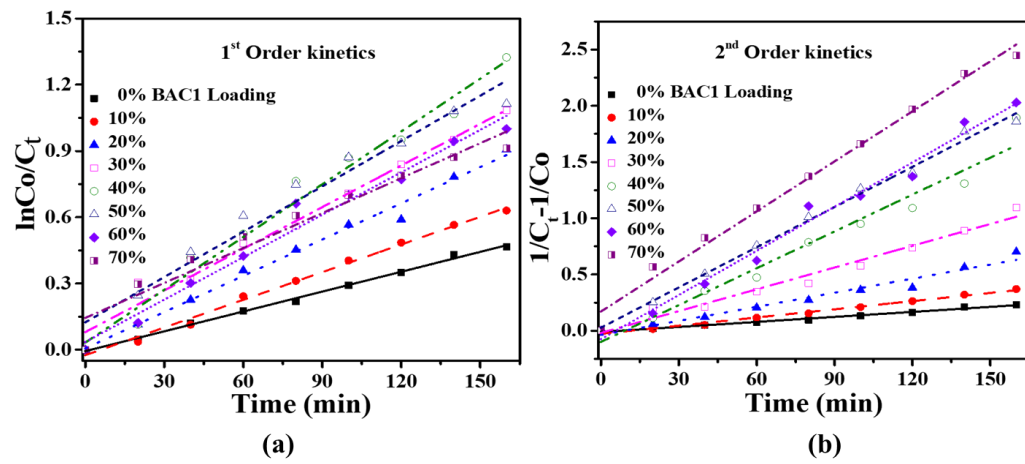
Appendix E: Particle size distribution of 85%TiO₂-ZnO/BAC1.

The particle size distribution of 85%TiO₂-ZnO/BAC1 was characterized as 10% (Dx10), 50% (Dx50), and 90% (Dx90) of the particle follow below size 151.0, 320.0, and 512.0 μm, respectively.

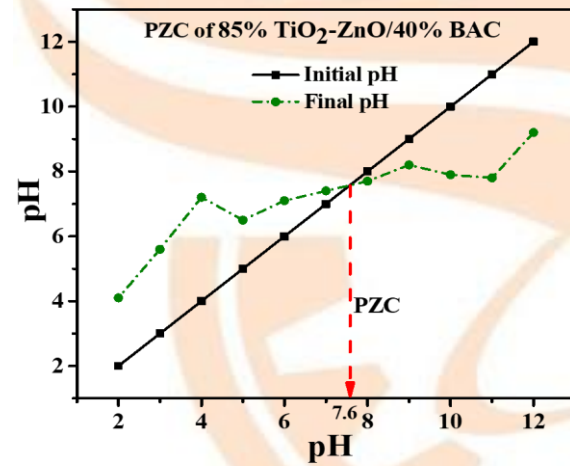
Concentration	0.15%
Span	1.128
Uniformity	0.355
Specific Surface Area	55.24 m ² /kg
D [3,2]	109 μm
D [4,3]	323 μm
Dx (10)	151 μm
Dx (50)	320 μm
Dx (90)	512 μm
Laser Obscuration	9.93%
Weighted Residual	0.78%
Particle Refractive Index	2.08
Particle Absorption Index	0.000



Appendix F: Kinetic study for the degradation of R6G using 85%TiO₂-ZnO/BACl.



Appendix G: Point of zero charge of 85%TiO₂-ZnO/BACl.



Appendix H: Thermodynamic parameters values.

Catalyst	Temperature (K)	K_L	ΔG (kJ/mol)	ΔH° (kJ/mol)	ΔS° (kJ/mol)
	303	30.6713	-8.6239		
	313	35.4244	-9.2834		
85%TiO ₂ - ZnO/BAC1	323	44.1379	-10.1705	10.3326	62.7840
	333	44.9706	-10.5372		
	353	49.2878	-11.1150		